

Mass spectrometry and laser photodissociation spectroscopy of
gas-phase metalloporphyrin complexes, metalloporphyrin
radicals, and Verteporfin

Cristiana Furlan

Master of Science by Research

University of York
Chemistry

November 2019

Abstract

Metalloporphyrins are known for interacting with donor molecules via axial coordination and this ability to attach additional ligands determines their role in biological processes such as oxygen transport or enzyme catalysis. In addition, the introduction of donor groups via ligation is being studied as a strategy for enhancing light-harvesting capacity and improving photovoltaic performance.

In this thesis, axial complexes between neutral metalloporphyrins and halide anions are studied in the gas-phase and their complexation energy determined with the aid of computational methods. The electronic properties and photochemistry of isolated gaseous zinc tetraphenyl porphyrin (ZnTPP) complexes with fluoride, chloride, bromide, and iodide are investigated using a novel custom-adapted laser-interfaced commercial mass spectrometer to provide information on how the axial complexation influences their intrinsic electronic spectra relative to the position and width of the Soret band. These spectroscopic experiments performed on negatively charged complexes are of interest because their low vertical detachment energy (VDE) can be accessed by the UV range of the laser and electron transfer processes from halide to porphyrin can be observed. In addition, these results represent the first proof of halide coordination in the gas-phase with neutral metalloporphyrin showing the formation of dimers and bridged complexes. Further experiments involved the generation of ZnTPP and nickel octaethylporphyrin (NiOEP) radical cations and anions with electrospray ionization (ESI) and LDI techniques. This work reports the first gas-phase absorption spectra of metalloporphyrin radicals together with their thermal and photo-induced dissociation channels and, a new, serendipitous, preparation procedure was found for generating metalloporphyrin radical anions in the gas phase via the LDI technique.

The last set of experiments presented in this thesis focuses on verteporfin (trade name Visudyne), a benzoporphyrin derivative photosensitizer used in photodynamic therapy of the treatment of the wet form of macular degeneration. In this work, the first direct study of its photoproducts and photofragmentation channels in an organic solvent and in the gas-phase are presented together, along with the thermal dissociation products and the first gas-phase intrinsic absorption spectrum.

Contents

Abstract	2
Contents	3
List of Tables	6
List of Figures	8
Acknowledgments.....	14
Declaration	15
CHAPTERS	
CHAPTER 1: Introduction	
1.1 Applications of porphyrins and metalloporphyrins.....	16
1.2 Structure and spectroscopic properties of porphyrins.....	17
1.3 The importance of Gas-phase studies on Metalloporphyrins.....	19
1.4 Gas-Phase studies on non-biological Metalloporphyrins	21
1.5 ESI technique and CID studies on (metallo)porphyrins	24
1.6 Metalloporphyrins and molecular beams.....	26
1.7 Porphyrin systems studied in this project	28
1.8 Aims of this project.....	30
CHAPTER 2: Experimental techniques	
2.1 Introduction to the experimental techniques.....	31
2.2 Density Functional Theory (DFT)	32
2.3 Electrospray Ionization (ESI)	33
2.4 Matrix Assisted Laser Desorbption (MALDI) and LDI.....	35
2.5 Collision Induced Dissociation (CID) and Collisional Dissociation (HCD)	36
2.6 Laser Interfaced Mass Spectrometer (LIMS).....	38
2.7 Photolysis Apparatus	41
CHAPTER 3: ZnTPP complexes with halides	
3.1 Introduction	43
3.2 Experimental methods.....	44

3.3	Effect of the metal on the complexation energies.....	45
3.4	Theoretical complexation energies of ZnP with halides and comparison with HCD	47
3.5	Optimised structures of Zn porphyrins and halide complexes	52
3.6	Photodepletion, photofragmentation and VDEs.....	56
3.7	A study on the effect of trapping parameters on the PD yield	60
3.8	ZnTPP · Br ⁻ photodepletion and photofragmentation spectra	15
3.9	ZnTPP · Cl ⁻ photodepletion and photofragmentation spectra	61
3.10	ZnTPP · F ⁻ photodepletion and photofragmentation spectra.....	63
3.11	ZnTPP · I ⁻ photofragmentation mechanism	67
3.12	Conclusions	68
CHAPTER 4: ZnTPP and NiOEP radicals		
4.1	Introduction	71
4.2	Review of previous mass spectrometric studies on gas-phase TPP and OEP porphyrin and metalloporphyrins	72
4.3	Methods.....	73
4.4	[ZnTPP] ^{•+} radical cation CID and HCD	74
4.5	LDI dissociation of the [ZnTPP] ^{•+} and [ZnTPP] ^{•-} radicals.....	75
4.6	[ZnTPP] ^{•+} photodepletion and photodissociation spectra	77
4.7	[NiOEP] ^{•+} radical cation CID and HCD	79
4.8	LDI dissociation of the [NiOEP] ^{•+} and [NiOEP] ^{•-} radicals.....	82
4.9	[NiOEP] ^{•+} photodepletion and photodissociation spectra	83
4.10	Conclusions	86
CHAPTER 5: Verteporfin		
5.1	Introduction	87
5.2	Experimental methods.....	87
5.3	CID on verteporfin	88
5.4	Photodepletion and photofragmentation spectra	91
5.5	Photolysis.....	95
5.6	Conclusions	97

CHAPTER 6: Summary and future work	
6.1 Gas-phase complexes between MP and halide anions	99
6.2 ZnTPP and NiOEP radicals	100
6.3 Verteporfin.....	100
APPENDIX 1	
A1.1 Introduction	101
A1.2 ZnTPP · X ⁻ and (ZnTPP) ₂ · X ⁻ ESI/MS spectra	101
A1.3 HCD ZnTPP · X ⁻ and (ZnTPP) ₂ · X ⁻ ESI/MS spectra	103
A1.4 HCD of the ZnTPP · F ⁻ complex.....	106
A1.5 DFT optimised geometries of ZnP · X ⁻ , (ZnP) ₂ · X ⁻ and (ZnP) ₂	107
A1.6 Iodide and bromide photodepletion spectra.....	111
APPENDIX 2	
A2.1 Introduction on the software developed to analyse the data	113
A2.2 Collection of the mass spectra	113
A2.3 DataAnalysis AutomationEngine: First step.....	114
A2.4 Phyton scripts: Second Step.....	118
A2.5 Phyton original scripts used for the PD and PF spectra calculation	121
A2.6 CID plots scripts.....	136
Abbreviations and glossary.....	145
Bibliography.....	147

List of Tables

Chapter 3:

Table 3.1: Complexation energies of the $MP \cdot Cl^-$ cluster, using the simplified MP structure in Fig. 3.2, with $M = Mg, Zn, Cu(II), Ni(II), Fe(II)$.

Table 3.2: Complexation energies of the $MP \cdot I^-$ cluster, using the simplified MP structure in Fig.3.2, with $M = Mg, Zn, Cu(II), Ni(II), Fe(II)$.

Table 3.3: Theoretical complexation energies of $ZnP \cdot X^-$ complexes.

Table 3.4: Equilibrium constants for the $ZnTPP \cdot X^-$ complexes, where X^- is the ligand.

Table 3.5: Equilibrium constants for the Zinc Porphyrin Sensitizers both in a fluid propylene carbonate solution and anchored to Nanocrystalline TiO_2 .

Table 3.6: CE_{50} of for the sandwich (2:1) and single complexes (1:1) with halides in the gas-phase determined using the HCD technique.

Table 3.7: Partial charges on Zinc, halides, and nitrogens for the 1:1 $ZnP \cdot X^-$ complexes. In addition, the zinc-halide and zinc-nitrogen bond length are reported. The last column reports the bond angle between the halide, zinc, and nitrogen, which reflects the displacement of the zinc from the porphyrin ring plan.

Table 3.8: The amount of charge lost from the halide and transferred to the zinc atom and the organic part of the porphyrin. The negative sign indicates a decrease in electron density while the positive sign an increasing electron density.

Table 3.9: Theoretical structural data of the $(ZnP)_2 \cdot X^-$ complexes, including halide-Zn bond length and Zn-halide-Zn bond angle. The last row shows the distance between two ZnP molecules planes in a $(ZnP)_2$ dimer.

Table 3.10: Theoretical complexation energies of 2:1 ZnP complexes with halides corresponding to the reaction: $(ZnP)_2 \cdot X^- \rightarrow ZnP \cdot X^- + ZnP$. The last row shows the stabilisation energy between two ZnP molecules.

Table 3.11: VDE of the $ZnP \cdot X^-$ complexes compared to the VDE of the respective halide anion. The last row shows the uncomplexed ZnP molecule VDE. The third column represents the electron affinity of the halide neutral atoms (taken from Ref.83 and found to be equal to the computational calculated VDE).

Table 3.12: Soret peaks in the gas-phase and solution phase of ZnTPP · X⁻ complexes. The solution phase data are obtained in benzene from Nappa and Valentine's article. The last row shows the Soret peak of the ZnTPP in benzene(b) and MeCN.

Chapter 5:

Table 5.1: Fragments derived from CID on protonated verteporfin (parent ion peak m/z 719.20).

List of Figures

Chapter 1:

Figure 1.1: Basic structure of porphyrins (Porphin molecule).

Figure 1.2: a) The HOMO and LUMO orbitals of the porphyrin ring and b) The energy levels of the transition showing the ($S_0 \rightarrow S_2$) Soret and the ($S_0 \rightarrow S_1$) Q band transition.

Figure 1.3: Simplified molecular orbital diagram for metalloporphyrins. Interaction between metal $d\pi$ and π^* porphyrin orbitals occurs in hypsochromic shifts. The $d\pi$ metal orbital overlap with the π system of the porphyrin ring.

Figure 1.4: Meso-tetra (4-sulfonatophenyl) porphyrin (TPPS).

Figure 1.5: TPPS dimers and trimers.

Figure 1.6: Dissociation channels of FeTPP^+ (observed via CID).

Figure 1.7: Fragmentation cascade of 1,5,15,20-tetrakis(alpha-pyridinio-methylphenyl)-(2H)-porphyrin and correlation between experimentally determined fragmentation thresholds (E50% values) and dissociation energies calculated at the DFT level.

Figure 1.8: Schematic diagram of a molecular beam; the sample vapour molecules enter a vacuum chamber through a small hole. If the vapor pressure is sufficiently high a jet is formed and only the molecules traveling in the correct direction pass through a second hole. An additional velocity selector can be used.

Figure 1.9: 1:1 and 2:1 (bridged dimer) cluster of ZnTPP and halide anions (X^-).

Figure 1.10: Verteporphyrin molecules. The verteporphyrin for injection used in PDT (photodynamic therapy) is a 1:1 mixture of two regioisomers (I and II).

Chapter 2:

Figure 2.1: Schematic diagram showing the electrospray ionization (ESI). A voltage is applied between the spraying nozzle and the sample plate. The solution with the analytes flows through the nozzle and forms a Taylor cone due to the high voltage. The following Coulomb fission and solvent evaporation lead to droplets with a diameter that reaches 200nm or less. The charged analyte is eventually released in the gas-phase following two possible mechanisms (IEM or CRM). Image taken from ref.59.

Figure 2.2: Schematic of an ESI source. Taken from ref. 63

Figure 2.3: Schematic of the ion evaporation model (IEM) and charged residue model(CRM). In the IEM a charged analyte leaves the droplet (“evaporates”) while in the CRM the solvent evaporates completely. Ref.51

Figure 2.4: MALDI scheme. The Analyte and the matrix are irradiated by a laser pulse. A hot plume is formed, and the analyte is ionized. Image taken from Reference 70.

Figure 2.5: Schematic of the AmaZon Bruker laser coupled mass spectrometer. The ESI source is used to generate the gas-phase ions. The ions of interest are selected according to their m/z , isolated and injected into the quadrupole ion trap. The ion trap is modified so that the laser beam coming from an Nd-YAG pumped laser is directed into it and therefore can be absorbed by the trapped ions.

Figure 2.6: Ion cloud interaction with the focused laser beam in the ion trap. The size of the cross-section is not known therefore can range from a small portion to the whole ion cloud. On the right a fluorescence imaging of an ion cloud (approximate dimensions 0.80mm X 1.6mm) taken from Ref.75

Figure 2.7: Nickel octaethylporphyrin(NiOEP) mass spectra. Above with laser turned off and below with laser on at 366nm. The parent ion intensity (m/z 590.18) is lower with the laser on and many positively charged fragment products are observed.

Figure 2.8: Photolysis cell. A solution with the sample is inserted in a hole and a cap is added to block the light from the outside environment. In the hole there are a series of UV LEDs and the sample is kept there for a certain amount of time and then the photolysis products analyzed using mass spectrometry.

Chapter 3:

Figure 3.1: 1:1 and 2:1 (bridged dimer) cluster of ZnTPP and halide anions (X^-).

Figure 3.2: Porphyrin structure used for the computational evaluation of the complexation energies of metalloporphyrins with halides. ($M=Zn, Mg, Cu, Ni, Fe$).

Figure 3.3: Zinc Porphyrin Sensitizers anchored to mesoporous nanocrystalline (anatase) TiO_2 thin films (TiO_2/ZnP). Image taken from Reference 82.

Figure 3.4: HCD plots of the 2:1 complexes: (a) $(ZnTPP)_2 \cdot I^-$, (b) $(ZnTPP)_2 \cdot Br^-$, (c) $(ZnTPP)_2 \cdot Cl^-$, (d) $(ZnTPP)_2 \cdot F^-$. The relative intensity of the signals of the parent ions and fragments are plotted against the percentage of collision voltage relative to the highest offset available on the Orbitrap Fusion Tribrid mass spectrometer.

Figure 3.5: HCD plots of the dimers: (a) $ZnTPP \cdot I^-$, (b) $ZnTPP \cdot Br^-$, (c) $ZnTPP \cdot Cl^-$

Figure 3.6: DFT optimized structures: a) top and b) side view of $ZnP \cdot Cl^-$ complex. c) Side view of the only ZnP . The zinc atom is pulled out of the porphyrin ring due to the bond with chloride.

Figure 3.7: DFT optimized structure of the $(ZnP)_2 \cdot Cl^-$ complex. a) Side view, b) top view.

Figure 3.8: DFT optimization with different positions of the phenyls groups in ZnTPP. a) front view of the conformer with all the opposite phenyls parallels ($//$). b) lateral view of the "parallel" and "cross" position of the phenyls. All the conformers are equally stable

Figure 3.9: The phenyl group in the slightly bent conformation minimizes the sterical interactions(c). a) Dihedral angle 0° , b) dihedral angle 90° and c) minimal energy structure with a dihedral angle of 109.2° where the hydrogens that are shown are at the maximum distance from each other.

Figure 3.10: Schematic to illustrate the difference between vertical and adiabatic ionization energy in case of an anion.

Figure 3.11: UV-Vis spectrum of a solution of ZnTPP in acetonitrile. Above spectrum in the range 380-620nm and below Q-bands zoomed in.

Figure 3.12: PD dependency on the cut off value(m/z).

Figure 3.13: Photofragments laser off and laser on mass spectrum of $ZnTPP \cdot Br^-$, excited at photodepletion maxima of 318 nm

Figure 3.14: a) Gas-phase UV absorption (photodepletion) spectra of $ZnTPP \cdot Br^-$ (b and c) Photofragment production spectra of the photofragments, $ZnTPP \cdot^-$ and Br^- respectively. The solid line is a five-point adjacent average of the data points. The laser

pulse energy was set at 0.2 mJ in the UV region and 0.6 mJ in the visible (400-600 nm). VDE 3.2 eV corresponding to 387 nm.

Figure 3.15: Photofragment laser off and laser on mass spectrum of $\text{ZnTPP} \cdot \text{Cl}^-$, excited at photodepletion maxima of 310 nm.

Figure 3.16: a) Gas-phase UV absorption (photodepletion) spectra of $\text{ZnTPP} \cdot \text{Cl}^-$ (b) Photofragment production spectra of the photofragment $\text{ZnTPP} \cdot^-$. The solid line is a four-point adjacent average of the data points. The laser pulse energy was set at 0.05 mJ.

Figure 3.17: Photofragment laser off and laser on mass spectrum of $\text{ZnTPP} \cdot \text{F}^-$, excited near photodepletion maxima at 318 nm.

Figure 3.18: a) Gas-phase UV absorption (photodepletion) spectra of $\text{ZnTPP} \cdot \text{F}^-$ (b and c) Photofragment production spectra of the photofragment $\text{ZnTPP} \cdot^-$ and $(\text{ZnTPP} - \text{C}_6\text{H}_6) \cdot^-$, respectively. The solid line is a five-point adjacent average of the data points. The laser pulse energy was set at 0.3 mJ.

Figure 3.19: Photofragment laser off and laser on mass spectrum of $\text{ZnTPP} \cdot \text{I}^-$, excited at 305 nm.

Chapter 4:

Figure 4.1: Schematic of the a) ZnTPP and b) NiOEP porphyrins.

Figure 4.2: $[\text{ZnTPP}] \cdot^+$ CID: a) MS spectra at 45% CID voltage b) relative intensity of the precursor molecule and fragments versus collision voltage.

Figure 4.3: $[\text{ZnTPP}] \cdot^+$ HCD: a) MS spectra at 45% HCD voltage b) relative intensity of the precursor molecule and fragments versus collision voltage.

Figure 4.4: ZnTPP LDI MS spectra: a) positive ion mode b) negative ion mode.

Figure 4.5: Photofragment laser off (top) and laser on (bottom) mass spectrum of $[\text{ZnTPP}] \cdot^+$, excited near the photodepletion maxima at 396 nm.

Figure 4.6: a) Gas-phase UV absorption (photodepletion) spectra of $[\text{ZnTPP}] \cdot^+$ (b and c) Photofragment production spectra of the photofragment m/z 598.06 ($\text{ZnTPP} - \text{C}_6\text{H}_6$) \cdot^+ and m/z 522.02 ($\text{ZnTPP} - \text{C}_{12}\text{H}_{10}$) \cdot^+ , respectively. The solid line is a five-point adjacent average of the data points. The laser pulse energy was set at 0.05 mJ.

Figure 4.7: $[\text{NiOEP}] \cdot^+$ CID: a) MS spectra at 45% CID voltage b) relative intensity versus collision voltage. Data obtained with the Orbitrap mass spectrometer.

Figure 4.8: [NiOEP]⁺CID: a) MS spectra at 0.8V b) relative intensity versus collision voltage. Data obtained with the AmaZon mass spectrometer.

Figure 4.9: [NiOEP]⁺HCD: plot of the relative fragmentation intensities versus % collision voltage.

Figure 4.10: NiOEP LDI MS spectra: a) positive mode b) negative mode.

Figure 4.11: UV-Vis spectra of a solution of $6 \cdot 10^{-6}$ NiOEP in acetonitrile.

Figure 4.12: Photofragment laser off (top) and laser on (bottom) mass spectrum of [NiOEP]⁺, excited near the photodepletion maxima at 368 nm. Laser pulse 0.1mJ.

Figure 4.13: Gas-phase UV absorption (photodepletion) spectra of [NiOEP]⁺ and Photofragment production spectra of the major fragments. The solid line is a four-point adjacent average of the data points. The laser pulse energy was set at 0.05 mJ

Chapter 5:

Figure 5.1: CID of protonated verteporfin: a) MS spectra averaged across the whole CID voltage range. b) Plot of relative intensity against CID voltage. A vertically expanded view of the CID results is shown on the bottom right.

Figure 5.2: Scheme of the neutral fragments lost when CID is applied to protonated verteporfin. The proposed fragments are deduced from the observed peaks; the difference between the parent ion and the positive fragments observed is taken and assigned to a loss of a smaller neutral molecule.

Figure 5.3: UV-Vis spectra verteporfin in MeCN.

Figure 5.5: Photodepletion spectra of protonated verteporfin (black) and 3 photofragmentation spectra as examples (m/z 687.2, 659.2, 645.2). Laser pulse 0.05 mJ (400-260 nm), 0.3 mJ (402 nm to 600 nm) and m/z 200 cut-off.

Figure 5.6: Photodepletion spectra of protonated verteporfin (black) and 3 photofragmentation spectra as examples. Laser pulse 0.2 mJ (600-800nm). Really low PF peak intensity (less than 0.2/0.3% of the Soret peak signal). 200 m/z cut-off

Figure 5.7: Mass spectra: a) after 2h exposure at 310nm. b) after 2h exposure 365nm. c) after 20min exposure 689nm(OPO).

Figure 5.8: Proposed reaction scheme that leads to the main fragmentation product at 435.42m/z.

Appendix:

Figure A1.1: MS spectra of $\text{ZnTPP} \cdot \text{X}^-$ and $(\text{ZnTPP})_2 \cdot \text{X}^-$ complexes. All the isotopic peaks are displayed.

Figure A1.2: MS spectra of $\text{ZnTPP} \cdot \text{X}^-$ complexes when HCD is applied.

Figure A1.3: MS spectra of $(\text{ZnTPP})_2 \cdot \text{X}^-$ complexes when HCD is applied.

Figure A1.4: MS spectra of the $\text{ZnTPP} \cdot \text{F}^-$ complex at HCD 40%.

Figure A1.5: Front and side view of the DFT optimized structure of $\text{ZnP} \cdot \text{X}^-$ complexes.

Figure A1.6: Front and side view of the DFT optimized structure of $(\text{ZnP})_2 \cdot \text{X}^-$ complexes.

Figure A1.7: Front and side view of the DFT optimized structure of $(\text{ZnP})_2$ aggregates.

Figure A1.8: Photodetachment spectra of the bare I^- ion. Adapted from Ref.118

Figure A1.9: a) and b) Gas-phase UV absorption (photodepletion) spectra of Iodide and Bromide respectively. The solid line is a five-point adjacent average of the data points. The laser pulse energy was set at 0.30 ± 0.10 mJ for both the anions.

Acknowledgments

Firstly, I would like to thank my supervisor Caroline Dessent for all the support and opportunities provided during this year.

I would also like to thank all the CED group, in particular, Rosaria Cercola for her help and patience and Jacob Berembein who helped me with the laser experiments. I wish to thank also Conor Rankine for his IT and computational support and the experimental officer, Ed Bergstrom for teaching me how to operate the mass spectrometers, troubleshooting the technical problems and answering my many questions.

Lastly, I wish to thank the summer students Olivia and Nick for bringing me joy and motivation every day in the office.

Declaration

I declare that this thesis is a presentation of original work and I am the sole author. This work has not previously been presented for an award at this, or any other, University. All sources are acknowledged as References.

Chapter 1: Introduction

1.1 Applications of porphyrins and metalloporphyrins

The initial light absorption in all photosynthetic organisms is due to pigments that are subdivided into three major groups: chlorophylls, carotenoids, and phycobilins. These pigments are conjugated π -electron systems and have exceptionally high molar extinction coefficients about $1 \times 10^5 \text{ M}^{-1} \text{ cm}^{-1}$.¹

Worldwide it is estimated that total energy conversion via photosynthesis is well over 100 TW, dwarfing the total amount of energy used by humans (about 13 TW in 2005).² In the attempt to create compatible successful systems, porphyrins have raised a lot of interest for the development of new light-harvesting materials: synthetic porphyrin are now incorporated in prototype dye-sensitized solar cells, and potentially they can match the success of the best of dyes.^{2,3,4}

Parallel growing numbers of studies have been done on catalysts for solar chemistry, such as water splitting or CO₂ reduction^{5,6} with complexes of meso-tetraphenylporphyrin and octaethylporphyrin being a focus in this field. Complexes with Mn, Fe, and Co catalyze a variety of reactions of potential interest in organic synthesis.⁷

In addition, in recent years, the use of porphyrins and metalloporphyrins in the biomedical field has increased substantially: the photochemical, photophysical, and photoredox properties of these molecules that are tuneable through structural modifications, and their low in vivo toxicity, have been brought into wide application in photodynamic therapy (PDT)⁸ leading to successful results like in the treatment of macular degeneration using verteporfin.⁹

PDT is considered a non-invasive cancer treatment, involving the interaction between light of a determined frequency, a photosensitizer, and oxygen. This interaction leads to the formation of a highly reactive oxygen species (ROS), usually singlet oxygen, as well as superoxide anion, free hydroxyl radical, or hydrogen peroxide.¹⁰ These highly reactive oxygen species react with cellular organic biomolecules such as lipids, aromatic amino

acids, and nucleic acids to produce oxidative radicals that damage the cell, possibly inducing apoptosis or even necrosis.^{10, 11}

PDT has found application also in the treatment of bacterial infections, such as acne¹²; bacteria have been shown to produce porphyrins endogenously¹³, which are therefore susceptible to photoexcitation and subsequently death after light treatment.

1.2 Structure and spectroscopic properties of porphyrins

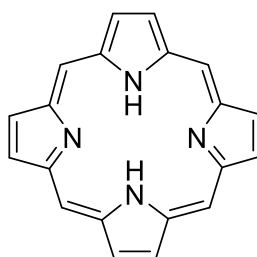


Figure 1.1. Basic structure of porphyrins (Porphin molecule).

The word porphyrin is derived from the Greek porphura, meaning purple. They are, in fact, a large class of deeply coloured pigment, of natural or synthetic origin. They consist of a macrocyclic aromatic system consisting of four pyrrole units joined by four methine groups. Porphin is the simplest porphyrin, and its chemical structure is the common structure motif (Fig. 1.1). This basic macrocycle can be substituted in many ways, and the central cavity can bind different metals, forming a metalloporphyrin. The most famous metalloporphyrins in biological systems, are heme (iron porphyrin) and chlorophylls (magnesium porphyrins).

Porphyrins are characterized by high molar extinction coefficients and their characteristic absorption profile, which is defined by an intense Soret or B band at around 400 nm, and a series of weaker Q bands at around 550 nm. The origins of these transitions have been explained by Gouterman's four orbitals model in D_{4h} symmetry.¹⁴ In this theory, the two fundamental concepts are:

- 1) The two absorption bands are due to transitions between two HOMO and two LUMO orbitals (π to π^* transitions)
- 2) The ring substitution and the metal center influence the relative energies of those orbitals.

In this model, the LUMO's are both e_g , and the two HOMO's are a_{1u} and a_{2u} . This means that there are two possible singlet excited states: $a_{1u}e_g$ and $a_{2u}e_g$

Orbital mixing splits these two excited singlet states into two 1E_u states. The electronic transition to the higher energy mixed state ($S_0 \rightarrow S_2$), is strongly allowed, whereas a transition to the lower energy mixed state, the ($S_0 \rightarrow S_1$), is only weakly allowed.¹⁴

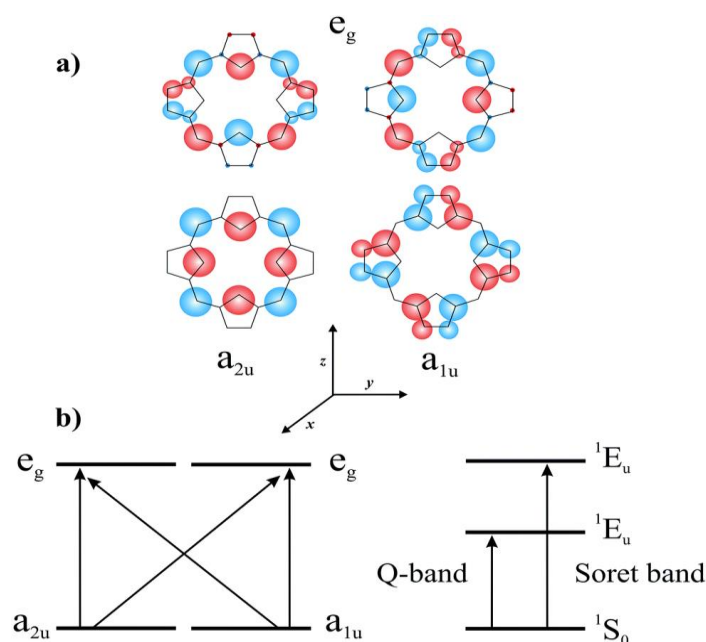


Figure 1.2. a) The HOMO and LUMO orbitals of the porphyrin ring and b) The energy levels of the transition showing the ($S_0 \rightarrow S_2$) Soret and the ($S_0 \rightarrow S_1$) Q band transition. Image adapted from Ref.15

In the case of metalloporphyrins, the nature of the metal determines how the UV-Vis spectrum changes; metalloporphyrins are subdivided into two major groups: regular metalloporphyrins contain closed-shell metal ions (d^0 or d^{10}) —for example Zn(II), while in hypso-porphyrins metals have a d^x , with $x = 6$ to 9 configuration —for example Ni(II).¹⁶

In regular metalloporphyrin, the metal has very little effect on the porphyrin π to π^* energy gap because of the low energy of the $d\pi$ (d_{xz} , d_{yz}) metal-based orbitals. In hypso-porphyrins there is a significant metal $d\pi$ to porphyrin π^* orbital interaction (metal to ligand π -backbonding), resulting in an increased porphyrin π to π^* energy separation causing the electronic absorptions to undergo hypsochromic (blue) shifts (Fig. 1.3).¹⁶

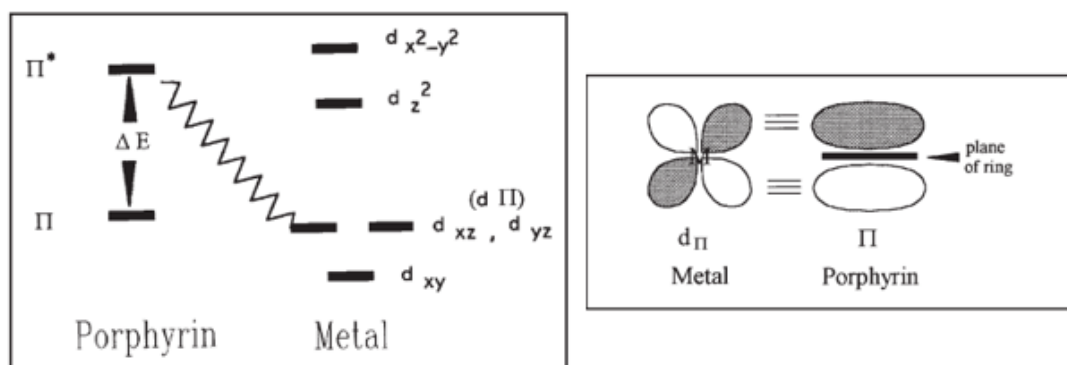


Figure 1.3. Simplified molecular orbital diagram for metalloporphyrins. Interaction between metal $d\pi$ and π^* porphyrin orbitals occurs in hypso-porphyrins. The $d\pi$ metal orbital overlap with the π system of the porphyrin ring. Image adapted from Ref.16.

Another effect of the metalation of the porphyrin is the reduction of the number of the observed Q bands due to the increased degree of symmetry.¹⁶

1.3 The importance of Gas-phase studies on Metalloporphyrins

Although porphyrins in biological systems or artificial materials occur in condensed phase media, gas-phase experiments are more suitable for theoretical and fundamental studies because of the lower complexity of the isolated system. Gas-phase spectra also serve to benchmark theoretical models that predict the energies of electronically excited states. However, in gas-phase spectroscopy it is not routinely possible to record the

absorption spectra of molecules in the conventional way, measuring the light before and after the sample to quantify the loss in intensity, because there is not a large enough number of ions to detect any change in light intensity. Therefore photon absorption is identified from ionic fragmentation of the precursor molecule or cluster (*action spectroscopy*).¹⁷

As pointed out by S.B. Nielsen in a conference paper in 2012,¹⁷ another fundamental aspect of gas-phase studies is the possibility of revealing the intrinsic electronic properties; the electronic structure of a biochromophore (i.e., light absorber) is strongly perturbed by its environment, e.g., water or amino acid residues within protein pockets, and it is, therefore, valuable to study isolated molecules *in vacuo*. In this paper, S.B. Nielsen presented the first *action spectrum* and *photodissociation* mass spectrum of isolated Fe(III)-heme cations showing that the bulky environment around the heme does cause a red-shift in the $\pi\pi^*$ transition energy.¹⁷

In following studies, S.B. Nielsen and co-workers determined the intrinsic absorption spectrum of isolated gas-phase chlorophyll pigments revealing the effect of the protein microenvironment.¹⁸ They determined a large difference in the absorption spectrum of Chl a and Chl b forms, which they concluded to be an intrinsic effect and not due to local hydrogen-bond interactions with the formyl group of Chl b, for example. This work clearly demonstrated the advantage of looking at isolated molecules. They also determined that the absorption *in vacuo* was blue-shifted by 50 nm compared to natural protein complexes.

In a subsequent gas-phase study with Chl a dimers, they addressed the question of whether this 50 nm shift is due to interactions with the protein environment or excitonic coupling between chlorophyll pigments. They found that chlorophyll association alone can produce a large portion of the colour shift observed in photosynthetic macromolecular assemblies.¹⁹

1.4 Gas-Phase studies on non-biological Metalloporphyrins

Although in nature, metalloporphyrins are generally iron or magnesium-based, there are a few examples of natural different metal choices. For example, coenzyme F430 is a Ni(I) porphyrin involved in methane production by methanobacterium thermoautotrophicum.^{20, 21} Also, a zinc porphyrin photosynthetic system was found in *addiphilium rubrum* bacteria showing the potentiality of using different metals.²²

For human health applications, it's important to explore properties of different porphyrins with a wide variety of metals and side chains substitutions. Furthermore, this can provide insight into fundamental biological questions such as the reasons for the occurrence of the magnesium porphyrin in photosynthesis or showing that alternative organic substitutions in biological porphyrins could have led to the disruption of their functions.

In a pioneering study, *rhodobacter sphaeroides* bacteria were engineered so that bacteriochlorophyll (BChl) -binding sites contain Zn-BChl rather than BChl a showing an electron transfer efficiency of >95% of the wild-type reaction center.²³ More work needs to be done in the direction of bioengineering photosynthesis with different porphyrins, and this is another future research field that could grow from a fundamental knowledge of different porphyrins properties.

Over recent years, many gas-phase studies have been conducted on non-biological porphyrins by M.M.Kappes and co-workers. The Kappes group focuses on gaseous anionic metalloporphyrin systems, using *photoelectron spectroscopy*: one initial system studied was meso-tetra(4-sulfonatophenyl)porphyrin (TPPS) multianions (Fig.1.4).²⁵

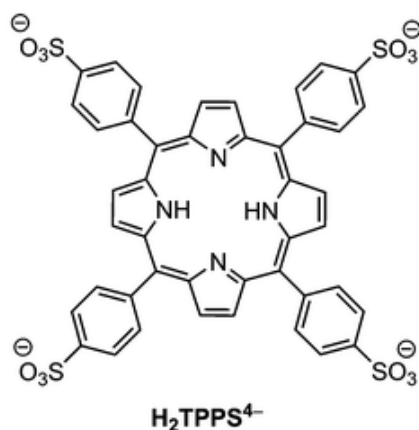


Figure 1.4 meso-tetra(4-sulfonatophenyl) porphyrin (TPPS). Adapted from Ref.24

TPPS was first used by Kappes *et al.* in 2013 where structures and photoelectron spectra of Mn(III) and Cu(II) TPPS multianions, as well as of homomolecular dimers and trimers (Fig.1.5) were determined.²⁵ The charge-dependent shifts they observed in the photoelectron spectra were explained by a simple electrostatic model.^{26, 27} The key assumptions of this model are that the HOMO is largely localized in the central part of the metalloporphyrin (either on the metal atom or on the nitrogen atoms surrounding it) and that the negatively charged sulfonic acid groups are involved only indirectly, by influencing the electrostatic potential experienced by the outgoing electron.

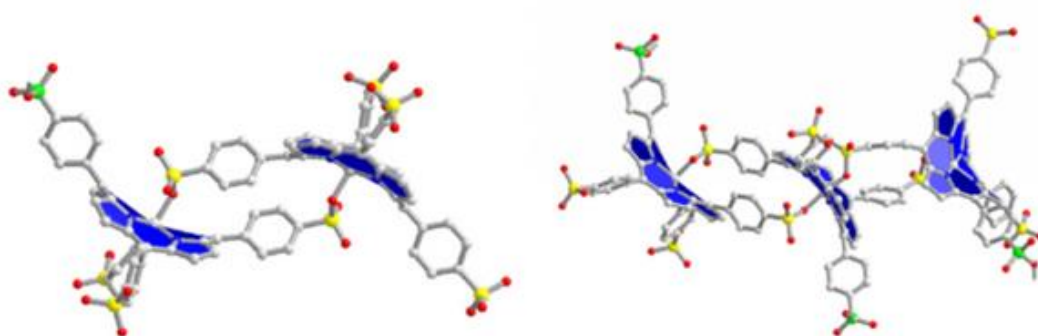


Figure 1.5 TPPS dimers and trimers. Figure taken from Ref.25

Subsequently, Kappes and co-workers used the Fe(II) and Mn(II) TPPS metalloporphyrins to determine the first experimental binding energies of molecular oxygen and carbon monoxide to model metal porphyrin complex ions in vacuo.²⁸

This gas-phase experiment offers the advantage that the oxidation state of the metal center is controlled since the ions are selected using the mass-to-charge ratio. Therefore, coupling mass spectrometry when working with species with multiple oxidation states is of great advantage.

Kappes' group also determined the influence of the oxidation state of the central transition metal on the binding energy with oxygen.²⁹ Particular emphasis has been placed on the different chemical behavior of the Fe and Mn systems as a function of their +II versus +III oxidation states. They proved that only open-shell d-metal porphyrins in their oxidation state +II have a sizable O₂ binding energy of 40.8 and 67.4 kJ/mol (for Fe(II) and Mn(II), respectively), whereas the Cu has a much lower dioxygen affinity (< 22

kJ/mol). They experimentally showed that metal-to-oxygen electron transfer plays a significant role in O₂ binding. In fact, O₂ is much less reactive toward the trivalent species [Fe(III)TPPS]³⁻ and [Mn(III)TPPS]³⁻, for which further metal-to-oxygen electron transfer is more difficult.²⁹

In another study, using photoelectron and action spectroscopies, the response of isolated Pd(II) meso-tetra(4-sulfonatophenyl)porphyrin tetraanions ([PdTPPS]⁴⁻) to electronic excitation was revealed together with their decay channels.³⁰ Primarily, electron detachment is observed together with small amounts of SO₂⁻ and SO₃⁻ loss. Kappes *et al.* found a peak centered at 524 nm corresponding to the Q band transition and another peak at or below the low-wavelength range limit of the OPO laser (410 nm) they used, corresponding to the Soret band transition. Compared to the solution-phase (water) absorption spectrum this represents a blue shift of the Soret band (412 → <410 nm) and a small red shift of the Q band transition (524 → 521 nm).

More recently in 2018, Kappes's group has identified the photodissociation pathways of gaseous monomeric and dimeric M(II)-meso-tetra-(4-sulfonatophenyl)-porphyrin (with M = Pd(II), Cu(II), Zn(II)) multianions.³¹ In these porphyrins, the position of the Q-band (S₀ → S₁ transitions) was studied as a function of charge state, counterions, oligomerization, and dimer structure type. Both charge-state variation and the type of associated counterion have only a minor effect on the Q-band absorption maxima, although, for the homodimers, a consistent 10 nm blue-shift of their Q-bands from the 3⁻ to the 5⁻ charge state was reported.

1.5 ESI technique and CID studies on (metallo)porphyrins

Electrospray ionization (ESI) is a technique used in mass spectrometry to produce ions using an electrospray in which a high voltage applied to a liquid to create an aerosol.

The ESI technique necessitates charged species, so to study a neutral molecule, a charged group or “tag” can be attached to the molecule of interest while ensuring it is at sufficient distance from the chromophore to not affect the absorption. This charged group allows the species to be electrosprayed but maintains the chromophore close to a neutral state. If this group is at enough distance, then the spectrum is the same as the hypothetical neutral chromophore in gas-phase. This method was used by S.B. Nielsen et al. to study isolated chlorophyll a and b using quaternary ammonium ions as tags.^{18,32}

A similar approach of using a “tag” was developed using formate anion (HCOO^-) coordination to neutral metalloporphyrins and -phthalocyanines containing divalent metals as a mean to improve their ion formation in electrospray ionization (ESI). This method is particularly useful when the oxidation of the metal coordinated to the porphyrin makes it overall neutral.³³

Collision induced dissociation (CID) is a mass spectrometry technique used to induce fragmentation of selected ions in the gas phase.³⁴ The selected ions (typically molecular ions or protonated molecules) are usually accelerated by applying an electrical potential to increase the ion kinetic energy and then allowed to collide with neutral species (often helium, nitrogen, or argon). During the collision, some of the kinetic energy is converted into internal energy, which results in bond breakage and the fragmentation of the molecular ion into smaller fragments.³⁵

The CID technique was applied by D.K. Bohme and co-workers to study the dissociation of tetraphenyl iron and manganese porphyrin ions.³⁶ They showed that the dissociation channels for both these porphyrins are the same. The results are summarised in Fig.1.6 for the iron tetraphenyl porphyrin.

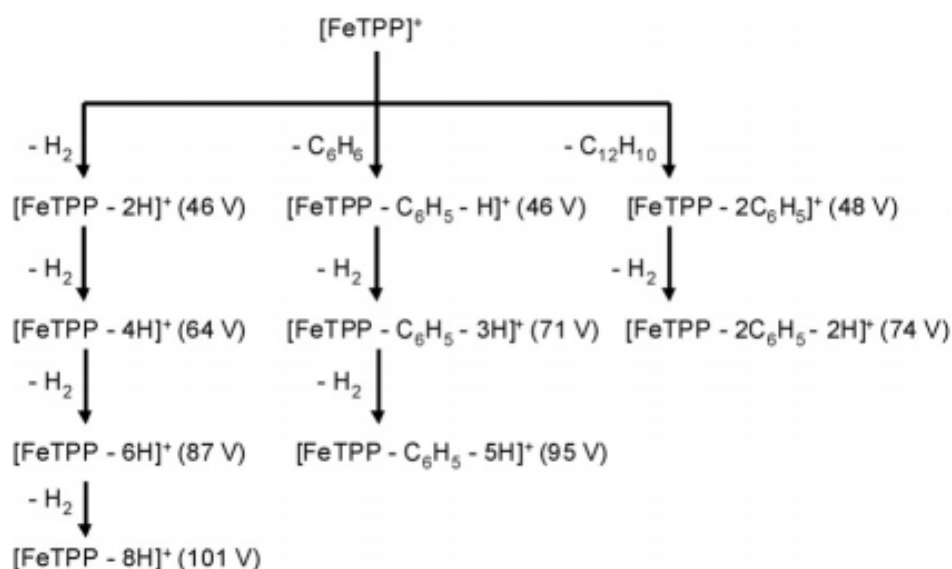


Figure 1.6 Dissociation channels of FeTPP^+ (observed via CID). Figure taken from Ref.36

In an article by M.M. Kappes and co-workers, benzylpyridinium-substituted porphyrins were studied using CID, and they found a linear correlation between experimental fragmentation thresholds and theoretical dissociation energies, suggesting that these species can be used as calibrants to gauge the fragmentation energetics of closely related systems (Fig.1.7).³⁷

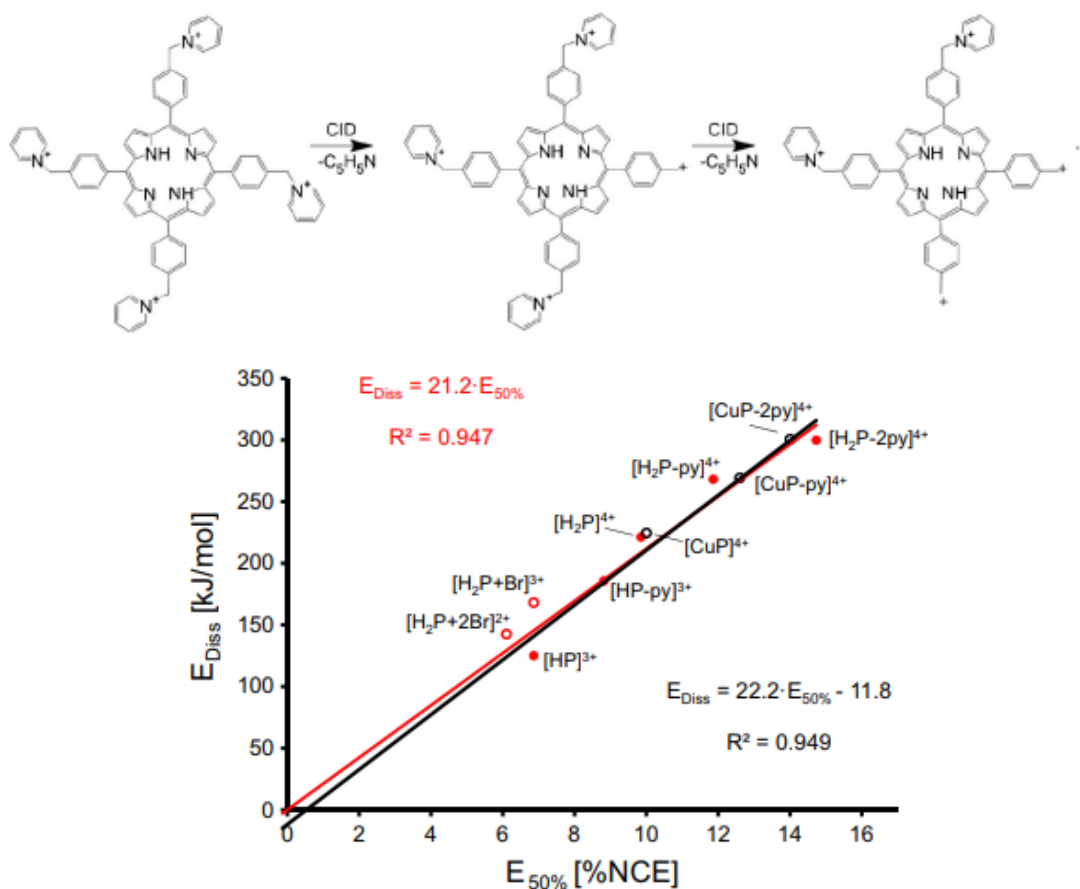


Figure 1.7 Fragmentation cascade of 1,5,15,20-tetrakis(alpha-pyridinio-methylphenyl)-(2H)-porphyrin and correlation between experimentally determined fragmentation thresholds ($E_{50\%}$ values) and dissociation energies calculated at the DFT level. Figure taken from Ref.37

1.6 Metalloporphyrins and molecular beams

A molecular beam is produced by allowing gas to enter a vacuum chamber through a small hole in a box. This box contains vapour of the molecules that are to make up the beam (Fig.1.8). At low pressures of vapor in the box, when the free path of the molecules is greater than the width of the exit hole, the molecules will effuse through the hole; at higher pressures, they will flow through the forming a jet. The jet rapidly expands in the vacuum until the molecules move independently and only those molecules moving in the

proper direction to pass through a second hole become part of the beam while the others are pumped away. In addition, a velocity selector can be used to allow only molecules within a small range of speeds to pass through.³⁸ This technique provides a source of cold “isolated” molecules, characterized by strong rotational and vibrational cooling.³⁹

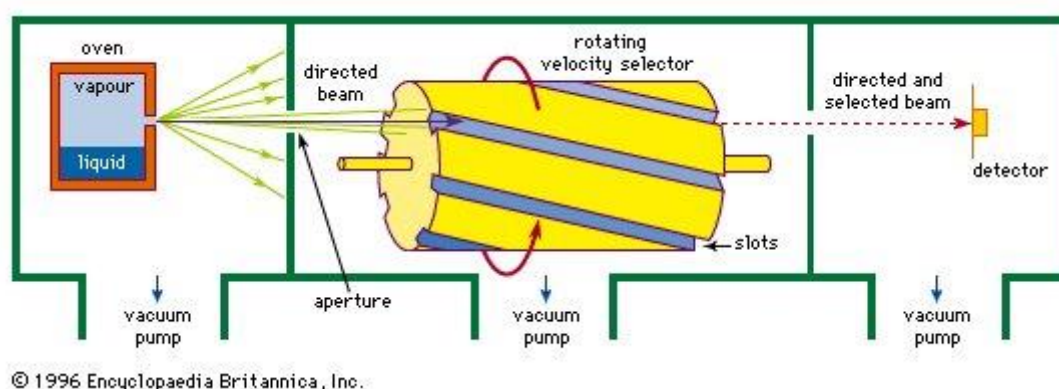


Figure 1.8 Schematic diagram of molecular beam apparatus; the sample vapour molecules enter a vacuum chamber through a small hole. If the vapour pressure is sufficiently high a jet is formed and only the molecules traveling in the correct direction pass through a second hole. An additional velocity selector can be used. Figure taken from Ref.38

In 1981, Joshua Jortner and co-workers successfully applied this technique to study the excited states of neutral gaseous MgTPP⁴⁰ and ZnTPP.⁴¹ More recently in 2010, Hudson *et al.* studied the first infrared spectra of jet-cooled free base and Cu (II) complex of protoporphyrin IX, produced in a molecular beam.⁴² In these experiments, they were able to clearly resolve the spectral features associated with the OH and NH vibrational transitions.

1.7 Porphyrin systems studied in this project

In this thesis, firstly gas-phase experiments of neutral metalloporphyrin (MP) *aggregates* with halides (zinc tetraphenyl porphyrin (ZnTPP), with F^- , Br^- , Cl^- , I^-) are presented. Those neutral MP molecules can not be charged by typical ESI processes (i.e. protonation, deprotonation), however, the negatively charged halides allow the use of the ESI technique acting similarly to a “tag”, but in this case, perturbing considerably the ZnTPP electronic spectrum. They also offer the possibility of forming bridged complexes where the halide sits between the porphyrins (Fig.1.9, and appendix A1.5). Similar to the case of the iodide ion-pyrimidine *clusters* studied previously in the Dessent group⁴³ choosing a halide ion-neutral MP complex allows us to study the near-threshold excitation and to explore the free-electron neutral molecule interaction, thus providing a route for studying the electron capture properties of metalloporphyrins.

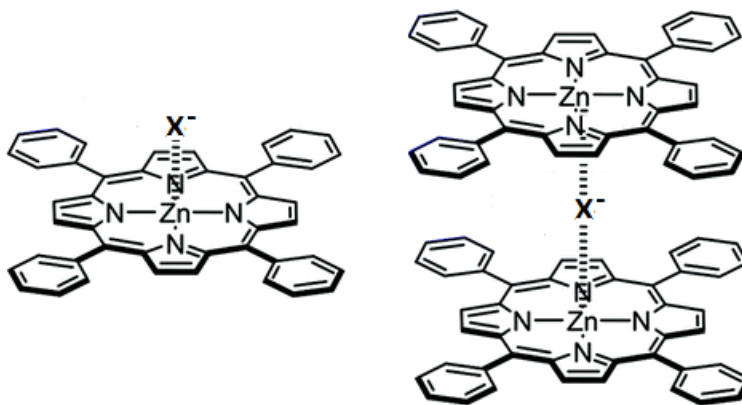


Figure 1.9. 1:1 and 2:1 (bridged) cluster of ZnTPP and halide anions (X^-).

Subsequently, the first gas-phase spectra of metalloporphyrins radicals are presented. Gas-phase ZnTPP and nickel octaethylporphyrin (NiOEP) positive radicals are obtained using the ESI technique and their photodissociation pathways compared with the CID results.

This thesis also includes a study on the benzoporphyrin derivative Verteporfin (trade name Visudyne, Fig.1.10). This is used as an injected medicine acting as photosensitizer for photodynamic therapy in the wet form of macular degeneration (also called subfoveal choroidal neovascularization, CNV). In this illness, abnormal blood vessels grow under the retina and macula causing bleed and leak of fluid, resulting in distorted or destroyed central vision. After being injected into the patient bloodstream, Verteporfin accumulates in these blood vessels and, when stimulated by a nonthermal red light with a wavelength of 689 nm in the presence of oxygen, produces highly reactive short-lived singlet oxygen and other reactive oxygen radicals, resulting in local damage to the endothelium and blockage of the vessels.^{44,45}

In this thesis, the action spectrum of gas-phase protonated verteporfin were acquired together with CID (collision-induced dissociation) studies and laser photodissociation, to better characterize the intrinsic properties of the verteporfin system. In addition, solution-phase photolysis experiments in the UV and visible range were performed to study its photoinduced fragmentation in the condensed phase, possibly showing additional mechanisms that enhance the cytotoxicity of the photolyzed verteporfin.

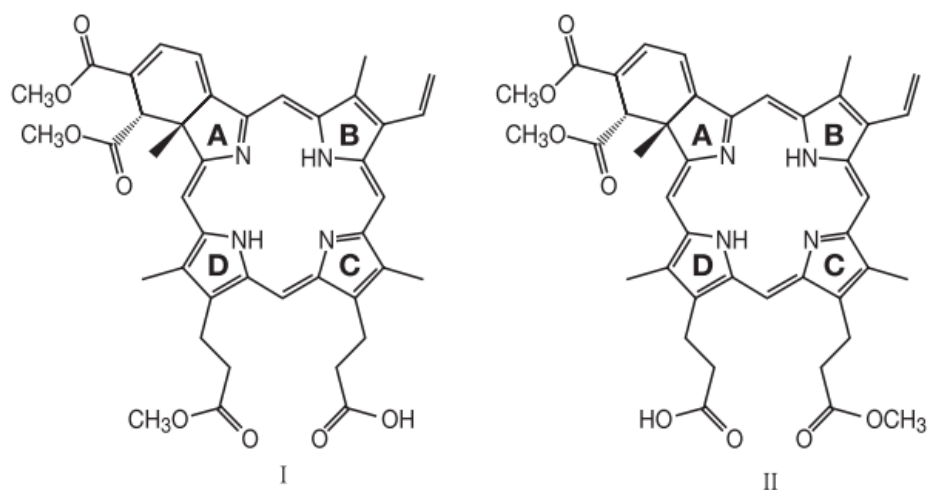


Figure 1.10 Verteporfin molecules. The verteporfin for injection used in PDT (photodynamic therapy) is a 1:1 mixture of two regioisomers (I and II).⁴⁴

1.8 Aims of the project

The project is constituted of three parts; the first part is focused on the neutral metalloporphyrin aggregates with halides, the second part on the radicals of neutral metalloporphyrins, and the third part on verteporfin gas-phase spectrum and fragmentation products.

Aims of the first part:

- 1) Investigation of whether it is possible to form halide metalloporphyrin (MP) aggregates in the gas phase using electrospray ionization.
- 2) Calculation of the vertical detachment energies (VDEs) of the aggregates to establish whether these are in a range that is accessible by our laser.
- 3) Investigation of photoexcitation of the complexes across the electron detachment threshold region to initiate electron transfer from the halide ion (X^-) to the MP, and follow any electron-transfer products.
- 4) Measurement of the gas-phase spectra of MP aggregates, to understand how the electronic bands (Soret and Q) evolve as a function of porphyrin aggregation.
- 5) Perform photodissociation experiments on MP aggregates, to characterize the photodegradation pathways.

Aims of the second part:

- 1) Obtain gas-phase radicals of neutral metalloporphyrins (ZnTPP, NiOEP)
- 2) Obtain the first gas-phase spectra of those radicals and compare the photofragmentation products with the collision-induced fragmentation pathways.

Aims of the third part:

- 1) Determine the first gas-phase spectra of verteporfin and characterize its photodegradation pathways.
- 2) Compare the gas phase results with the photolysis experiments in solution.

Chapter 2: Experimental techniques

2.1 Introduction to the experimental techniques

The porphyrins and metalloporphyrin (MP) analyzed in this thesis were characterized by different experimental techniques.

ZnTPP and its aggregates with halide anions were first studied computationally using density functional theory (DFT). Experimentally, these gas-phase aggregates were formed using electrospray ionization (ESI). Then collision-induced dissociation (CID) and higher energy collisional dissociation (HCD) were applied to determine the fragmentation products and the relative binding energy with the halides. Lastly, the gas-phase action spectra of these aggregates were determined using the commercial AmaZon Bruker mass spectrometer coupled with an OPO laser source, i.e. Laser Interfaced Mass Spectrometer (LIMS).

NiOEP and ZnTPP gas-phase radicals were formed with ESI and laser desorption ionization (LDI). HCD studies were performed on these radicals using the Orbitrap mass spectrometer while the gas-phase action spectrum using the LIMS.

Lastly, verteporfin fragmentation and photofragmentation channels were studied with CID and on the LIMS instrument, respectively. The solution-phase photolysis experiments were performed on home-built photolysis cells.

In summary, the techniques applied in this project are:

- 1) Computational density functional theory methods (DFT)
- 2) Electrospray ionization (ESI) to generate the gas-phase protonated/deprotonated ions, radicals, and aggregates/complexes.
- 3) Laser Desorption Ionization (LDI) to generating metalloporphyrin gas-phase radicals.
- 4) Collision induced dissociation (CID) and higher energy collisional dissociation

- (HCD) to determine the thermal fragmentation products.
- 5) Laser interfaced mass spectrometer (LIMS) to obtain the photodepletion and photofragmentation spectra.
 - 6) Photolysis of solutions at different wavelengths to determine the photofragmentation products.

2.2 Density Functional Theory (DFT)

Density functional theory (DFT) is a computational quantum mechanical modeling method used in chemistry to investigate the electronic structure of atoms and molecules. This theory uses functionals (functions of another function) to predict the properties of many-electron systems, treating the energy of interacting electrons as a functional of the electron density. This approach is based on the two Hohenberg-Kohn theorems: the ground state properties of a many-electron system depend only on the electronic density $n(x,y,z)$ and the correct ground state density for a system is the one that minimizes the total energy through the functional $E[n(x,y,z)]$.⁴⁶ This approach speeds up the calculations considerably because the electron density is a function of only three variables (x, y, z).

In this thesis, DFT studies were performed to determine and compare the complexation energies between different metalloporphyrins (MP) and halides (X) and provide insights into their interaction. These DFT calculations also provided the optimized lowest energy structures in the gas phase.

2.3 Electrospray Ionisation (ESI)

Electrospray ionization (ESI) is an atmospheric pressure technique used to transfer ionized species from a solution to the gas-phase.^{47,48,49} The transferred charged species are characterized by minimal fragmentation, and because of this feature, ESI is considered a soft ionization technique.^{50,51} ESI is often coupled with mass spectrometry to produce gas-phase ions that can be directed into the instrument.⁵²

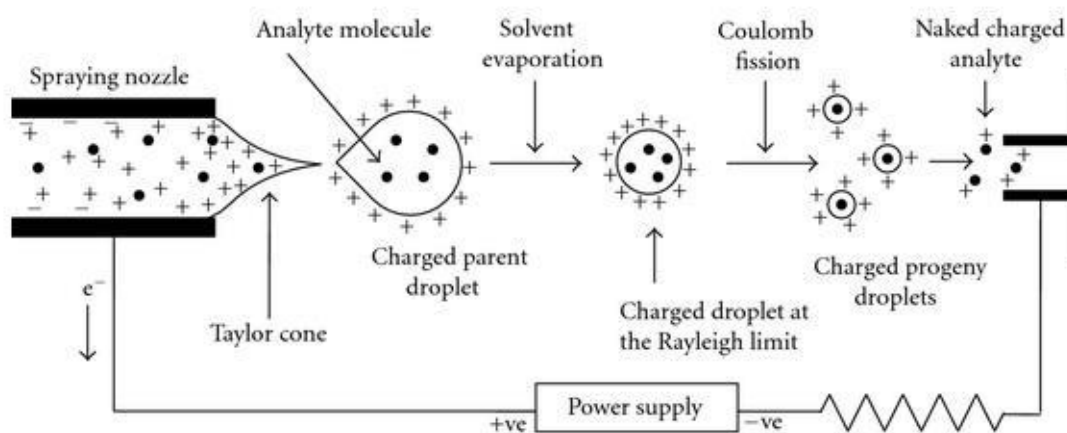


Figure 2.1 Schematic diagram of the electrospray ionisation (ESI). A voltage is applied between the spraying nozzle and the sample plate. The solution with the analytes flows through the nozzle and forms a Taylor cone due to the high voltage. The following Coulomb fission and solvent evaporation leads to droplets with a diameter that reaches 200nm or less. The charged analyte is eventually released in the gas-phase following two possible mechanisms (IEM or CRM). Image taken from ref.53

Once the solution with the sample is ready, it is injected into the spraying nozzle with the aid of a syringe pump that keeps the flow rate constant (Fig.2.1). A potential of around 3-4 kV is applied between the nozzle and the sampling cone, allowing the formation of small, highly charged droplets that at the end of the plume reach a diameter of 2 μ m.⁵⁴ If the voltage is high enough (but below the corona discharge threshold), the electric field exerts a similar magnitude of force in the droplet as the surface tension does, and a cone shape begins to form (Taylor cone) emitting a jet of liquid (cone-jet) that is essential to the formation of the small droplets (Fig.2.2).^{55,56}

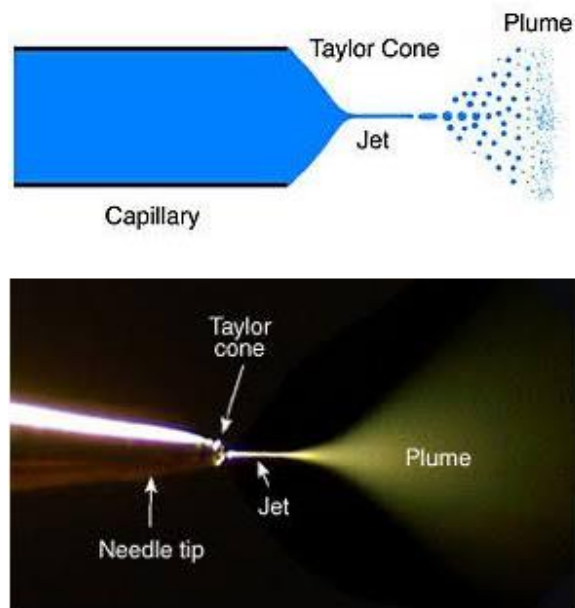


Figure 2.2 Schematic of an ESI source. Adapted from ref. 57

Once the droplet is sprayed into the desolvation zone towards the sampling cone, it will shrink because of solvent evaporation. An inert gas (usually nitrogen) is pumped into the interface housing to raise the temperature of the air within the ionization chamber to aid complete desolvation. The temperature required is dependent on the solvent properties of the sprayed droplet and the eluent flow rate.^{51,53}

As the droplet shrinks due to solvent evaporation, its radius decreases, but its charge remains constant. This leads to an increase in repulsion between the surface charges until the electrostatic repulsive forces become equal to the eluent surface tension (Rayleigh Instability Limit). Further decreasing the radius of the droplet will cause the Rayleigh limit to be exceeded, and the droplet will undergo a coulombic fission to reduce the coulombic stress between the surface charges. The process is often referred to as ‘coulombic’ or ‘droplet jet fission’.^{53,58}

The charged analyte is then released from the droplets before entering the sample cone with two possible mechanisms (Fig.2.3) named charge residue model and evaporation model.⁵¹

Dole et al. proposed the charged residue model, where further droplet fissions are hypothesized until very small droplets containing a single ion each are produced. Solvent

evaporation from these droplets will lead to the formation of gas-phase ions.⁵⁹ The evaporation model, on the other hand, was proposed by Iribarne and Thompson, and their theory suggests that below a droplet radius of 10 nm an ion can ‘evaporate’ from within the droplet.⁶⁰ Low molecular weight analytes are thought to follow the ion evaporation model (IEM), whereas the charged residue model (CRM) applies to large globular species.⁵¹ An additional third mechanism named chain ejection model (CEM) has recently been proposed for disordered polymers.⁵¹

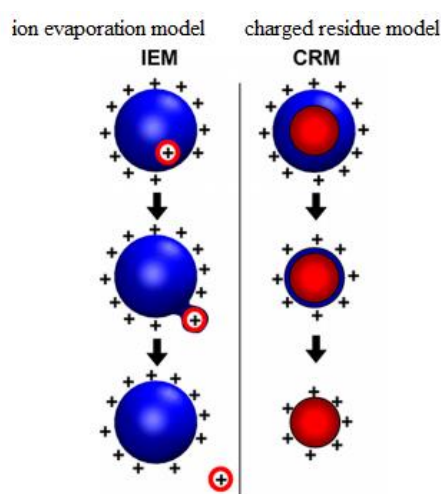


Fig.2.3 Schematic of the ion evaporation model (IEM) and charged residue model (CRM). In the IEM a charged analyte leaves the droplet (“evaporates”) while in the CRM the solvent evaporates completely. Ref.51

2.4 Matrix Assisted Laser Desorption (MALDI) and LDI

The matrix-assisted laser desorption (MALDI) like the ESI is a soft ionization technique that uses laser energy to generate ions.⁶¹ The first step in the MALDI technique is the mixing of the sample with a suitable matrix material and its application on the metal plate. The matrix is a solution of molecules with strong optical absorption in the UV range of the laser, and they are often acidic, therefore, act as a proton source to encourage ionization of the analyte.⁶²

In the second step, a pulsed laser irradiates the sample, and this causes ablation and

desorption of the sample and matrix material, and a hot plume is formed. Eventually, the analyte molecules are ionized in the hot plume of ablated gases (e.g., deprotonation or protonation) and then accelerated into the mass spectrometer (Fig.2.4).⁶³

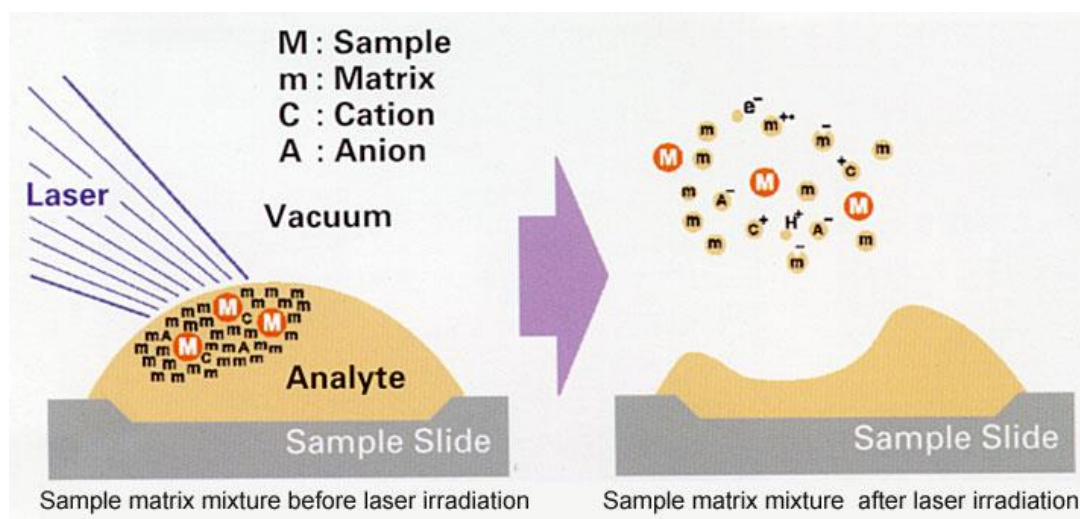


Fig.2.4 MALDI scheme. The Analyte and the matrix are irradiated by a laser pulse. A hot plume is formed, and the analyte is ionised. Image taken from Reference 64.

Interestingly, the MALDI experiments presented in this thesis didn't require the matrix because all the porphyrins used strongly absorb in the UV region. MALDI technique without matrix is defined as LDI.

2.5 Collision Induced Dissociation (CID) and Higher Energy Collisional Dissociation (HCD)

CID and HCD are techniques used to dissociate the gas-phase analyte using collisions with inert gases, therefore, probing structure and bond energies in molecular ions.^{65, 37} CID is a more general term used to indicate collisional dissociation techniques with different mechanisms depending on the type of mass spectrometer.

In an ion-trap instrument, CID is a resonant excitation technique that occurs inside the ion trap. To reach a certain collision energy, ions are accelerated relatively slowly from their starting energy to the final energy, which can be controlled by the user. During the excitation process, the precursor ions collide many times with the inert gas, and each collision can activate or cool it down. The evolution of this equilibrium depends greatly on the ion kinetic energy. If the ions are accelerated slowly compared to the unimolecular dissociation rate, the ions will distribute the excitation energy across most of the bonds, and the weakest bond breaks first. Instead, if the ions are accelerated faster than their unimolecular dissociating rate, then the ions do not have time to equilibrate resulting in a richer fragmentation production where also stronger bonds are broken.⁶⁶

Compared to CID, HCD usually produces richer spectra with a similar fragmentation pattern of typical triple quadrupole spectrum. This technique is performed on Orbitrap mass spectrometers and is a non-resonant activation technique. HCD mode gives access to consecutive dissociation pathways, and ions do not experience a long series of equilibrating collisions with gas molecules; the energy is imparted to them very quickly with fewer collisions with both weak bonds and stronger bonds having a chance to break, depending on which ones are activated.⁶⁶

With both HCD and CID, the CE_{50} (collision energy necessary to obtain 50% overall fragmentation) can be derived from plotting the relative intensity of the parent and fragments ions versus the offset voltage. The relative intensity is calculated by dividing the intensity of the considered molecule by the sum of its intensity and all the fragments and parent ion intensities.

2.6 Laser Interfaced Mass Spectrometer (LIMS)

All the action spectra presented here are obtained with the commercial Bruker AmaZon quadrupole ion-trap mass spectrometer custom modified to allow a laser beam to enter the ion trap as described in detail elsewhere.^{67,68} A schematic of the instrument is shown in Fig.2.5

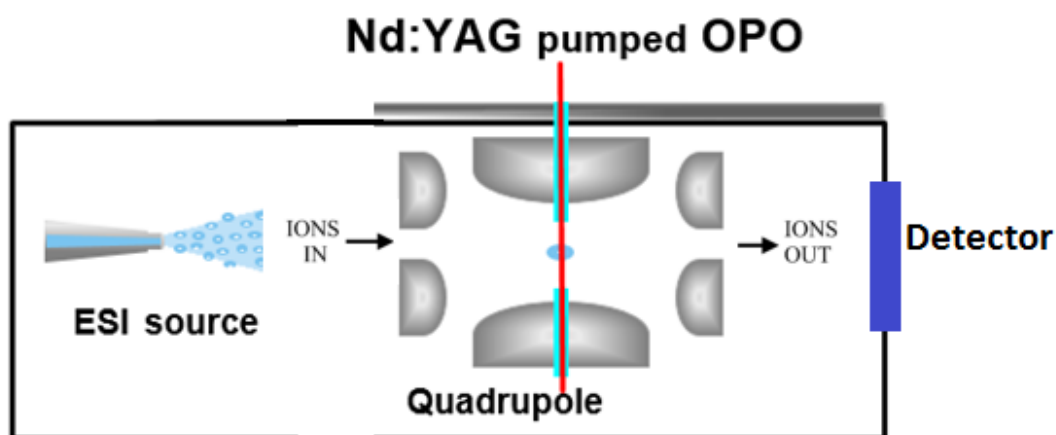


Fig.2.5 Schematic of the AmaZon Bruker laser interfaced mass spectrometer. The ESI source is used to generate the gas-phase ions. The ions of interest are selected according to their m/z , isolated and injected into the quadrupole ion trap. The ion trap is modified so that the laser beam coming from an Nd-YAG pumped laser is directed into it and therefore can be absorbed by the trapped ions.

The photons are produced by an Nd:YAG (Surelite) pumped OPO (Horizon) laser giving around 1 mJ of pulse energy across the range 215-345 nm. The laser pulse-width is $t = 4-6$ ns, the laser pulse frequency is $f = 10$ Hz. The accumulation time chosen was 100 ms so that each ion cloud interacts with only one laser pulse. The laser beam is focused into the ion trap, as shown in Fig.2.6.

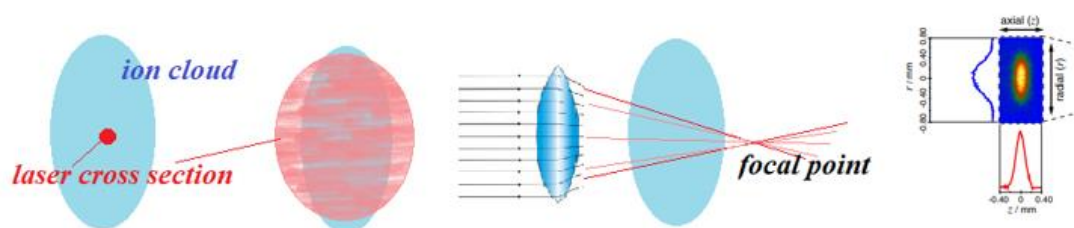


Fig.2.6 Ion cloud interaction with the focused laser beam in the ion trap. The size of the cross section is not known and therefore can range from a small portion to the whole ion cloud. On the right a fluorescence imaging of an ion cloud (approximate dimensions 0.80mm X 1.6mm) taken from Ref.69

As mentioned previously, the numbers of ions trapped are not high enough to directly measure the absorption spectrum and so an indirect method is used. Firstly, with the laser turned off, the intensity of the isolated parent ion mass spectrum peak is measured, and then the intensity of the same ion is measured with the laser turned on. When the photons are absorbed by the parent ion, the intensity of its mass spectrum signal will be lower because of its photodissociation. It is possible to observe also the fragments produced if they have the same electrostatic polarity as the parent ion (Fig.2.7). This procedure is repeated with different wavelengths to obtain a full action spectrum, with measurements usually taken with a wavelength step of 2-4 nm.

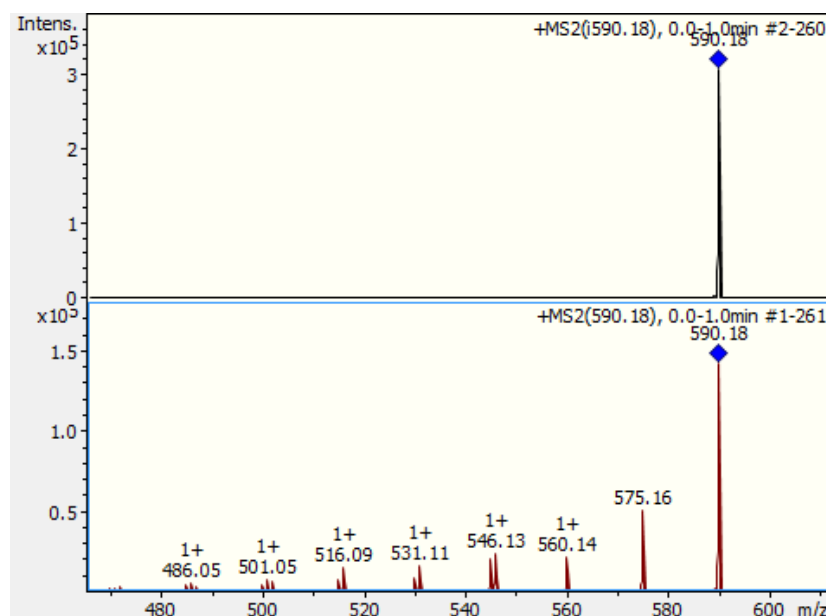


Fig.2.7 Nickel octaethylporphyrin(NiOEP) mass spectra. Above with laser turned off and below with laser on at 366nm. The parent ion intensity (m/z 590.18) is lower with the laser on and many positively charged photofragment products are observed. Note the different y-axis scales to compare intensities.

The laser data are collected and analyzed as follows:

- 1) The gas-phase parent ions (the molecule of interest) are generated using an ESI source and are isolated and trapped in the ion trap.
- 2) A wavelength is chosen, and many mass spectra are collected both with the laser off and on. The averaged mass spectrum with the laser off is compared to the averaged mass spectrum collected with the laser on (Fig.2.7 is an example of both those averaged spectra).
- 3) The procedure is repeated with the next wavelength (usually 2-4 nm step) until all the wavelength range of interest is covered.
- 4) The data collected are analyzed by a home-built Python software developed as part of this thesis work (Appendix A2), and the photodepletion (PD), and photofragmentation (PF) yields are calculated according to equations 2.1 and 2.2 and plotted against wavelength (nm) or wave energy (eV).

The photodepletion (PD) and photofragmentation (PF) yields are calculated according to the following formulas, where I_{off} and I_{on} are the intensities of the parent ion signal (recorded by the mass spectrometer detector) respectively with the laser off and on, λ is the wavelength (nm) and P is the laser pulse energy (mJ). In the PF formula, I_{frag} is the intensity of the fragment ion.^{43,70}

$$\textit{Photodepletion yield} = \frac{\ln\left(\frac{I_{\text{off}}}{I_{\text{on}}}\right)}{\lambda \cdot P} \quad \text{Equation 2.1}$$

$$\textit{Photofragmentation yield} = \frac{\frac{I_{\text{frag}}}{I_{\text{off}}}}{\lambda \cdot P} \quad \text{Equation 2.2}$$

In both equations, the $\lambda \cdot P$ term is used to normalize with respect to the number of photons per laser pulse (N_{ph}). In the presented experiments, the laser pulse energy is

maintained at a constant value at all the wavelengths; however, this means that for a fixed laser pulse energy, laser pulses of longer wavelengths are made of more photons, and therefore the probability of interaction with the ions is higher. The normalization is necessary to account for this fact, and it is related to the number of photons per pulse as shown by equation 2.3 below:

$$\lambda \cdot P = \lambda \cdot \left(h \cdot \frac{c}{\lambda} \cdot N_{Ph} \right) = (h \cdot c) \cdot N_{Ph} \quad \text{Equation 2.3}$$

In equation 2.1 the term “ $\ln \left(\frac{I_{off}}{I_{on}} \right)$ ” can also be substituted by the term “ $\frac{I_{off}-I_{on}}{I_{off}}$ ” giving the same profile of the spectrum. In this latter case the denominator I_{off} is used to account for the variations of the signal during the wavelength scan due to the siring pump instability (device used to press the siring with the sample, providing a constant flow of solution to the ESI source), ESI instability, or unstable compound that loses signal over time. The meaning of those two terms is that they both represent the loss of parent ion signal due to photodepletion (fragmentation processes and/or electron loss) caused by the absorption of the laser photons.

In equation 2.2, the intensity of the fragmented product is normalized with the intensity of the parent ion with the laser off to account for the changes of its intensity during the experimental time frame of the wavelength scan.

2.7 Photolysis apparatus

Solutions of Verteporfyryn in pure Acetonitrile (MeCN) were photolyzed with home-built photolysis cells. The LED lights had their maximum peak emission at 310 nm and 356 nm, respectively, in the two apparatus. A scheme of the apparatus is shown in Fig.2.8.

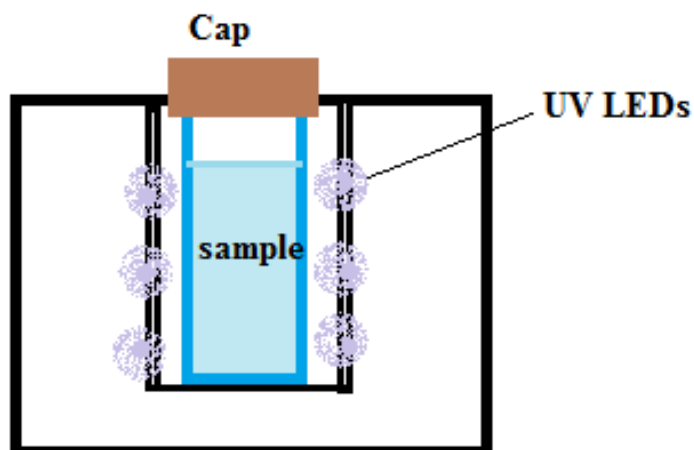


Figure 2.8 Photolysis cell. A solution with the sample is inserted in a hole and a cap is added to block the light from the outside environment. In the hole there are a series of UV LEDs and the sample is kept there for a certain amount of time and then the photolysis products analysed using mass spectrometry.

Because of the absence of LED photolysis cells covering the visible range in our lab, the solution with the sample was also photolyzed with the OPO laser at the chosen wavelength of 689 nm, corresponding to the absorption peak used in PDT.

Chapter 3: ZnTPP complexes with halides

3.1 Introduction

The first part of the project presented in this thesis involves gas-phase experiments of neutral metalloporphyrin (MP) aggregates with halides. The negatively charged halides allow the use of the ESI technique, but also offer the possibility of forming 2:1 aggregates where the halide sits between the porphyrins (Fig.3.1). Similarly to the case of the iodide ion-pyrimidine clusters studied previously in the Dessent group⁷¹ choosing a halide anion-neutral MP complex allows us to study the near-threshold excitation (near vertical electron detachment energy) and to explore the free-electron neutral molecule interaction, thus providing a route for studying the electron capture properties of metalloporphyrins. In this chapter, the computational studies are presented and compared with the experimental results, which include HCD studies, photodepletion (PD), and photofragmentation (PF) spectra.

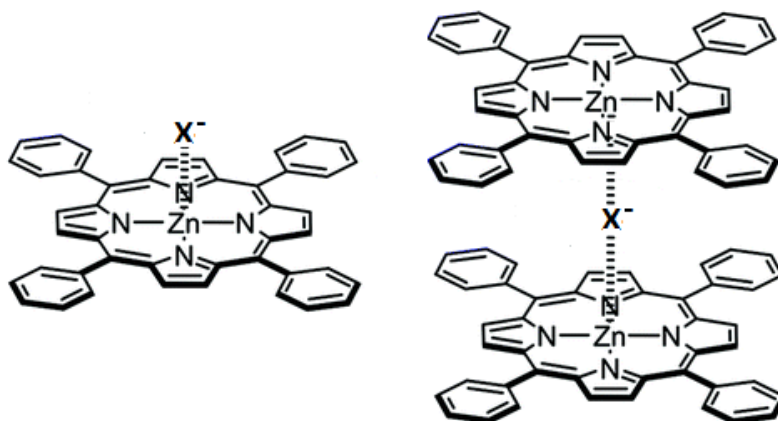


Figure 3.1. 1:1 and 2:1 (bridged) complexes of ZnTPP and halide anions (X^-).

3.2 Experimental methods

Computation:

Gaussian 09⁷² was used for all the calculations and frequency calculations were performed to test that the optimized structures correspond to a true minimum.

First, the effect of different metals on the complexation energy with halide anions was tested on the simplified MP structure in Fig.2.3 optimized in this work: all these computational calculations were performed using the functional UB3LYP⁷³ and the 6-31+g(d)⁷⁴ basis set except with the iodine-containing complexes for which the basis set dgdzvp was chosen according to a DFT comparative analysis done on iodine-containing compounds.⁷⁵ For all the complexation energies determined, counterpoise correction was applied.

The following optimization DFT calculations on $\text{ZnP} \cdot \text{X}^-$ complexes (ZnP is the simplified structure with $\text{M}=\text{Zn}$, Fig.2.3, while ZnTPP is the porphyrin used in the experiments) were performed using the B3LYP hybrid functional. Different basis sets were used on different sets of atoms: the s6-31g⁷⁶ basis set was used for Zn, 6-31+g(d) for C, N, O, H, Br, Cl, F, and dgdzvp for I.⁷⁵ This choice is in line with other computational studies on metalloporphyrins.^{77,78,79,80} These same settings were applied also with the ZnTPP conformational studies, VDEs calculations and with the $(\text{ZnP})_2 \cdot \text{X}^-$ complexes. With these latter 2:1 complexes, the general Grimme's dispersion correction DFT-D3⁸¹ was used to account for the Van der Waals (dispersive) interactions between the two porphyrin rings. For the calculation of the complexation energies, counterpoise correction was always applied and all the charges presented in this chapter were determined with the NBO analysis.⁸²

Experimental:

ZnTPP (HPLC $\geq 94\%$) and the halide containing salts (KBr, NaCl, NH_4F , KI) were all purchased from Sigma Aldrich and used without further purification to prepare 10^{-5} M equimolar (1:1) solutions in MeCN that were electrosprayed and analyzed by mass spectrometry.

All HCD experiments were performed on the Orbitrap Fusion Tribrid mass spectrometer (Thermo Fisher Scientific, Waltham, MA, USA) using the following parameters: ESI

negative ion voltage of 2500 V, capillary temperature of 275°C and 250°C for the 1:1 and 2:1 complexes respectively (however no significant difference was found in the range 90-290°C), flow rate of 4µL/min, isolation mode ion trap, detector type Orbitrap. The HCD voltage was set to increase every minute and all the spectra acquired within the same minute were averaged and their data used to produce the HCD voltage vs. relative intensity plots (i.e. Fig.3.4). The voltage difference between the C-trap, trap lens and the ion-routing multipole (IRM) was 244 V at 100% HCD collision energy.

The PD and PF spectra across the UV and visible range were collected using the laser interfaced AmaZon Bruker ion trap mass spectrometer with a laser pulse energy chosen to achieve a 20-30 % intensity drop of the parent ion signal at its maximum absorption peak to avoid photodissociation caused by absorption of multiple photons; a phenomenon described in the power studies of R.A.Jockusch and H.Yao on fluorescein derived molecules.⁸³ The parameters used with the AmaZon mass spectrometer were: ESI capillary 4400 V, End Plate Offset -600 V, capillary temperature of 120°C and flow rate of 4µL/min. The fragmentation time was set at 100 ms so that each ion packet was excited only by one laser shot. Importantly, all the ZnTPP · X⁻ complexes were isolated with a wide isolation window that included many isotopic peaks to stabilize the isolated ion.

3.3 Effect of the metal on the complexation energies

The first part of the project was to choose a neutral metalloporphyrin (with the metal in the +II oxidation state) and try to make its iodide aggregate in the gas-phase with the ESI technique. Initial mass spectrometric investigations revealed that it was worth studying the metalloporphyrin clusters with all the halides.

To guide the purchase of the metalloporphyrin, a series of theoretical calculations were done as described in section 3.2 using the simple structure in Fig.3.2 (this basic metalloporphyrin structure will be represented in this chapter with the symbol MP).

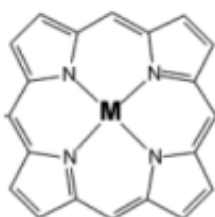


Figure 3.2 Porphyrin structure used for the computational evaluation of the complexation energies of metalloporphyrins with halides. ($M = \text{Zn, Mg, Cu, Ni, Fe}$).

Complexation energies of both the $MP \cdot Cl^-$ and $MP \cdot I^-$ aggregates are shown in Tables 3.1 and 3.2 respectively.

Table 3.1 Complexation energies of the $MP \cdot Cl^-$ clusters, using the simplified MP structure in Fig.3.2, with $M = Mg, Zn, Cu(II), Ni(II), Fe(II)$.

MP (metalloporphyrin)	Complexation energy (kcal/mol)
Mg-MP	-44.33
Zn-MP	-38.32
Cu-MP	-11.93
Ni-MP	+0.95
Fe-MP	-36.68

Table 3.2 Complexation energies of the $MP \cdot I^-$ cluster, using the simplified MP structure in Fig.3.2, with $M = Mg, Zn, Cu(II), Ni(II), Fe(II)$.

MP (metalloporphyrin)	Complexation energy (kcal/mol)
Mg-MP	-29.47
Zn-MP	-26.65
Cu-MP	-5.06
Ni-MP	+3.67
Fe-MP	-25.90

In all the complexes studied the halide anion binds directly with the metal at the center of the MP, which shows a partial positive charge in the uncomplexed MPs.

For both the $MP \cdot Cl^-$ and $MP \cdot I^-$ clusters, the order in the stabilization energy is $MgP < ZnP < FeP < CuP < NiP$. According to this data, the MgP has the most negative complexation energy, and therefore seems the most suitable for the formation of clusters with these two halide anions; NiP appears to be the worst choice with positive stabilization energy that suggests it is not possible to form $NiP \cdot Cl^-$ or $NiP \cdot I^-$ clusters.

This was confirmed by the experimental ESI/MS data with the NiOEP for which none of its aggregates with any of the halide anions (F⁻, Cl⁻, Br⁻, I⁻) was observed. Furthermore, for all the MPs the stabilization energy of the MP · Cl⁻ is more negative than the MP · I⁻, indicating a higher preference for ‘hard’ ligands.

Even though the magnesium porphyrin (MgP) was predicted to bind most strongly with halide anions, for the experiments, we chose the zinc *meso*-tetraphenylporphyrin (ZnTPP) because it is considerably less expensive; ZnP was predicted to be the second-best choice among the metals studied to form complexes in the gas phase with chloride and iodide, and adding four additional phenyl groups in the *meso* position was predicted to have a negligible influence on the partial charge on the Zn (+1.292 in ZnTPP vs. +1.293 in ZnP), therefore its binding affinity with the halide was predicted to not be compromised.

3.4 Theoretical complexation energies of ZnP with halides and comparison with HCD

Optimization DFT calculations were performed on ZnP · X⁻ complexes with X = I, Br, Cl, F, and the complexation energies were determined following the methods described in section 3.2. The results are summarised in Table 3.3. and shows that these complexes have relatively high bonding energies (around 30 to 70% of a C-C single bond).

Table 3.3 Theoretical complexation energies of ZnP · X⁻ complexes.

Cluster	Complexation energy (kcal/mol)
ZnP · I ⁻	-25.47
ZnP · Br ⁻	-31.99
ZnP · Cl ⁻	-38.11
ZnP · F ⁻	-61.11

The calculated gas-phase complexation energy order follows the condensed phase equilibrium constant trend determined in a study by Nappa and Valentine⁸⁴ on the ZnTPP complexes with halides (Table 3.4). The same trend is found with zinc porphyrins anchored to nanocrystalline TiO₂ by Meyer *et.al* (Table 3.5, Fig.3.3).⁸⁵ In this latter case, there is no evidence of ZnTPP · I⁻ indicating the K_{eq} is too small for the complex to be detected or that in this case the complex is not possible to form.

Table 3.4 Equilibrium constants for the ZnTPP · X⁻ complexes, where X⁻ is the ligand.⁸⁴

Ligand	Solvent	K _{eq} M ⁻¹
F ⁻	CH ₂ Cl ₂	>10,000
Cl ⁻	CH ₂ Cl ₂	290 ± 30
Br ⁻	CH ₂ Cl ₂	17 ± 2
I ⁻	CH ₂ Cl ₂	No evidence of complex formation

Table 3.5 Equilibrium constants for the Zinc Porphyrin Sensitizers both in a fluid propylene carbonate solution and anchored to Nanocrystalline TiO₂.⁸⁵

		K _{eq} M ⁻¹
ZnP-Cl	Solution	1670 ± 30
	TiO ₂	780 ± 40
ZnP-Br	Solution	96 ± 4
	TiO ₂	70 ± 4
ZnP-I	Solution	5.5 ± 0.7
	TiO ₂	3.4 ± 0.1

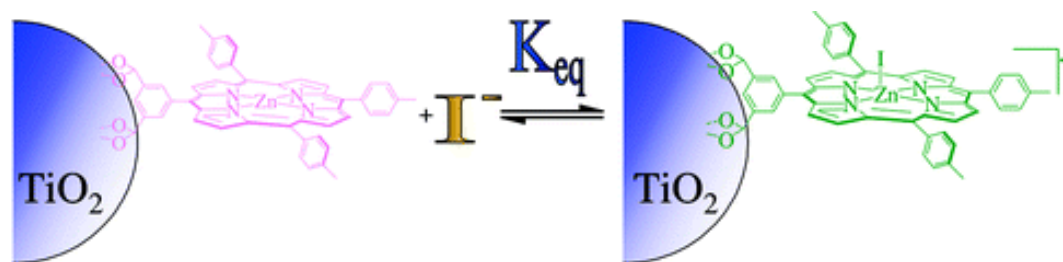


Figure 3.3 Zinc Porphyrin Sensitizers anchored to mesoporous nanocrystalline (anatase) TiO₂ thin films (TiO₂/ZnP). Image taken from Reference 85.

This trend in the complexation energies is also confirmed with CID and HCD (Higher energy Collisional Dissociation) experiments presented below. The Zn-halide bond strength increases with the increasing of the σ -donor character of the ligand ($F^- > Cl^- > Br^- > I^-$). From the mass spectrometric studies, it was determined that the ZnTPP forms 1:1 and 2:1 complexes with all the halides considered (F, Cl, Br, I). These data are shown in Appendix A1.2.

All the ZnTPP $\cdot X^-$ complexes were studied with the HCD, allowing a comparison of the complexation energies and revealing the fragmentation pathways.

Fig.3.4 displays the results for the 2:1 complexes and Fig.3.5 for the 1:1 dimers complexes. As shown in Table 3.6 these complexes can be easily fragmented except for the fluorine 2:1 complex that shows a collision voltage above 102. The dimer fluorine cluster, ZnTPP $\cdot F^-$, is difficult to discuss since F^- has a mass below the m/z 50 threshold; it is reasonable to predict that its CE_{50} falls above 11.3% that corresponds to the CE_{50} of (ZnTPP)₂ $\cdot F^-$; this is supported by the fact all the other dimers have a higher CE_{50} than the respective 2:1 complexes. The result is also in line with Nappa and Valentine's research in which only the dimer ZnTPP $\cdot F^-$ was observed.⁸⁴

For all these complexes, the fragmentation pathways were also studied. The fragmentation mechanism of the $(\text{ZnTPP})_2 \cdot \text{X}^-$, with $\text{X} = \text{I}, \text{Cl}, \text{Br}, \text{F}$, complexes is as follow (with the respective MS spectrum being displayed in appendix A1.3):



Regarding the dimers, only the $\text{ZnTPP} \cdot \text{Br}^-$ and $\text{ZnTPP} \cdot \text{I}^-$ HCD graphs are shown here because the lowest mass threshold of m/z 50 doesn't allow the detection of the fragments chloride and fluoride and no other negatively charged fragments are formed; therefore with the $\text{ZnTPP} \cdot \text{Cl}^-$ and $\text{ZnTPP} \cdot \text{F}^-$ complexes the relative intensity can not be plotted since it is constantly 100%.

The $\text{ZnTPP} \cdot \text{Br}^-$ and $\text{ZnTPP} \cdot \text{I}^-$ complexes fragment according to the pathway:



It seems possible that $\text{ZnTPP} \cdot \text{Cl}^-$ also follows this same simple mechanism since on increasing the HCD voltage, the precursor ion signal drops to zero and no ionic fragment is observed across the entire HCD voltage range.

The fluorine 1:1 cluster follows more distinctive fragmentation pathways (Appendix A1.4); interestingly its negative fragmentation products are possible to see only using the HCD technique. Using the CID technique, the behavior was like the $\text{ZnTPP} \cdot \text{Cl}^-$ complex, and it was not possible to see any fragmentation product even though the precursor ion signal decreases increasing the collision voltage. This can be explained considering that the CID is more an "equilibrating" collision dissociation technique so that only the Zn-F bond is broken.

Table 3.6 CE_{50} of for the bridged 2:1 and dimer 1:1 complexes in the gas-phase determined using the HCD technique.

Parent cluster	^a CE_{50} %	^b E_{50} (Voltage)
$(ZnTPP)_2 \cdot I^-$	0.50%	1.22 V
$(ZnTPP)_2 \cdot Br^-$	2.24%	5.47 V
$(ZnTPP)_2 \cdot Cl^-$	3.00%	7.32 V
$(ZnTPP)_2 \cdot F^-$	11.33%	27.6 V
$ZnTPP \cdot I^-$	2.49%	6.07 V
$ZnTPP \cdot Br^-$	2.60%	6.34 V

^a $CE_{50\%}$ is the collision energy necessary to obtain 50% overall fragmentation, expressed as a percentage with respect to the highest offset available on the Orbitrap Fusion Tribrid mass spectrometer.

^b E_{50} is the collision voltage necessary to obtain 50% overall fragmentation.

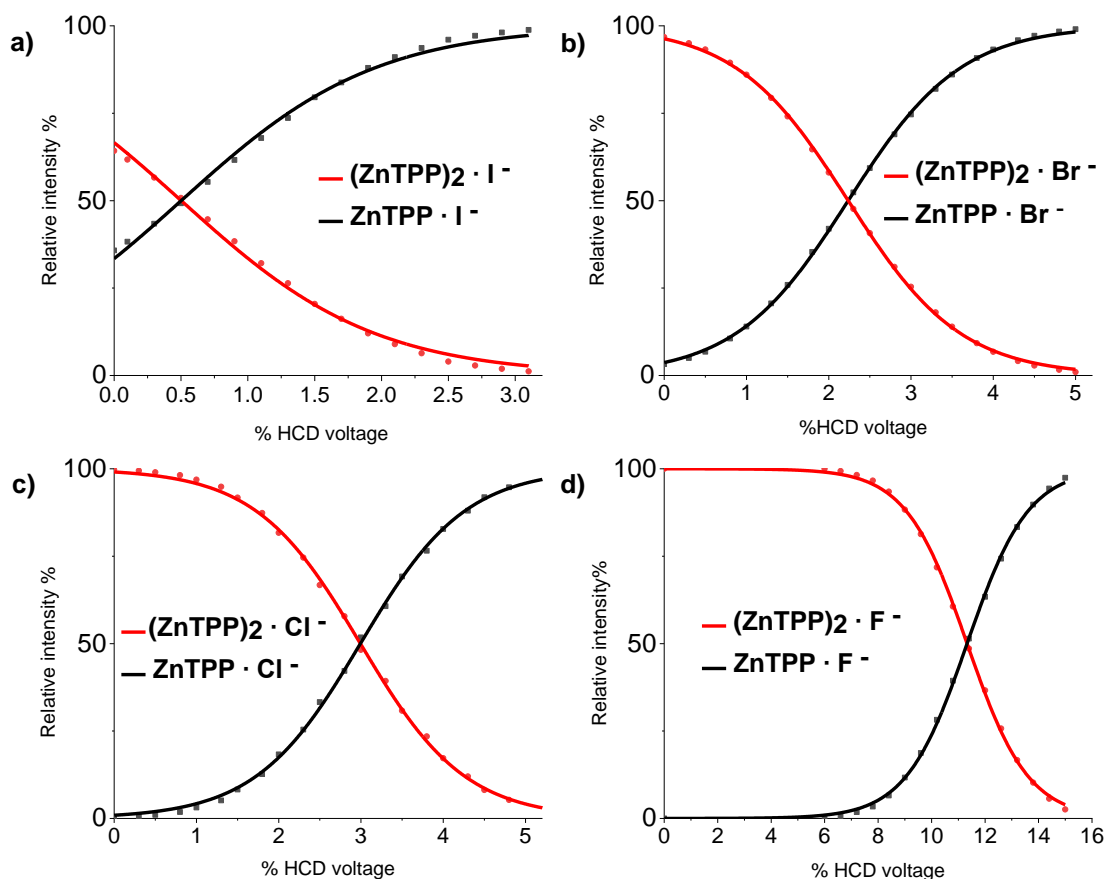


Figure 3.4 HCD plots of the 2:1 complexes: (a) $(ZnTPP)_2 \cdot I^-$, (b) $(ZnTPP)_2 \cdot Br^-$, (c) $(ZnTPP)_2 \cdot Cl^-$, (d) $(ZnTPP)_2 \cdot F^-$. The relative intensity of the signals of the parent ions and fragments are plotted against the percentage of collision voltage relative to the highest offset available on the Orbitrap Fusion Tribrid mass spectrometer. Note that the x-axes are set with different scales.

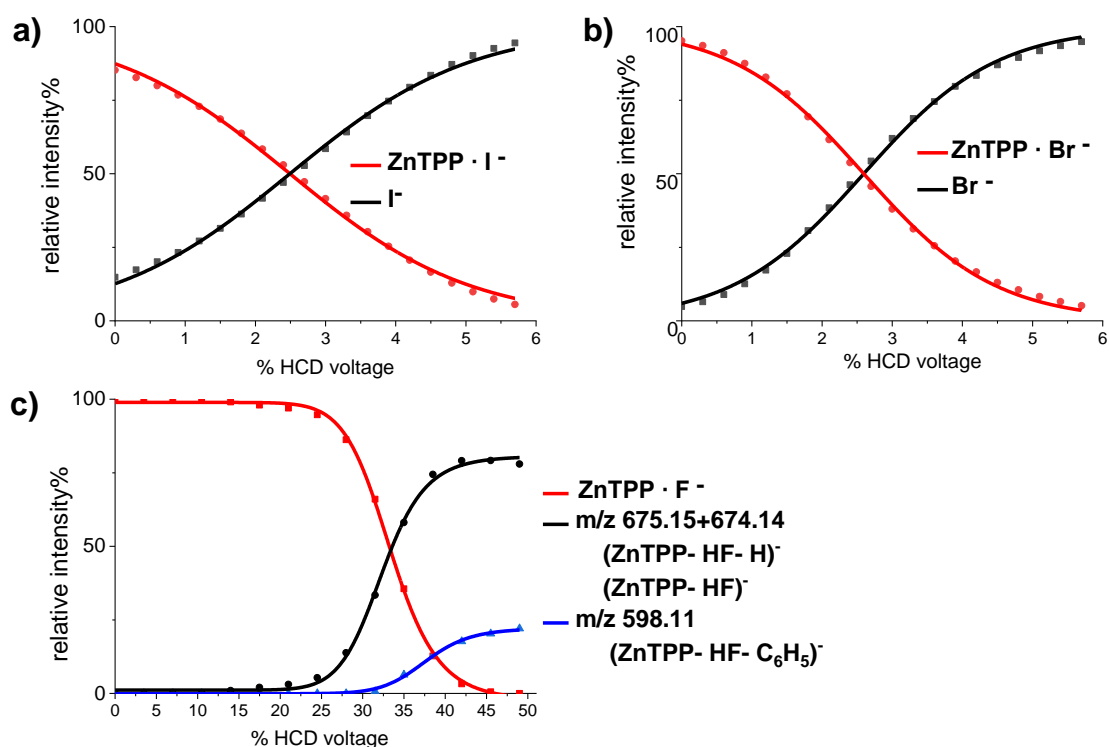


Figure 3.5 HCD plots of the dimers: (a) $\text{ZnTPP} \cdot \text{I}^-$, (b) $\text{ZnTPP} \cdot \text{Br}^-$, (c) $\text{ZnTPP} \cdot \text{Cl}^-$

3.5 Optimised structures of Zn porphyrins and halide complexes

Computationally, the simplified $\text{ZnP} \cdot \text{X}^-$ structures were studied instead of $\text{ZnTPP} \cdot \text{X}^-$ because the latter are computationally too demanding.

From the optimized structure (e.g., in Fig.3.6 and all the structures in Appendix A1.5) and Table 3.7, it can be noticed that the bond with the halides pulls the zinc out of the plane of the porphyrin ring, and this distortion does not change significantly across different halides. As shown in Table 3.8, the major difference observed with different halides is the amount of charge transferred from the halide to the metal centre and to the remaining organic part of the porphyrin ring.

The optimized sandwich ZnP complexes (2:1) with all the halides (Fig.3.7 and Appendix A1.5) reveal a sloped structure, which appears to arise due to the stabilization from the marginal π - π stacking interaction; the calculated stabilization energy derived from the interaction of two ZnP molecules is 25 kcal/mol, and its value is high enough to contribute significantly to the overall optimized structure. These 2:1 structures were optimized using the split basis sets with a dispersion correction to account for the Van der Waals interactions between the two porphyrin rings as described in Section 3.2. The structural data of these optimized structures are shown in Table 3.9. The energy required to break the bond between the halide and one of the ZnP molecule was determined, and it is shown to be lower than the 1:1 complexes in accordance with the HCD experimental results, in which the 2:1 complexes dissociate at lower voltages compared to their respective 1:1 complex (Table 3.10).

Finally, the ZnTPP molecule was optimized to determine the ground state conformation of the phenyl groups (Fig.3.8). All the phenyl groups are slightly bent with a dihedral angle of 109.2° to minimize the steric interactions (Fig.3.9), however, two opposite phenyls can be in a “parallel” or “cross” position (Fig.3.8.b). These positions were determined not to influence the stability of the molecule, therefore all these conformers appear to be equally stable.

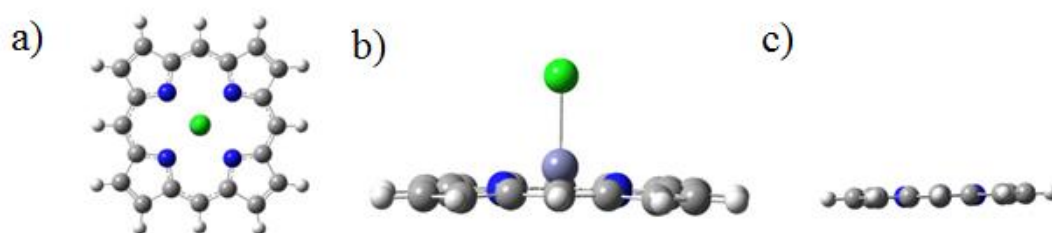


Figure 3.6 DFT optimised structures: a) top and b) side view of ZnP·Cl complex. c) Side view of the only ZnP. The zinc atom is pulled out of the porphyrin ring due to the bond with chloride.

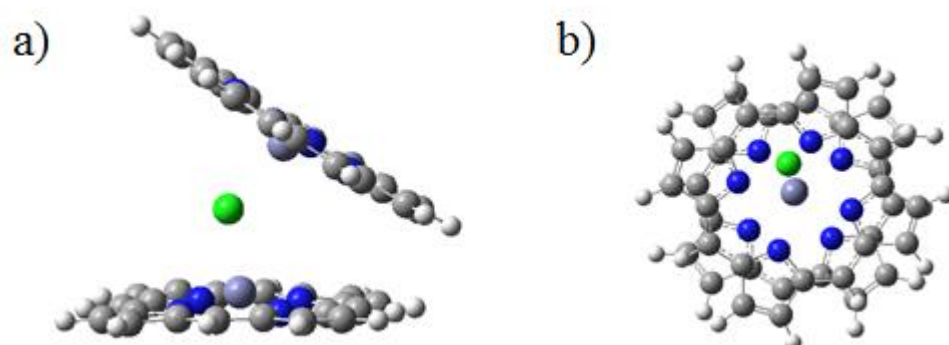


Figure 3.7 DFT optimised structure of the $(ZnP)_2 \cdot Cl^-$ complex. a) Side view, b) top view.

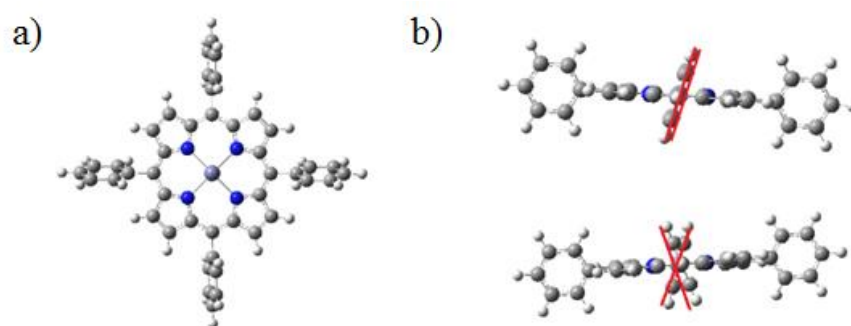


Figure 3.8 DFT optimization with different position of the phenyls groups in ZnTPP. a) front view of the conformer with all the opposite phenyls parallels (//). b) lateral view of the “parallel” and “cross” position of the phenyls. All the conformers are equally stable.

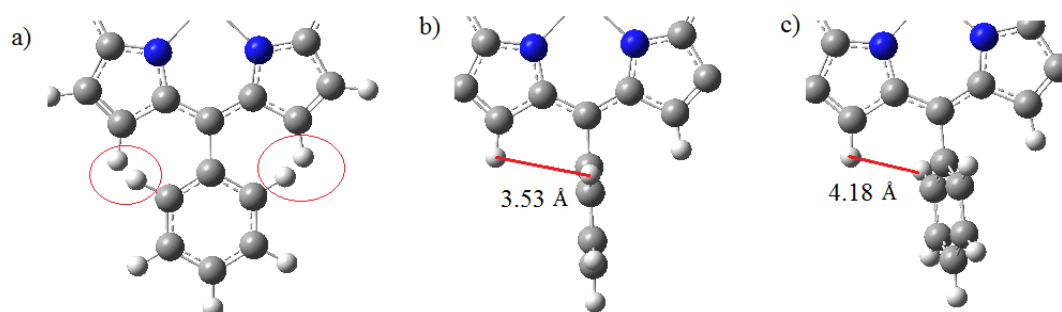


Figure 3.9 The phenyl group in the slightly bent conformation minimise the sterical interactions(c). a) Dihedral angle 0° , b) dihedral angle 90° and c) minimal energy structure with dihedral angle of 109.2° where the hydrogens shown are at the maximum distance from each other.

Table 3.7. Partial charges on Zinc, halides, and nitrogens for the 1:1 ZnP · X⁻ complexes. In addition, the zinc-halide and zinc-nitrogen bond length are reported. The last column reports the bond angle between the halide, zinc, and nitrogen, which reflects the displacement of the zinc from the porphyrin ring plan.

Complex	Charge on Zn	Charge on the halide	Charge on nitrogens	Zn-halide bond length(A)	Zn-N bond length(A)	N-Zn-halide bond angle(°)
ZnP · I ⁻	1.057	-0.632	-0.653	2.79	2.13	104.78
ZnP · Cl ⁻	1.107	-0.678	-0.606	2.52	2.14	105.17
ZnP · Br ⁻	1.143	-0.709	-0.599	2.35	2.14	105.66
ZnP · F ⁻	1.308	-0.825	-0.594	1.9	2.15	105.97
ZnP only	1.293	X	-0.653	X	2.06	X

Table 3.8. The amount of charge lost from the halide anion and transferred to the zinc atom and the organic part of the porphyrin. The negative sign indicates a decrease in electron density while the positive sign an increasing electron density.

Complex	Charge change on halide	Charge change on zinc	Charge change on the organic part
ZnP · I ⁻	-0.370	+0.236	+0.134
ZnP · Cl ⁻	-0.322	+0.186	+0.136
ZnP · Br ⁻	-0.291	+0.150	+0.143
ZnP · F ⁻	-0.175	-0.015	+0.190

Table 3.9. Theoretical structural data of the $(\text{ZnP})_2 \cdot \text{X}^-$ complexes, including halide-Zn bond length and Zn-halide-Zn bond angle. The last row shows the distance between two ZnP molecules planes in a $(\text{ZnP})_2$ dimer.

Cluster	Zn-halide bond length (Å)	Zn-halide-Zn angle (°)
$(\text{ZnP})_2 \cdot \text{I}^-$	2.84	124.0
$(\text{ZnP})_2 \cdot \text{Br}^-$	2.59	127.9
$(\text{ZnP})_2 \cdot \text{Cl}^-$	2.43	131.6
$(\text{ZnP})_2 \cdot \text{F}^-$	1.97	148.7
$(\text{ZnP})_2$ dimer only	Interplanar distance = 3.16 Å	

Table 3.10. Theoretical complexation energies of 2:1 ZnP complexes with halides corresponding to the reaction: $(\text{ZnP})_2 \cdot \text{X}^- \rightarrow \text{ZnP} \cdot \text{X}^- + \text{ZnP}$. The last row shows the stabilisation energy between two ZnP molecules.

Cluster	Complexation energy (Kcal/mol)
$(\text{ZnP})_2 \cdot \text{I}^-$	-21.95
$(\text{ZnP})_2 \cdot \text{Br}^-$	-23.94
$(\text{ZnP})_2 \cdot \text{Cl}^-$	-28.44
$(\text{ZnP})_2 \cdot \text{F}^-$	-32.73
$(\text{ZnP})_2$ dimer only	-24.97

3.6 Photodepletion, photofragmentation and VDEs

In the experiments presented in this chapter, a negatively charged complex ($\text{ZnTPP} \cdot \text{X}^-$) is predicted to lose an electron in the presence of photons of adequate energy (*photodetachment*) and therefore become neutral. The geometry of an ion may be different from the corresponding neutral molecule. If the neutral is in the same geometry

as the anion, then a vertical ionization energy (or vertical detachment energy, VDE) can be measured. In contrast, in the case of the adiabatic ionization energy, the neutral is in its lowest energy, relaxed geometry. This is illustrated in fig.3.10.

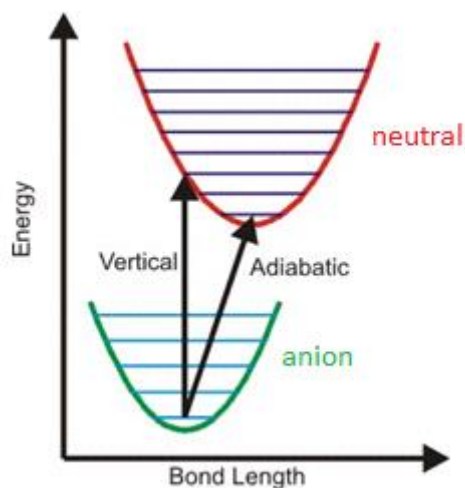


Figure 3.10 Schematic to illustrate the difference between a vertical and adiabatic ionization energy in case of an anion.

The VDEs of the ZnP complexes with halides were calculated theoretically, and the results summarized in table 3.11. To calculate the VDEs, the energy of the gas phase ionized neutral molecule is subtracted to the energy of negatively charged complex fixing its optimized geometry (single point calculation). The VDE was also calculated for the ZnP molecule, and as predicted, the bond with the halide strongly lowers its value compared to the uncomplexed ZnP, making it accessible to the UV laser range. The VDE was also calculated for the halide anion alone, and its value compared with the electron affinity of the halide neutral atom. The calculated VDE of the halide anions was found to be in good agreement with the tabulated EA.⁸⁶

Table 3.11 VDE of the $ZnP \cdot X^-$ complexes compared to the VDE of the respective halide anion. The last row shows the uncomplexed ZnP molecule VDE. The third column represents the electron affinity of the halide neutral atoms (taken from Ref.83 and found to be equal to the computational calculated VDE).

Complex	VDE (eV)	EA halides (eV)
$ZnP \cdot I^-$	3.3	3.1
$ZnP \cdot Br^-$	3.2	3.4
$ZnP \cdot Cl^-$	3.3	3.6
$ZnP \cdot F^-$	3.2	3.3
ZnP	6.8	

After determining that the VDEs of all the $ZnP \cdot X^-$ complexes were within the UV range accessible to the OPO laser, the PD and PF spectra were measured. The solutions used were all 1:1 of $10^{-5}M$ ZnTPP and the respective halide salt in pure acetonitrile.

The experiments were difficult to perform due to the fragmentation of the complexes during the isolation process in the instrument. Isolation was found to cause one order of magnitude drop in the precursor ion signal, suggesting that these complexes are “fragile” species.⁸⁷ Therefore, all the isotopic peaks of a given complex were isolated to increase the isolation width and therefore stabilize the species and minimize the drop in the signal. Even with this wide isolation window, the experiments were challenging due to the low precursor ion signal. The $ZnTPP \cdot I^-$ was found to be the complex with the weakest bond between the MP and iodide, and experimentally it was also observed to be the most unstable. The signal recorded after a wide isolation window was still too low to obtain reliable data, and therefore is not presented here.

From the data collected all of the complexes follow the same two photofragmentation mechanisms; in the first mechanism, one electron is transferred from the halide to the porphyrin leading to a radical $ZnTPP\bullet$ with loss of a neutral halide atom (Equation 3.3), while in the second mechanism, the neutral $ZnTPP$ and halide anion are released as observed in the HCD experiments (Equation 3.4).

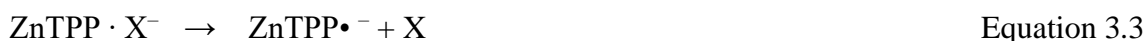


Fig.3.11 shows the solution phase UV-Vis spectrum of ZnTPP in acetonitrile where both the Soret and the Q-bands are visible. The gas phase spectra of the $\text{ZnTPP} \cdot \text{X}^-$ complexes have broader peaks, and they are shifted by up to 120 nm compared to their solution phase spectrum.⁸⁴ Importantly, the Q-bands appear to be missing in PD and PF spectra; this can be attributed to a lifetime of the excited species that is longer than the experimental window or the photofragmentation and photodetachment processes require more laser power to be seen (absorption of multiple photons⁸³).⁸⁸ The fragmentation time in our experiment is 100 ms, probably well above the lifetime of excited species: for example the isolated ferric heme in the gas-phase was found to have lifetime decays in the order of few ms to less than 1 ms⁸⁹, therefore the first explanation is less likely to account for the lack of observed Q-bands.

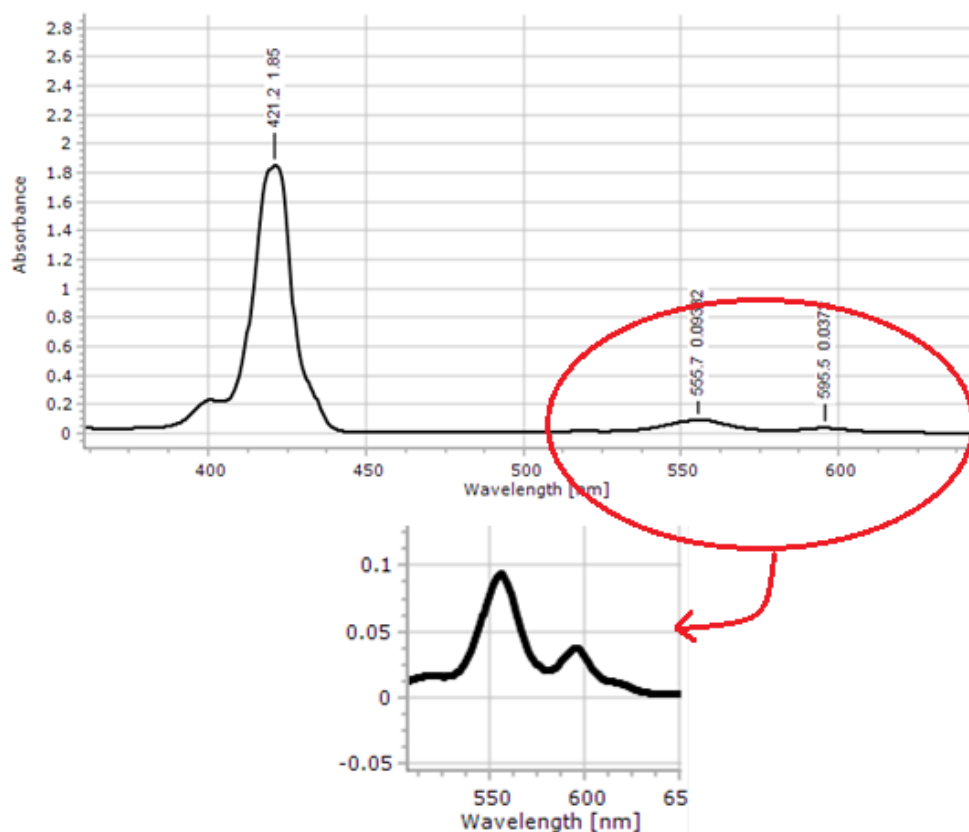


Figure 3.11 UV-Vis spectra of a solution of ZnTPP in acetonitrile. Above spectra in the range 380-620 nm and below Q-bands zoomed in.

3.7 A study on the effect of trapping parameters on the PD yield

Quadrupole ion trap operation is concerned with the criteria that govern the stability (and instability) of the trajectory of an ion, that is, the experimental conditions that determine whether an ion is stored within the device or is ejected from the device.⁹⁰

The two dimensionless Mathieu's parameters, a_u and q_u , are used to define the confinement of ions in quadrupole devices and are strongly related to the m/z range chosen in the mass spectrometer.⁹¹ During these experiments with the $ZnTPP \cdot X^-$ complexes, it was observed that the amount of photodepletion depends significantly on the mass cut off chosen. Because of that, a low cut off of 77 m/z and 120 m/z was used only to determine respectively the Br^- and I^- photofragmentation spectra and a higher cut off (500-600 m/z) was used for the remaining photofragments and PD spectra.

The dependence of PD on the m/z cut off value is reported in Fig.3.12, which shows that for the $ZnPP \cdot Br^-$ complex a low 77 m/z cut off leads to a substantially reduced PD yield. A possible explanation of this phenomenon is that with a lower cut off, the ion packet is more diffuse, and so the overlap with the laser beam is reduced.

Effect of the m/z cut off on the PD yield

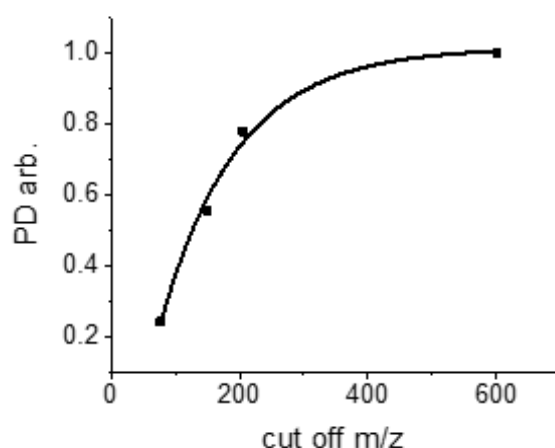


Figure 3.12 PD yield vs. the cut off value (m/z) determined for the $ZnPP \cdot Br^-$ complex at 318 nm .

3.8 ZnTPP · Br⁻ Photodepletion and Photofragmentation spectra

ESI generated ZnTPP · Br⁻ complexes were isolated and the PD and PF spectra obtained. In Fig.3.13 the averaged MS spectra recorded with laser OFF and ON at 318 nm are displayed; these clearly show the reduction of the parent ion intensity and the production of two photofragments, namely Br⁻ and the radical anion ZnTPP^{•-}. These were the only two photofragments observed across the wavelength range used and resulted from the photofragmentation channels shown in Equations 3.5 and 3.6.



Equation 3.5 represents the loss of bromide caused by the bond dissociation between Zn and Br⁻ and corresponds to the same mechanism observed in the HCD study, while Equation 3.6 represents an electron transfer process in which an electron is transferred from Br⁻ to ZnTPP producing the radical anion ZnTPP^{•-}.

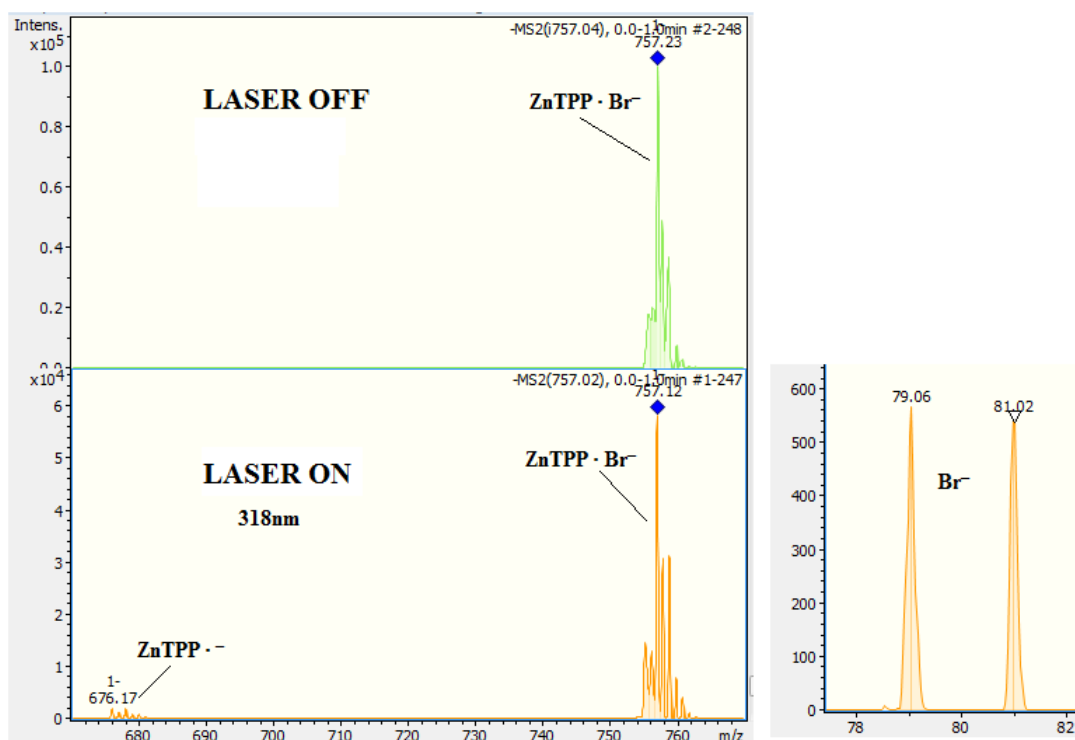


Figure 3.13 Photofragment laser off and laser on mass spectrum of ZnTPP · Br⁻, excited at photodepletion maxima of 318 nm. Note different y-axis scales.

Fig.3.14 shows the PD and PF spectra; the Soret band of the gas-phase $\text{ZnTPP} \cdot \text{Br}^-$ complex is around 320 nm. This is blue-shifted by around 110 nm with respect to the solution absorption spectra in benzene.⁸⁴ In addition, the Soret band width is > 100 nm, well above the typical Soret band widths observed in solution. A new feature at around 430 nm can be observed in both PD and PF spectra; considering the substantial blue-shift of the Soret band, this feature may be attributed to a Q band, however, considering its proximity to the Soret band this may also be a resolved feature of the latter. The onset of the Soret band is at around 400 nm, close to the computational calculated VDE. The PF and PD spectra have similar profiles, indicating that the photofragmentation production is enhanced at the Soret band; this profile similarity is not always observed with other gas-phase molecules, as demonstrated in a previous study by Dessent *et al.*⁹²

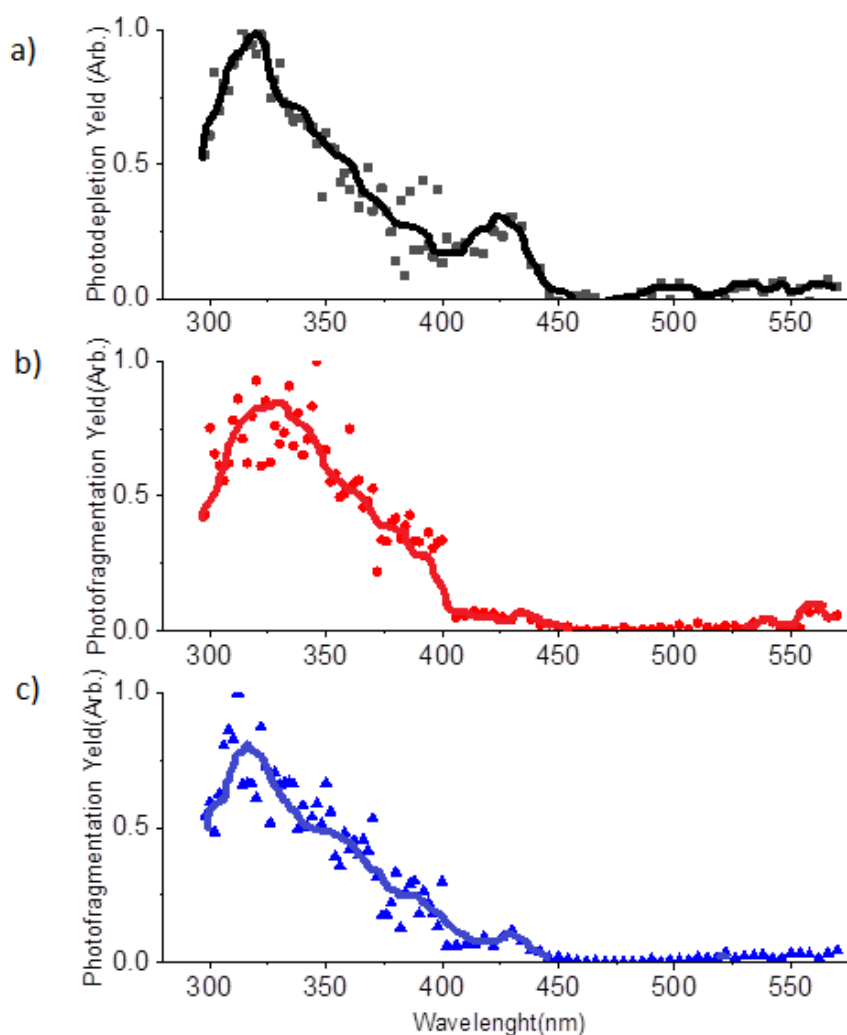
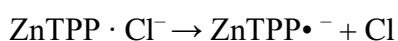


Figure 3.14 a) Gas-phase UV absorption (photodepletion) spectra of $\text{ZnTPP} \cdot \text{Br}^-$ (b and c) Photofragment production spectra of the photofragments, $\text{ZnTPP}^{\bullet-}$ and Br^- respectively. The solid line is a five-point adjacent average of the data points. The laser pulse energy was set at 0.2 mJ in the UV region and 0.6 mJ in the visible (400-600 nm). VDE 3.2 eV corresponding to 387 nm.

3.9 ZnTPP · Cl⁻ Photodepletion and Photofragmentation spectra

ESI generated ZnTPP · Cl⁻ complexes were isolated and the PD and PF spectra obtained. In Fig.3.15 the averaged MS spectra recorded with laser OFF and ON at 310 nm are displayed; these show the production of only the photofragment radical anion ZnTPP^{•-}. Chloride can not be detected because its mass is below the m/z 50 cut-off of the AmaZon mass spectrometer. However, it is very likely that also the loss of the Cl⁻ occurs since this reaction can also be observed in both ZnTPP · Br⁻ and ZnTPP · I⁻ (Fig.3.13 and 3.19). Therefore, because of the low mass of the chloride ion, only the electron transfer reaction can be observed (Equation 3.7):



Equation 3.7

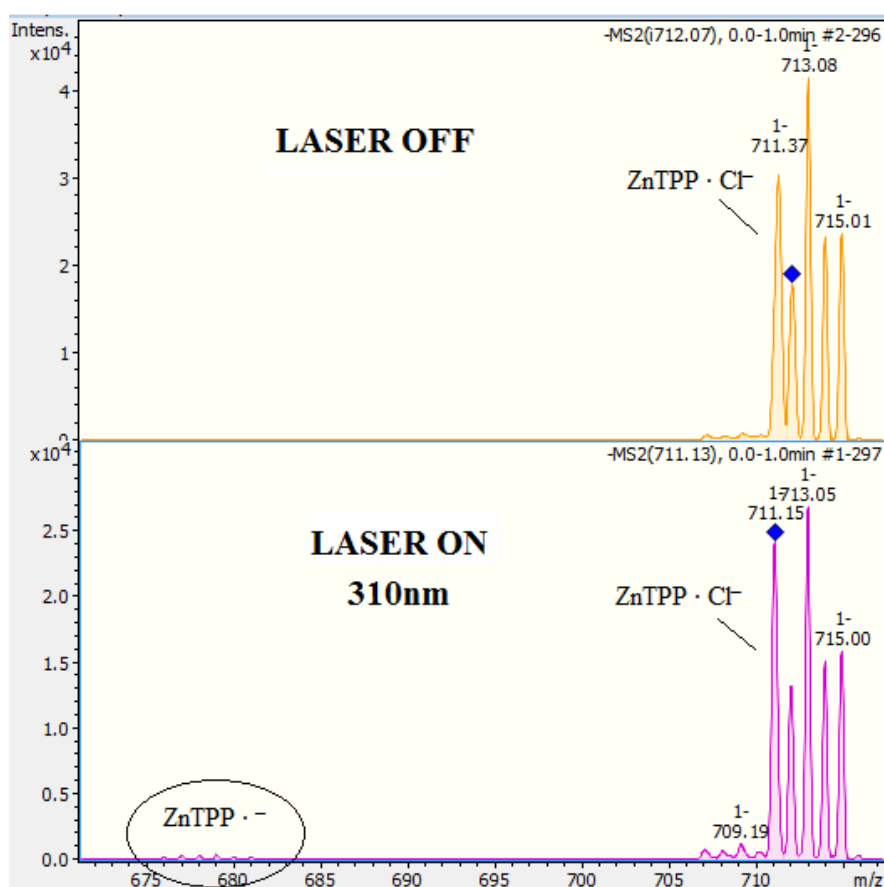


Figure 3.15 Photofragment laser off and laser on mass spectrum of ZnTPP · Cl⁻, excited at photodepletion maxima of 310 nm. Note the different y-axis scales.

Fig.3.16 shows the PD and PF spectra; the Soret band of the gas-phase $\text{ZnTPP} \cdot \text{Cl}^-$ complex is around 310 nm. This is blue-shifted by around 120 nm with respect to the solution absorption spectra in benzene.⁸⁴ The Soret band width is around 65 nm and no additional features can be observed. The onset of the Soret band is at around 350 nm, which is 0.2 eV more than the calculated VDE, however, this can be considered within the computation error typical of the functional B3LYP.⁹³ The PF spectrum is characterized by a poor resolution, however, it shows that the photofragmentation production is clearly increased around the Soret band.

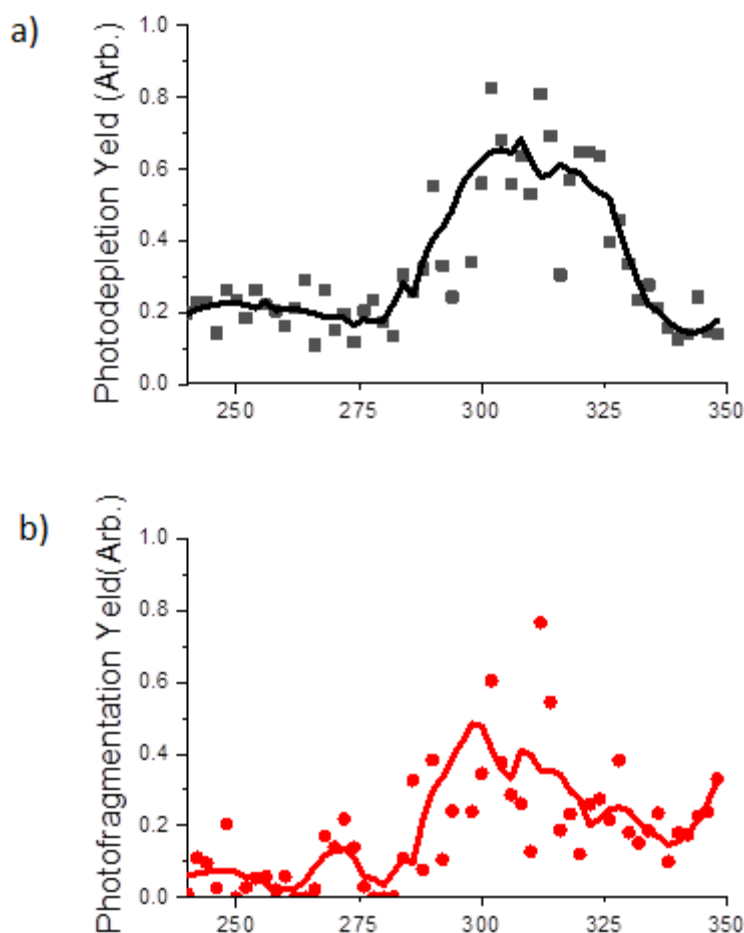


Figure 3.16 a) Gas-phase UV absorption (photodepletion) spectra of $\text{ZnTPP} \cdot \text{Cl}^-$ (b) Photofragment production spectra of the photofragment $\text{ZnTPP}^{\bullet-}$. The solid line is a four-point adjacent average of the data points. The laser pulse energy was set at 0.05 mJ.

3.10 ZnTPP · F⁻ Photodepletion and Photofragmentation spectra

ESI generated ZnTPP · F⁻ complexes were isolated and the PD and PF spectra obtained. In Fig.3.17 the averaged MS spectra recorded with laser OFF and ON at 318 nm are displayed; these clearly show the production of two photofragments derived from an electron transfer process, namely the radical anion ZnTPP•⁻ and its derived species resulted from the loss of a benzene molecule from the porphyrin (ZnTPP - C₆H₆)•⁻. These were the only two photofragments observed across the wavelength range used and resulted from the photofragmentation channels shown in Equations 3.8 and 3.9:



The fluorine anion can not be detected because its mass is below the 50m/z cut-off of the AmaZon mass spectrometer, but as discussed in Section 3.9 it is likely to occur.

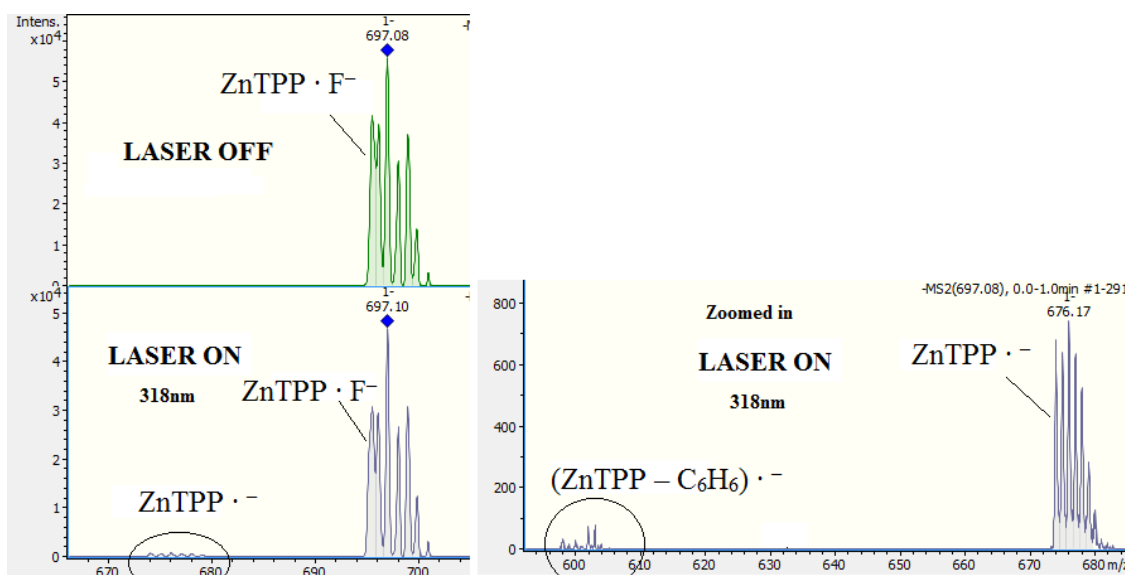


Figure 3.17 Photofragment laser off and laser on mass spectrum of ZnTPP · F⁻, excited near photodepletion maxima at 318 nm.

Fig.3.18 shows the PD and PF spectra; the Soret band of the gas-phase $\text{ZnTPP} \cdot \text{F}^-$ complex is around 316 nm. This is blue-shifted by around 110 nm with respect to the solution absorption spectrum in benzene.⁸⁴ The laser pulse energy was probably too high, in these experiments, leading to multi-photon dissociation; the fact that the baseline line is shifted above zero suggests that this is the case. Although it was possible to reduce the laser power, this was difficult for acquiring the spectrum due to low precursor ion intensity. The Soret band width is around 60 nm and resolved features are difficult to observe in the PD spectrum, however, both the PF spectra show three distinct defined bands in contrast with all the previous spectra. The onset of the Soret band appears to be at around 335 nm, which is 0.5 eV more than the calculated VDE, however because of the saturated spectrum, the onset of the Soret band is not well defined and as shown in both PF spectra there seems to be an increased absorption at around 350 nm.

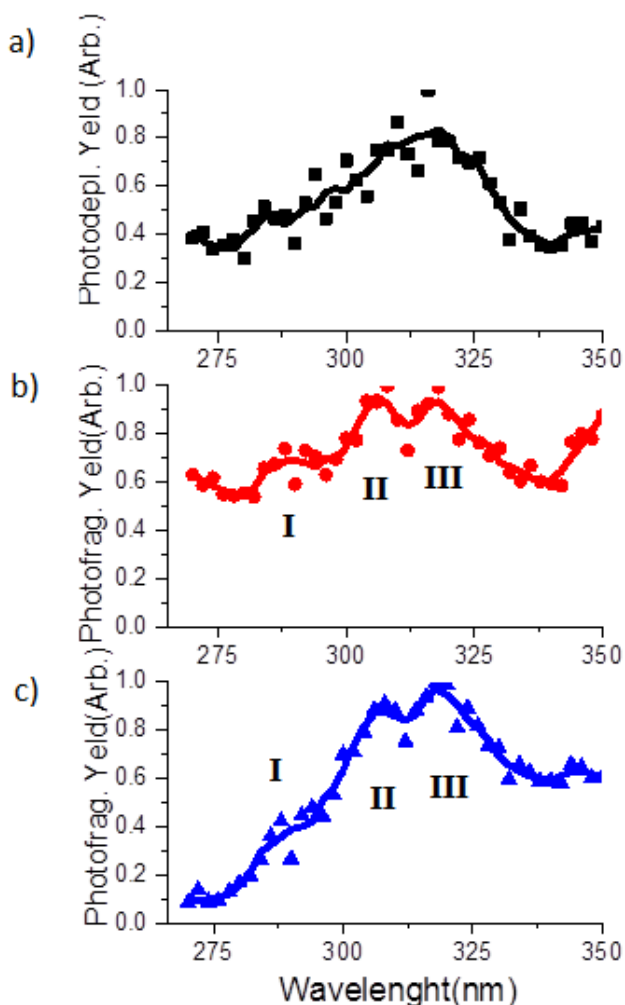
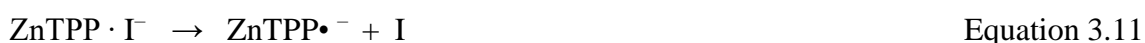


Figure 3.18 a) Gas-phase UV absorption (photodepletion) spectra of $\text{ZnTPP} \cdot \text{F}^-$ (b and c) Photofragment production spectra of the photofragment $\text{ZnTPP}\cdot^-$ and $(\text{ZnTPP} - \text{C}_6\text{H}_6)\cdot^-$, respectively. The solid line is a five-point adjacent average of the data points. The laser pulse energy was set at 0.3 mJ.

3.11 ZnTPP · I⁻ Photofragmentation mechanism

ESI generated ZnTPP · I⁻ complexes were isolated, however because of the too low parent ion intensity the PD and PF spectra were too noisy lacking identifiable peaks, therefore are not presented here. In Fig.3.19 the averaged MS spectra recorded with laser OFF and ON at 305 nm are displayed; these clearly show the production of two photofragments, namely I⁻ and the radical anion ZnTPP^{•-}. These were the only two photofragments observed across the wavelength range used and resulted from the photofragmentation channels shown in Equations 3.10 and 3.11:



Equation 3.10 shows that the same mechanism observed in the HCD experiment is in common with the photodissociation. However, according to Equation 3.11 also the electron transfer reaction occurs, resulting in the production of a neutral iodine atom and the radical anion ZnTPP^{•-}.

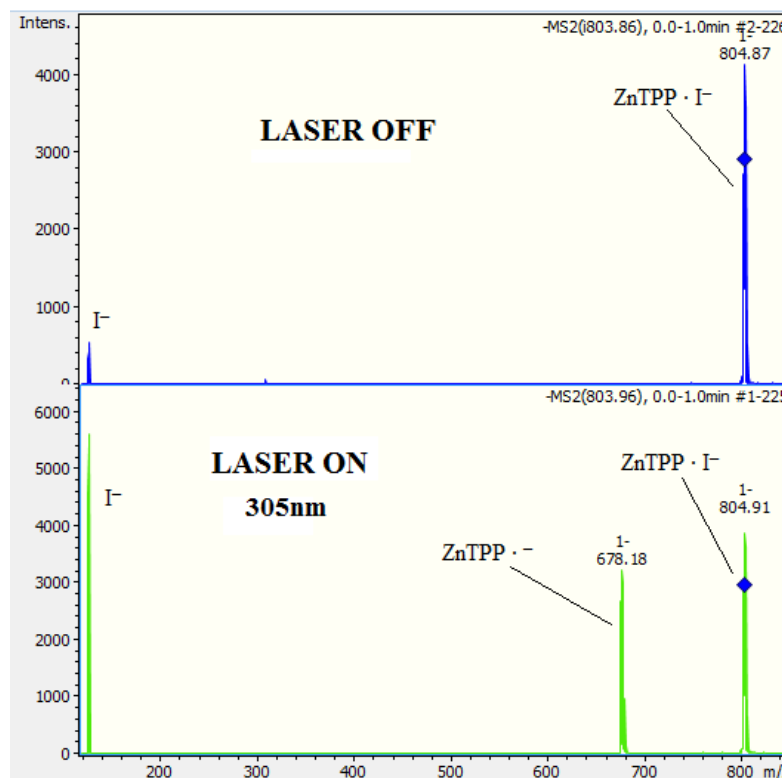


Figure 3.19 Photofragment laser off and laser on mass spectrum of ZnTPP · I⁻, excited at 305 nm.

It can be noticed that immediately after isolation of the parent ion $\text{ZnTPP} \cdot \text{I}^-$ a small signal at m/z 126.9 can be detected. This is derived from the loss of iodide during the isolation step due to the low stability of this complex. The intensity of this signal increased more than 5 times when the laser was turned on, indicating that this is indeed also a photofragmentation product.

3.12 Conclusions

In summary, this is the first time clusters of porphyrins or metalloporphyrins have been studied as complexes with anions in the gas-phase. These spectra allow for a clearer view of the fundamental absorption properties, away from the effects of the bulk solvent.

This work has proved that the ZnTPP porphyrin forms not only the 1:1 complex but also a 2:1 complex in the gas-phase and provides the complexation energies together with collision induced fragmentation mechanism.

In these complexes, the metal center charge changes remarkably with different halides, and with fluorine (the most electronegative), more charge is transferred onto the porphyrin ring (table 3.8). This is in contrast with a hypothesis reported by Nappa and Valentine stating that the charge on the metal remains relatively constant while increasing amounts of negative charge are transferred to porphyrin ring in the order $\text{F} < \text{Cl} < \text{Br} < \text{I}$ and this was believed to give an explanation to the redshift of the visible absorption spectrum upon complexation.⁸⁴

The laser experiments with the Amazon were challenging due to the instability upon isolation of the complexes, however adopting a wider isolation window and optimizing the instrumental parameters, was sufficient to obtain the PD and PF spectra of all the 1:1 complexes except the iodine one that was the most “fragile”.

All the mass spectra collected with the laser on show two photofragmentation pathways in common (Equations 3.12 and 3.13):





The photodissociation mechanism in Equation 3.12 can be observed only with the ZnTPP · I⁻ and ZnTPP · Br⁻ complexes because I and Br are the only halides with a molecular mass higher than the instrument lowest cut-off. This mechanism is in common with all the collision-induced dissociation studies, and it is reasonable to think that also the chloride and fluoride complexes follow this same photodissociation mechanism as well.

The mechanism in Equation 3.13 involves the transfer of one electron from the halide to the zinc porphyrin and was observed with all the complexes.

ZnTPP · F⁻ is the only complex that shows an additional photofragmentation pathway that involves an electron transfer to the porphyrin and an additional loss of a benzene ring. This is probably due to the striking difference in the nature and strength of the fluorine bond.

A common blue shift of the Soret band is observed. This is largely blue-shifted between 110 to 120 nm indicating a strong stabilization of the excited state by the solvent molecules (in comparison, Fe(III) heme in the gas phase is blue-shifted by only 34 nm compared to the solution phase^{94,95}); another possibility is that the absorption spectrum of these complexes is strongly solvent dependent with variations in their peak positions of around 100 nm between different solvents like in the case of the Nile blue molecule⁹⁶, however, this appears unlikely considering that the Soret band of these complexes was shifted of only around 4 nm in CH₂Cl₂ compared to benzene solutions.⁸⁴ The gas-phase Soret band is shown in table 3.12, where it is compared to the solution phase data obtained in benzene.⁸⁴ In the solution phase the Soret band is at decreasing wavelength from Br to F; this trend is not observed in the gas-phase, because the broad and less resolved peaks in the action spectra do not allow sensitivity of few nm, furthermore, it can be possible that this trend is strongly influenced by the interaction with the solvent.

Table 3.12 Soret peaks in the gas-phase and solution phase of $ZnTPP \cdot X^-$ complexes. The solution phase data are obtained in benzene from Nappa and Valentine's article.⁸⁴ The last row shows the Soret peak of the $ZnTPP$ in benzene(b)⁸⁴ and MeCN.

Complex	Gas-phase	Solution phase
$ZnTPP \cdot I^-$	na	na
$ZnTPP \cdot Br^-$	318nm	438nm
$ZnTPP \cdot Cl^-$	310nm	436nm
$ZnTPP \cdot F^-$	318nm	431nm
$ZnTPP$	na	422nm (b) 421nm (MeCN)

Chapter 4: ZnTPP and NiOEP radicals

4.1 Introduction

Porphyrins and metalloporphyrins are known for their radical-stabilizing abilities due to the extended π -system.⁹⁷ They can easily be oxidised^{98, 99} producing positive radical cations. In addition, radical porphyrin cations have also been produced by photodissociation¹⁰⁰, fast atom bombardment¹⁰¹, and ESI.^{102, 103}

The isolation of stable radical anions is more challenging because porphyrins are usually electron-rich so that the radical anions are very easily oxidized.^{97, 104}

Here we demonstrate that negative radical anions can be successfully produced and observed with the LDI technique coupled with mass spectrometry. The species analyzed in this chapter are zinc tetraphenyl porphyrin (Zn(II)TPP), and nickel octaethyl porphyrin (Ni(II)OEP) (Fig.4.1), and their action spectra and CID fragmentation and photofragmentation pathways are presented.

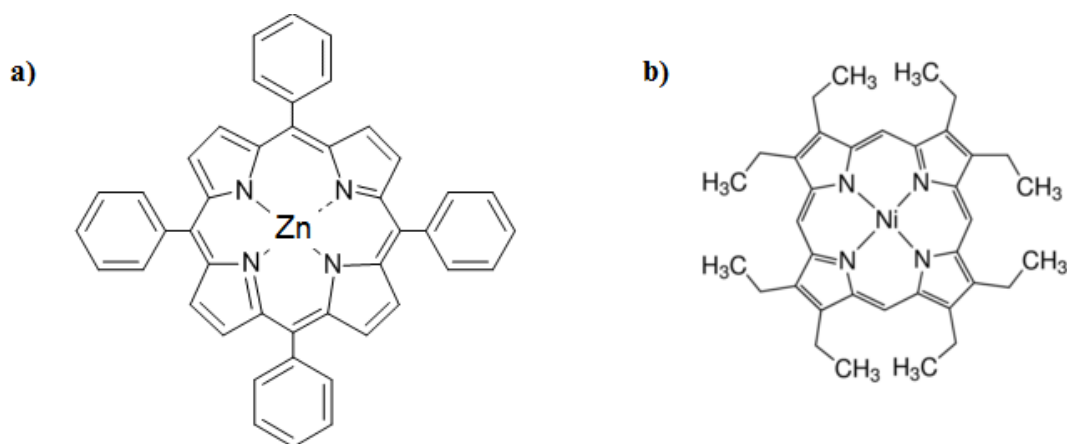


Figure 4.1 Schematic of the a) ZnTPP and b) NiOEP porphyrins.

4.2 Review of previous mass spectrometric studies on gas-phase TPP and OEP porphyrins and metalloporphyrins.

TPP type porphyrins

Gas-phase tetraphenylporphyrins (TPP) were previously studied by other authors using mass spectrometry, both as metallated and free bases: gas-phase metallated TPP were obtained as positive cations ($[M(III)TPP]^+$) with different techniques such as laser desorption and ionization (LDI), electron impact (EI) and electrospray (ESI) and only recently their fragmentation products were studied by CID showing similar fragmentation patterns via loss of benzene, two benzenes, two phenyl groups, and hydrogen molecules.¹⁰⁵ Protonated and radical cations of $M(II)TPP$ were formed previously by fast atom bombardment (FAB)¹⁰⁶ while ESI was shown to produce the protonated species of a zinc TPP porphyrin¹⁰⁷ and the radical cations of various $M(II)TPP$ species.¹⁰² Gas-phase TPP substituted free bases were obtained as protonated species using ESI and their fragmentation pattern studied by CID.¹⁰⁷

In this chapter, ESI generated $M(II)TPP$ radical cations will be studied for the first time by CID, and these results will be compared with the HCD fragmentation technique. In addition, the PD and PF spectra are presented, constituting the first example of gas-phase porphyrin radical absorption spectra.

OEP type porphyrins

Gas-phase metallated neutral octaethylporphyrins ($M(II)OEP$) were obtained in previous studies as radical cations using ESI, and their oxidation potential correlated to the effectiveness of this ionization source.¹⁰² In addition, octaethylporphyrin (OEP) and its iron(III) complex ($[Fe(III)TPP]^+$) were studied by EID and EI, showing different fragmentation pathways.¹⁰⁸ The fragmentation products of both protonated species and radical cations of ZnOEP, Cu(II)OEP, and free base OEP were studied by both low and high energy collision CID.¹⁰¹

Here, Ni(II)OEP is produced with the ESI technique and studied by CID and HCD, and its PD and PF spectra presented.

As shown by this brief literature review, radical porphyrin anions are very rarely observed and studied, however, here we show that they can be easily obtained using the MALDI technique without matrix (LDI). Their PD and PF spectra were not obtained because ESI was the only source available in our laser interfaced mass spectrometer (AmaZon mass spectrometer).

4.3 Methods

Higher-energy collisional dissociation (HCD) and CID were performed using an Orbitrap™ Fusion Tribrid mass spectrometer (Thermo Fisher Scientific, Waltham, MA, U.S.A.) as described previously.^{43, 109} The instrument was operated at 4 μL/min with the following parameters: spray voltage, 3500 V; ion-transfer tube temperature, 275 °C; vaporizer temperature, 20 °C; isolation mode quadrupole and detector Orbitrap; RF lens 80%. The HCD and CID collisional energy were varied between 0 and 100%, and the intensity of the ion in percentage was calculated.

The following CID studies were obtained with AmaZon SL dual funnel electrospray ionization quadrupole ion-trap (ESI-QIT) mass spectrometer (Bruker Daltonics Inc., Billerica, MA, USA). This technique was performed by applying an excitation AC voltage to the end caps of the trap to induce collisions of the trapped ions with the He buffer gas, as also described in detail previously.⁹²

Solutions of ZnTPP and NiOEP (1×10^{-5} M) in MeCN were introduced to the mass spectrometers. ZnTPP and NiOEP (HPLC \geq 94%) were purchased from Sigma-Aldrich and used without purification.

Gas-phase ZnTPP and NiOEP radical anions and cations were also studied with the Bruker Solarix XR 9.4 T (FT-ICR) using the MALDI source in positive and negative ion mode. The data were acquired using flexcontrol software version 3.0 (Bruker Daltonics). Each spot was analyzed in reflector mode using a smartbeam™Nd:YAG laser (355 nm). Spectra were acquired using the solarixcontrol software and processed with DataAnalysis version 4.2 (Bruker Daltonics).

The $\text{ZnTPP}^{\bullet+}$ and $\text{NiOEP}^{\bullet+}$ radical cations, PD and PF spectra were obtained using the laser-interfaced AmaZon mass spectrometer as described in Section 2.6.

4.4 $[\text{ZnTPP}]^{\bullet+}$ radical cation CID and HCD

An intense singly charged radical cation $[\text{ZnTPP}]^{\bullet+}$ (m/z 676.16) was observed upon ESI/MS of ZnTPP. The major product ion produced by CID arises from losses of a $\text{C}_6\text{H}_5\cdot$ radical (60%) followed by the loss of a C_6H_6 molecule (30%). Minor fragments arise from the loss of one and two hydrogen atoms. At higher collision voltages, the loss of two $\text{C}_6\text{H}_5\cdot$ is observed (8%), probably through a rearrangement to a more stable biphenyl molecule (Fig.4.2).

When the fragmentation is studied with higher-energy collisional dissociation (HCD) new fragments are observed. With this technique, the most abundant fragments produced are derived from losses of even species (H_2 , C_6H_6 , and biphenyl) in contrast with the CID results. With the HCD technique, up to 2 hydrogen molecules are lost and species that are derived from the loss of a benzene molecule together with hydrogen atoms or molecules are also observed (Fig.4.3). The $[\text{ZnTPP}]^{\bullet-}$ radical anion cannot be observed with the ESI source.

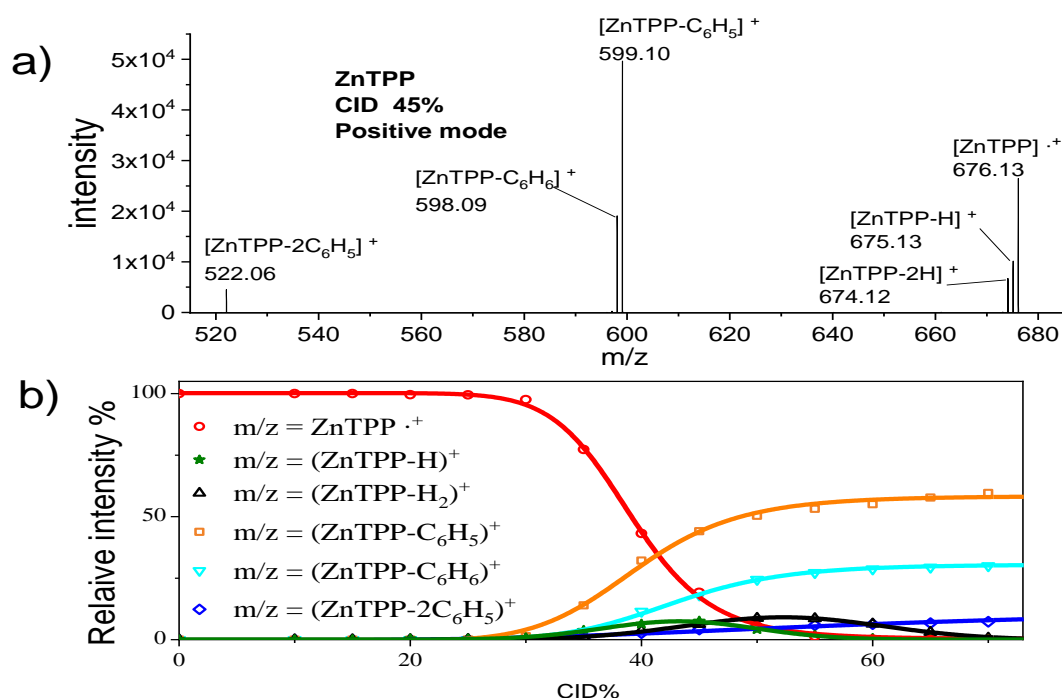


Figure 4.2 $[\text{ZnTPP}]^{\bullet+}$ CID: a) MS spectra at 45% CID voltage b) relative intensity of the precursor molecule and fragments versus collision voltage.

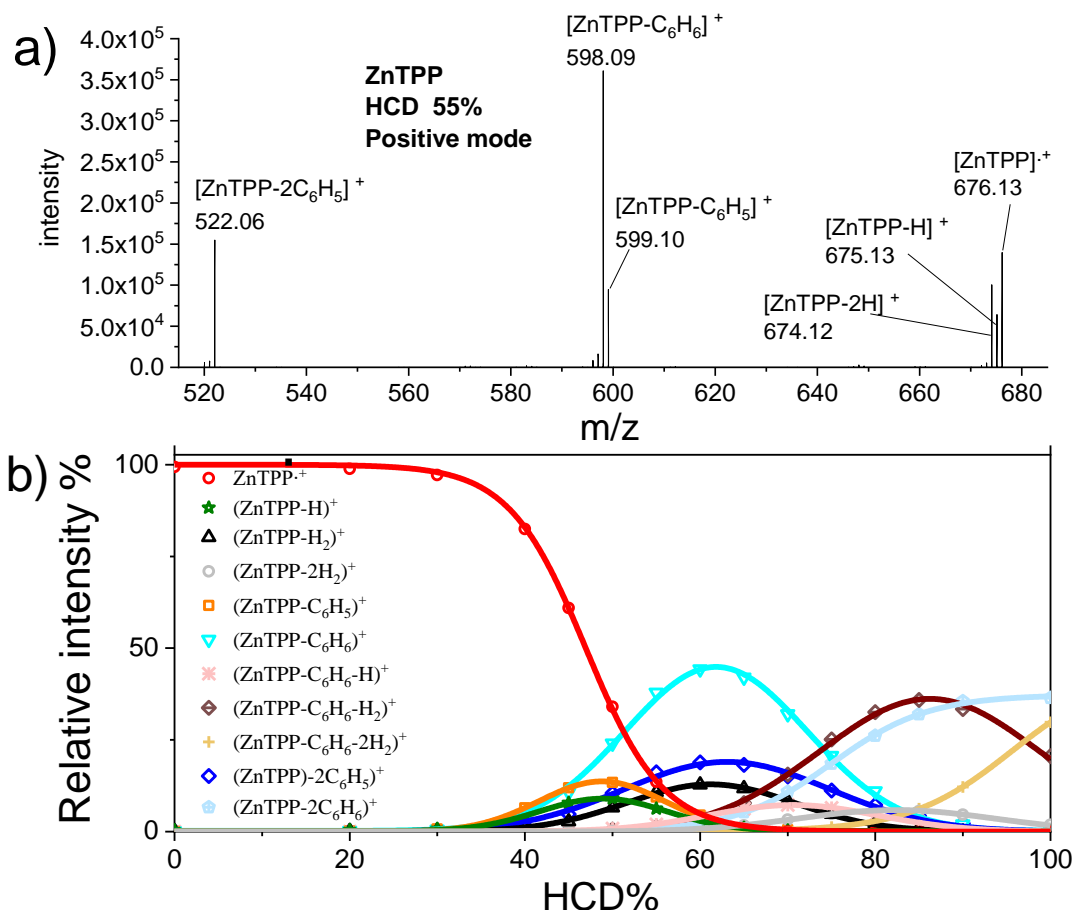


Figure 4.3 [ZnTPP]^{•+} HCD: a) MS spectra at 45% HCD voltage b) relative intensity of the precursor molecule and fragments versus collision voltage.

4.5 LDI Dissociation of the [ZnTPP]^{•+} and [ZnTPP]^{•-} radicals

Using the MALDI technique without a matrix (LDI) on ZnTPP droplets deposited on ground steel target plates, and a laser wavelength of 355 nm, it was possible to observe both the parent cation and anion radical together with their fragmentation products. In positive mode, the fragmentation is more effective than in negative mode. The same fragmentation products are observed but with opposite charges, suggesting that similar

fragmentation pathways occur but with a different probability (Fig.4.4). Many of the species observed in the LDI positive mode were also observed in the HCD dissociation.

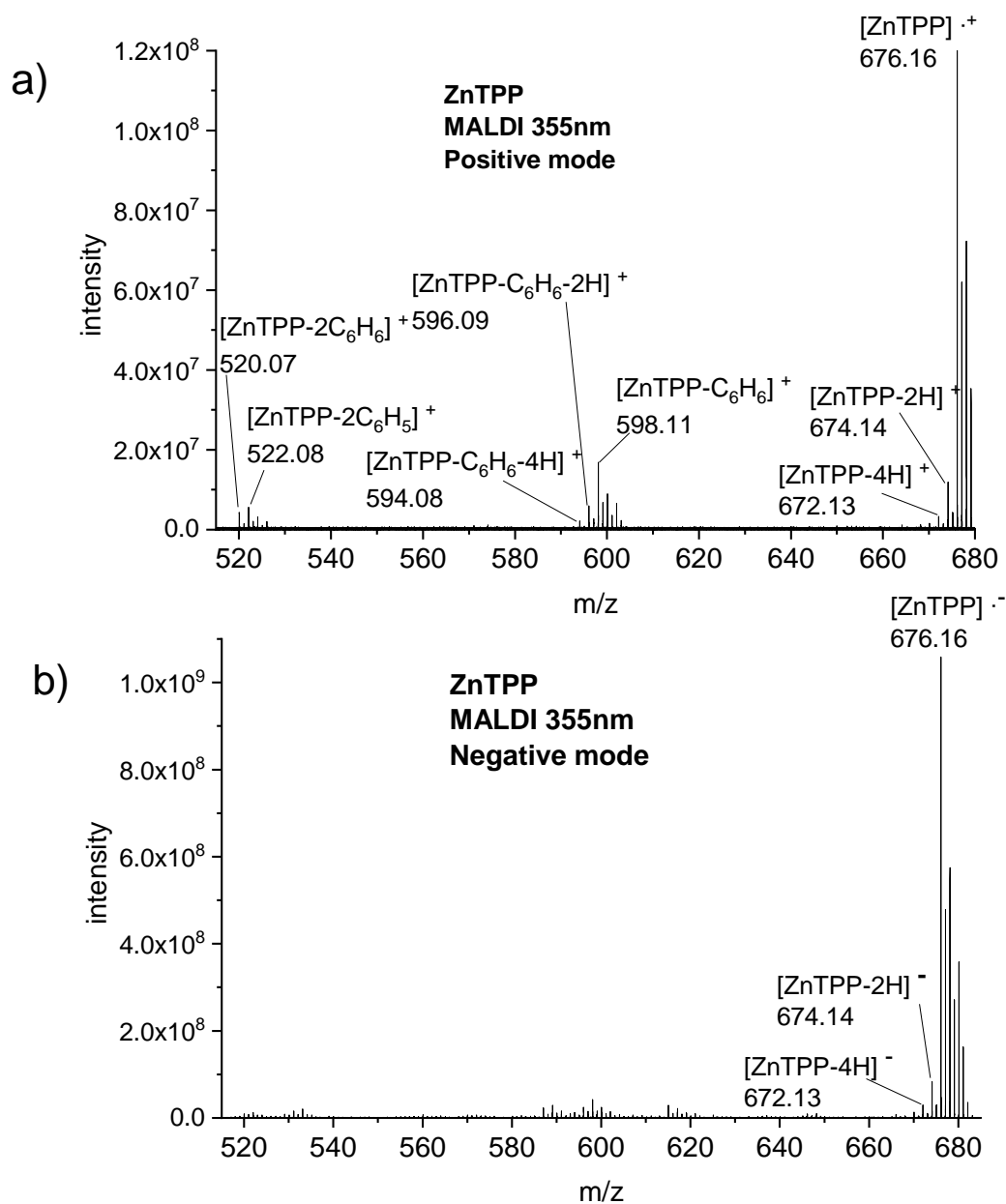


Figure 4.4 ZnTPP MALDI MS spectra: a) positive ion mode b) negative ion mode.

4.6 $[\text{ZnTPP}]^{\bullet+}$ photodepletion and photodissociation spectra

The gas-phase ZnTPP radical cation was produced using the ESI source and its photodepletion and photofragmentation spectra obtained, as described in Chapter 2.6. The photofragmentation channels of $[\text{ZnTPP}]^{\bullet+}$ are similar to the HCD products, with the major photofragments being derived from the loss of one benzene (598 m/z) and one biphenyl molecule (522 m/z) as shown in Fig.4.5.

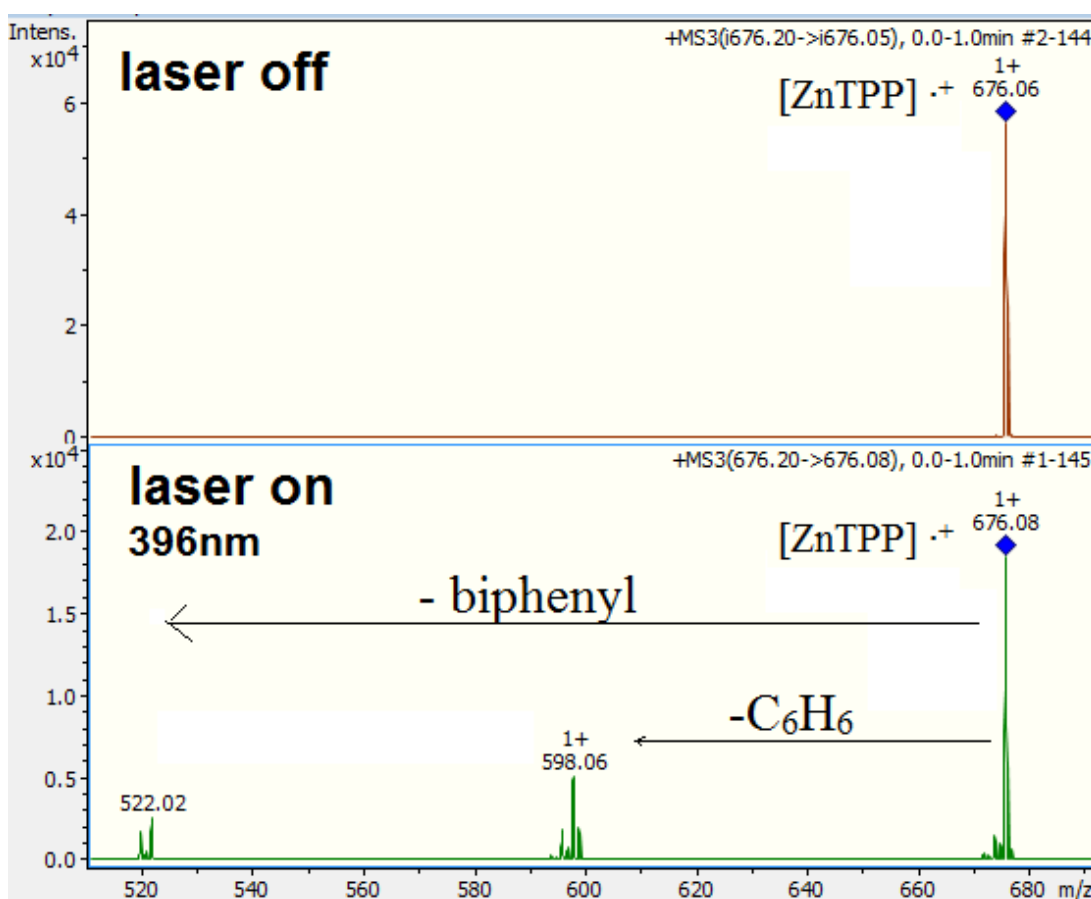


Figure 4.5 Photofragment laser off (top) and laser on (bottom) mass spectrum of $[\text{ZnTPP}]^{\bullet+}$, excited near the photodepletion maxima at 396 nm.

In Fig.4.6 the PD is shown together with the photofragmentation yield of the two major photo-products. The PD spectrum features a broad Soret band peaking at 396 nm with an additional resolved shoulder peak at 380 nm; this shoulder peak can be attributed to a

partially resolved vibronic structure,⁴¹ which appears better resolved on the photofragmentation spectra.

The Soret band is blue-shifted by about 25 nm compared to the neutral ZnTPP spectrum in MeCN (Fig. 3.11); it is expected that the Soret band of the radical cation is blue-shifted compared to the theoretical gas-phase spectrum of its neutral species due to a higher ionization potential, and this together with the solvent contribution may explain the observed shift. The difference between the first and second ionization potential of ZnTPP is small ($IP_1 = 6.97\text{eV}$ and $IP_2 = 7.05\text{eV}$)¹¹⁰ and this may account for why the blue-shift is relatively small compared to the examples in the previous chapter.

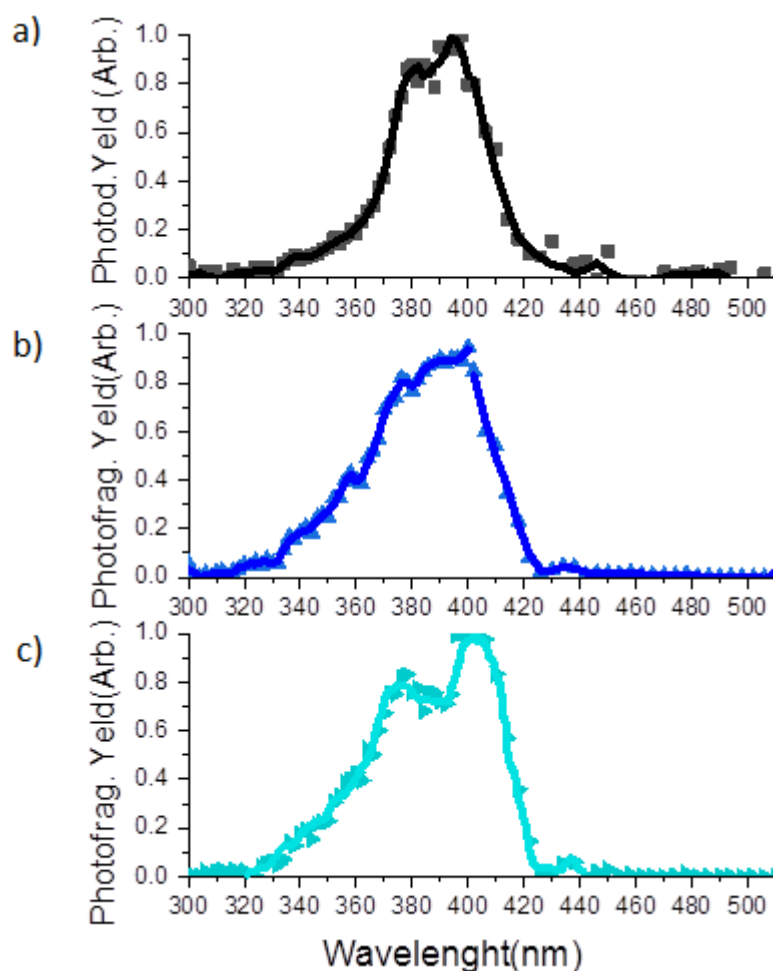


Figure 4.6 a) Gas-phase UV absorption (photodepletion) spectra of $[\text{ZnTPP}]^{\bullet+}$ (b and c) Photofragment production spectra of the photofragment m/z 598.06 ($\text{ZnTPP}-\text{C}_6\text{H}_6$) $^{\bullet+}$ and m/z 522.02 ($\text{ZnTPP}-\text{C}_{12}\text{H}_{10}$) $^{\bullet+}$, respectively. The solid line is a five-point adjacent average of the data points. The laser pulse energy was set at 0.05 mJ.

4.7 [NiOEP] \cdot^+ CID and HCD

An intense singly charged radical ion [NiOEP] \cdot^+ (m/z 590.27) was observed with the ESI/MS of a solution of NiOEP in MeCN. With the Orbitrap mass spectrometer, the major product ion produced by collision-induced dissociation (CID) arises from losses of a $\text{CH}_3\cdot$ radical (relative intensity 97%) followed by the loss of two $\text{CH}_3\cdot$ radicals probably rearranging to an ethane molecule (2%), and by the loss of an additional $\text{CH}_2\cdot$ radical (1%) possibly rearranging to a propane molecule (Fig. 4.7).

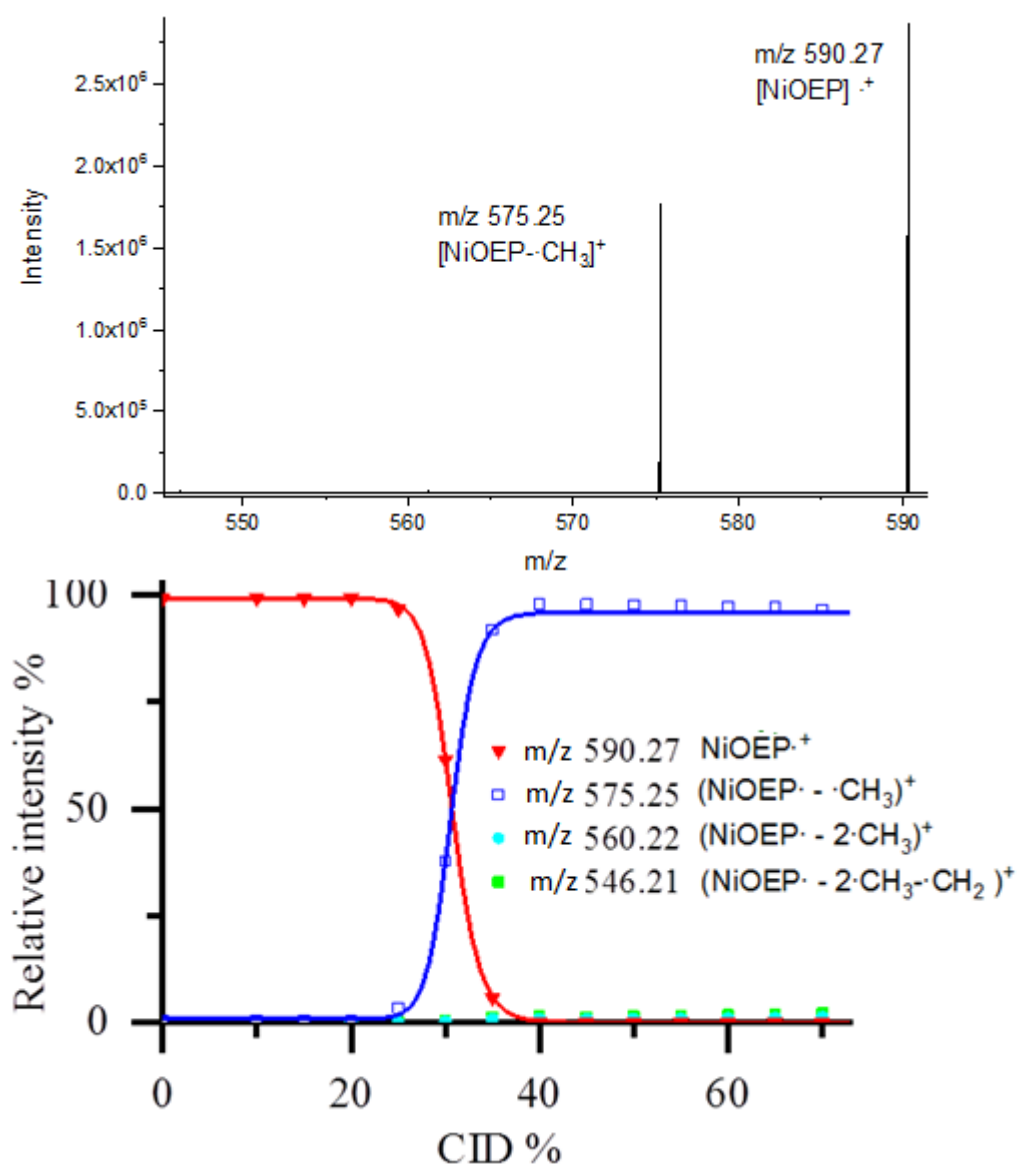


Figure 4.7 [NiOEP] \cdot^+ CID: a) MS spectra at 45% CID voltage b) relative intensity versus collision voltage. Data obtained with the Orbitrap mass spectrometer.

The CID was repeated with the laser interfaced Amazon Bruker mass spectrometer and skewed Gaussian profiles were observed for the fragment production curves: all the fragments start to be produced at 0.7 V, and their peak abundance is between 8% and 20% for all of them. More fragmentation products are observed compared to the previous Orbitrap collision experiments and are derived from the loss of a $\text{CH}_3\cdot$ radical (20%) followed by species derived from successive losses of methyl ($\text{CH}_3\cdot$) or ethyl ($\text{CH}_3\text{CH}_2\cdot$) radicals (Fig. 4.8).

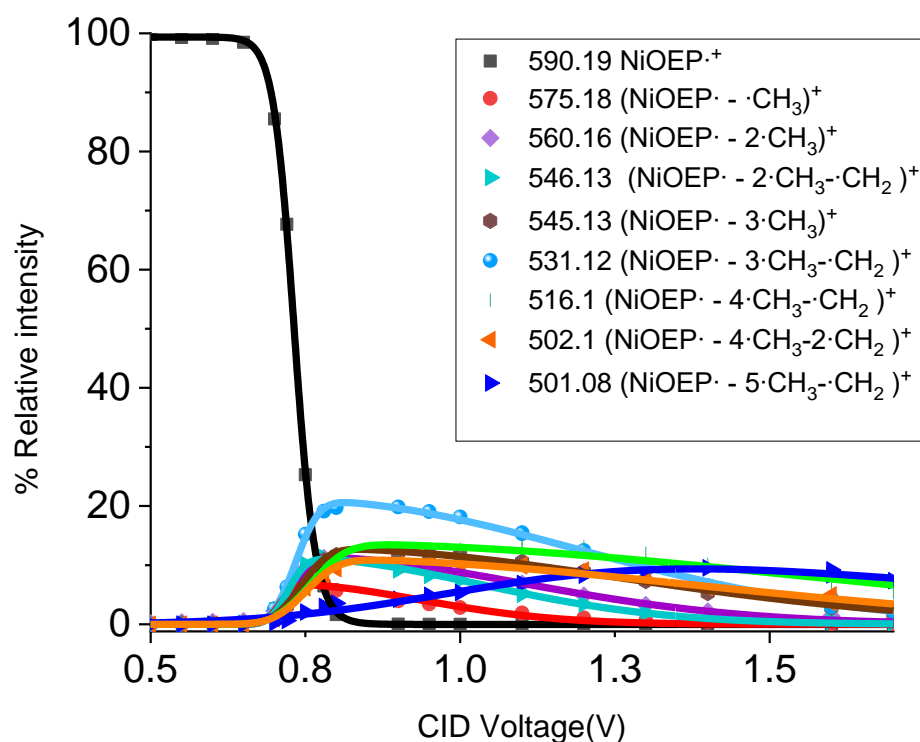
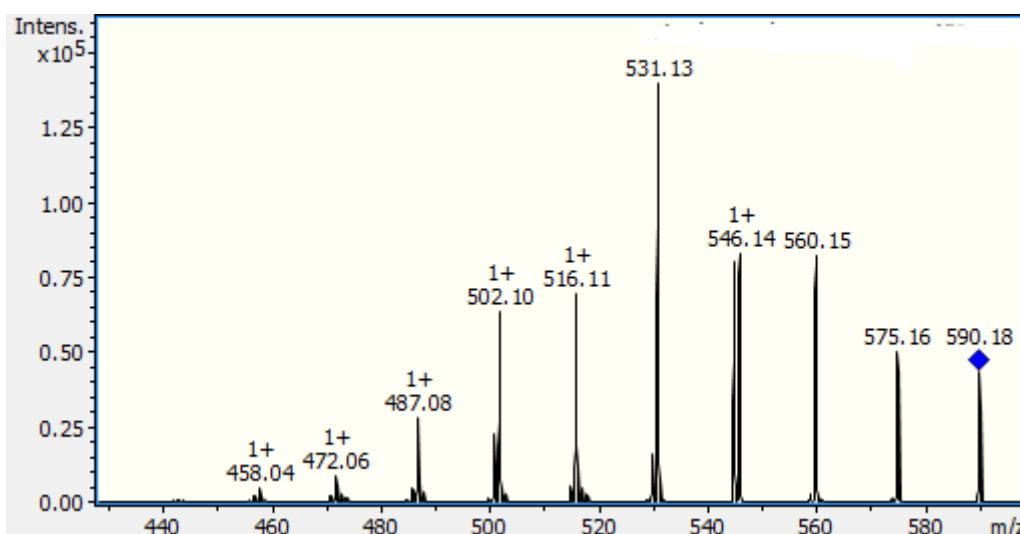


Figure 4.8 $[\text{NiOEP}]^{\bullet+}$ CID: a) MS spectra at 0.8V b) relative intensity versus collision voltage. Data obtained with the AmaZon mass spectrometer.

By comparison, the HCD process also results in many more fragments compared to the CID experiment executed on the same instrument (Orbitrap mass spectrometer). All of the fragments derived from the loss of methyl ($\text{CH}_3\cdot$) or ethyl ($\text{CH}_3\text{CH}_2\cdot$) radicals probably rearranging to more stable closed-shell species (Fig. 4.8).

At lower HCD voltages the major fragment arises from the loss of a $\text{CH}_3\cdot$ radical (55%) similar to the CID experiment on the Orbitrap, while at higher voltages many products are observed at similar peak abundances ranging between 8% and 25%.

The $[\text{NiOEP}]\cdot^-$ radical anion cannot be observed with the ESI source.

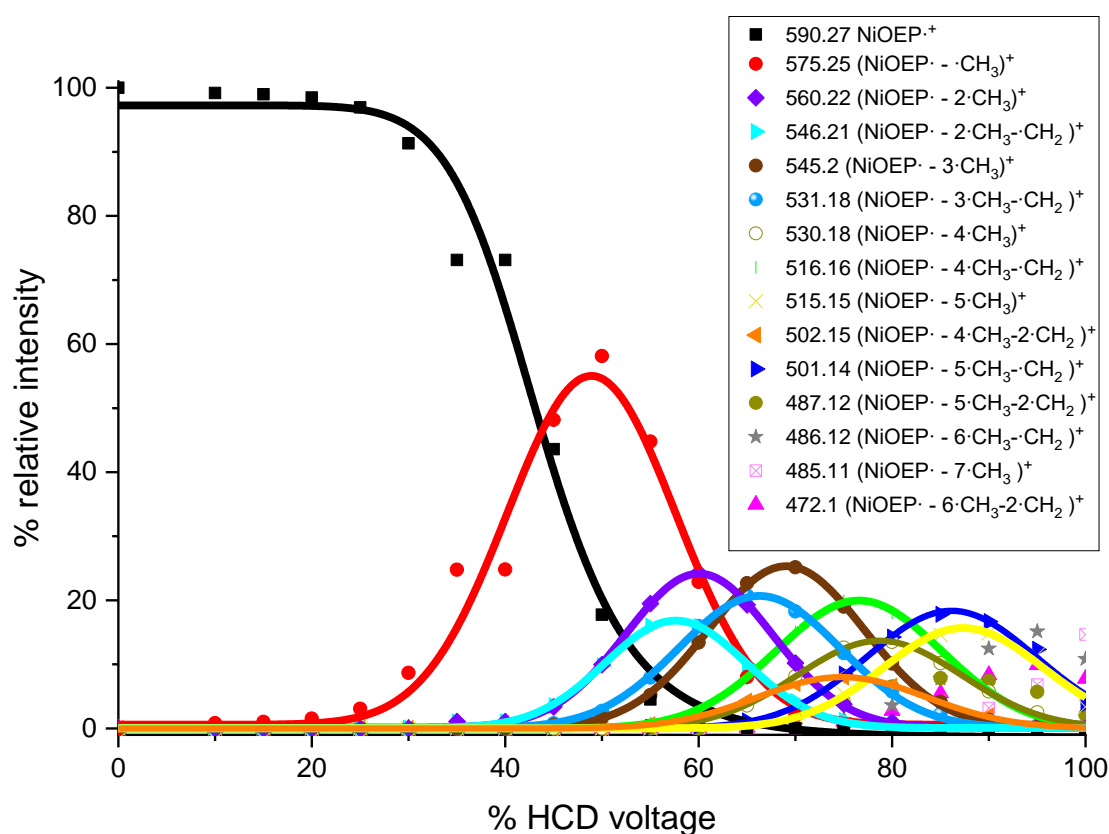


Figure 4.9 $[\text{NiOEP}]^+\text{HCD}$: plot of the relative fragmentation intensities versus % collision voltage.

4.8 LDI Dissociation of $[\text{NiOEP}]^{\bullet+}$ and $[\text{NiOEP}]^{\bullet-}$ radicals

Using the MALDI technique without matrix (LDI) on NiOEP droplets deposited on ground steel target plates and a laser wavelength of 355 nm it is possible to observe both the parent cation and anion radical together with their fragmentation products similarly to the ZnTPP case.

The same fragmentation products are observed but with opposite charges, suggesting that similar fragmentation pathways occur in both radicals.

The most abundant peaks with the LDI ionization technique are derived from subsequent losses of methyl (CH_3^{\bullet}) radicals up to eight (Fig.4.10).

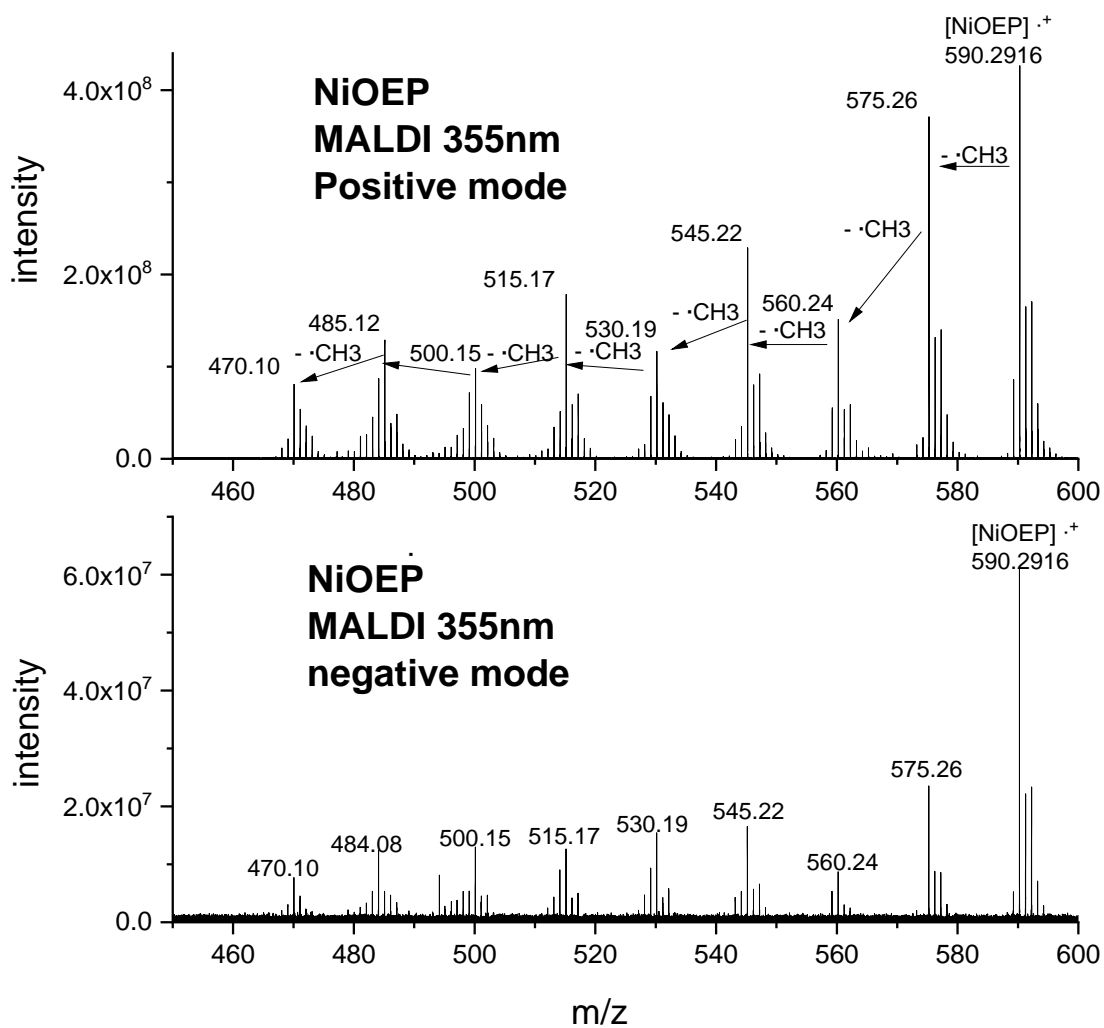


Figure 4.10 NiOEP MALDI MS spectra: a) positive mode b) negative mode

4.9 [NiOEP]•⁺ photodepletion and photodissociation spectra

The gas-phase NiOEP radical cation was produced using the ESI source and its photodepletion and photofragmentation spectra obtained, as described in Section 2.6. In Fig.4.11 the UV-Vis absorption spectra of a solution of NiOEP in MeCN is reported to allow comparisons with the gas-phase absorption spectra.

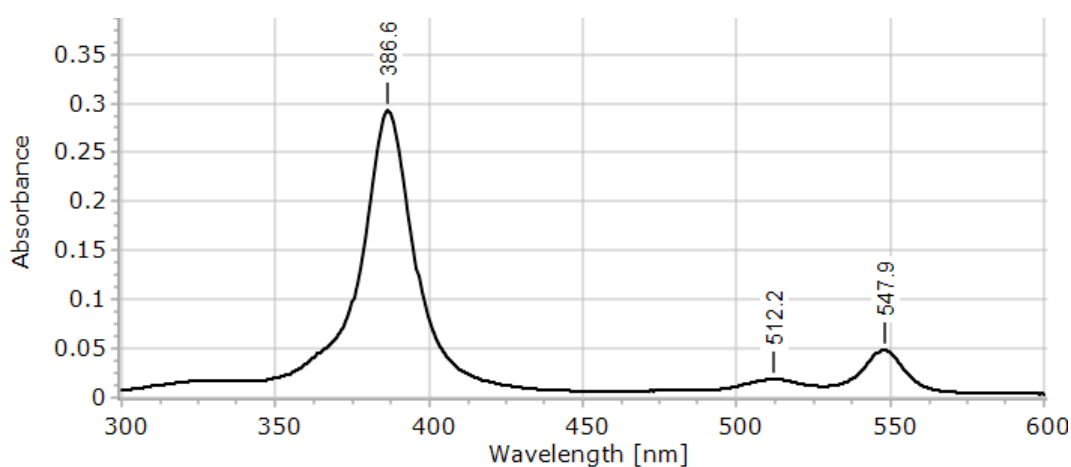


Figure 4.11 UV-Vis spectra of a solution of NiOEP in acetonitrile

The photofragmentation channels of [NiOEP]•⁺ are similar to the HCD pathways; the major photofragment is derived from the loss of one CH₃• radical (575m/z) as shown in Fig.4.12. Other slightly less abundant photofragments derived from the loss of more CH₃• and CH₂• radicals.

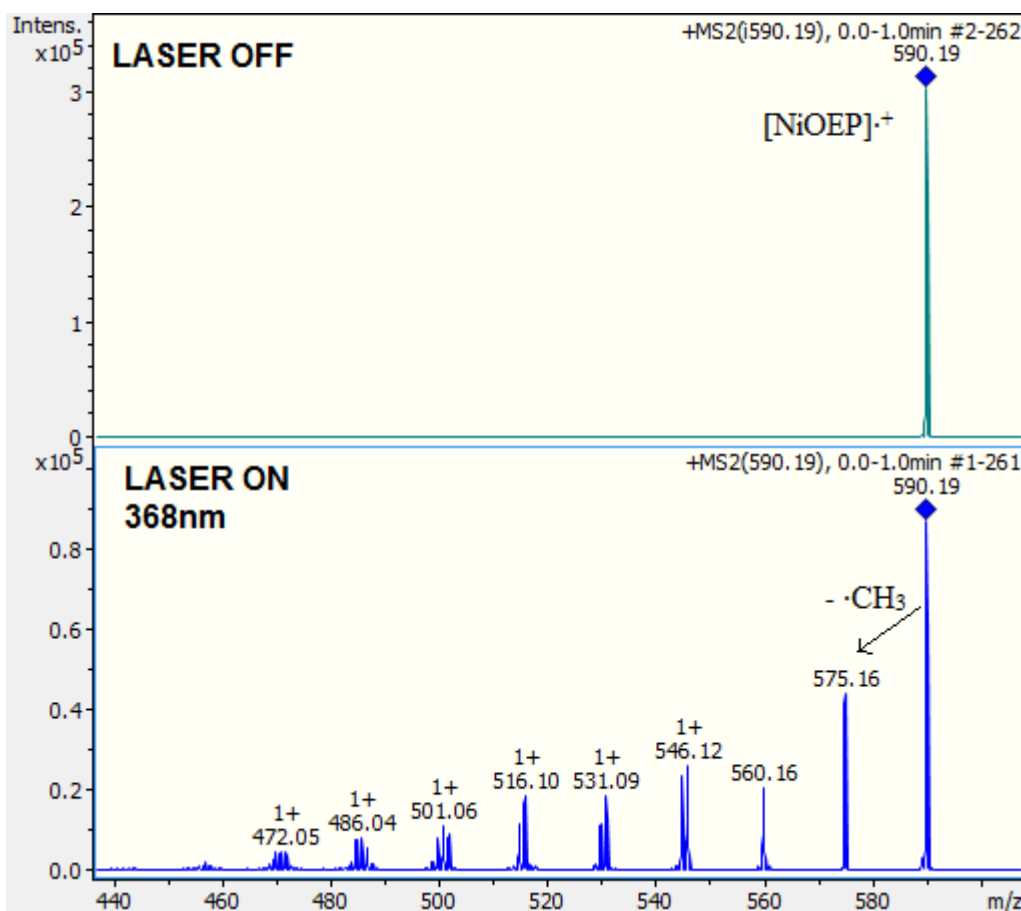


Figure 4.12 Photofragment laser off (top) and laser on (bottom) mass spectrum of $[\text{NiOEP}]^{\bullet+}$, excited near the photodepletion maxima at 368 nm. Laser pulse 0.1 mJ.

In Fig. 4.13 the PD is shown together with the photofragmentation yield of the major photoproducts. The PD spectrum features a large Soret band peaking at 368-370 nm; this is blue-shifted by about 16-18 nm compared to the NiOEP spectrum in MeCN (Fig.4.11).

Compared to the solution spectrum a shoulder peak is observed around 380 nm in both PD and the majority of the PF spectra.

The photofragments at m/z 575.16 and m/z 560.16, corresponding to the loss of one and two CH_3^{\bullet} radicals respectively, have a characteristic photofragmentation production profile that doesn't follow the PD pattern. All the other photofragments have a similar profile to the PD spectrum.

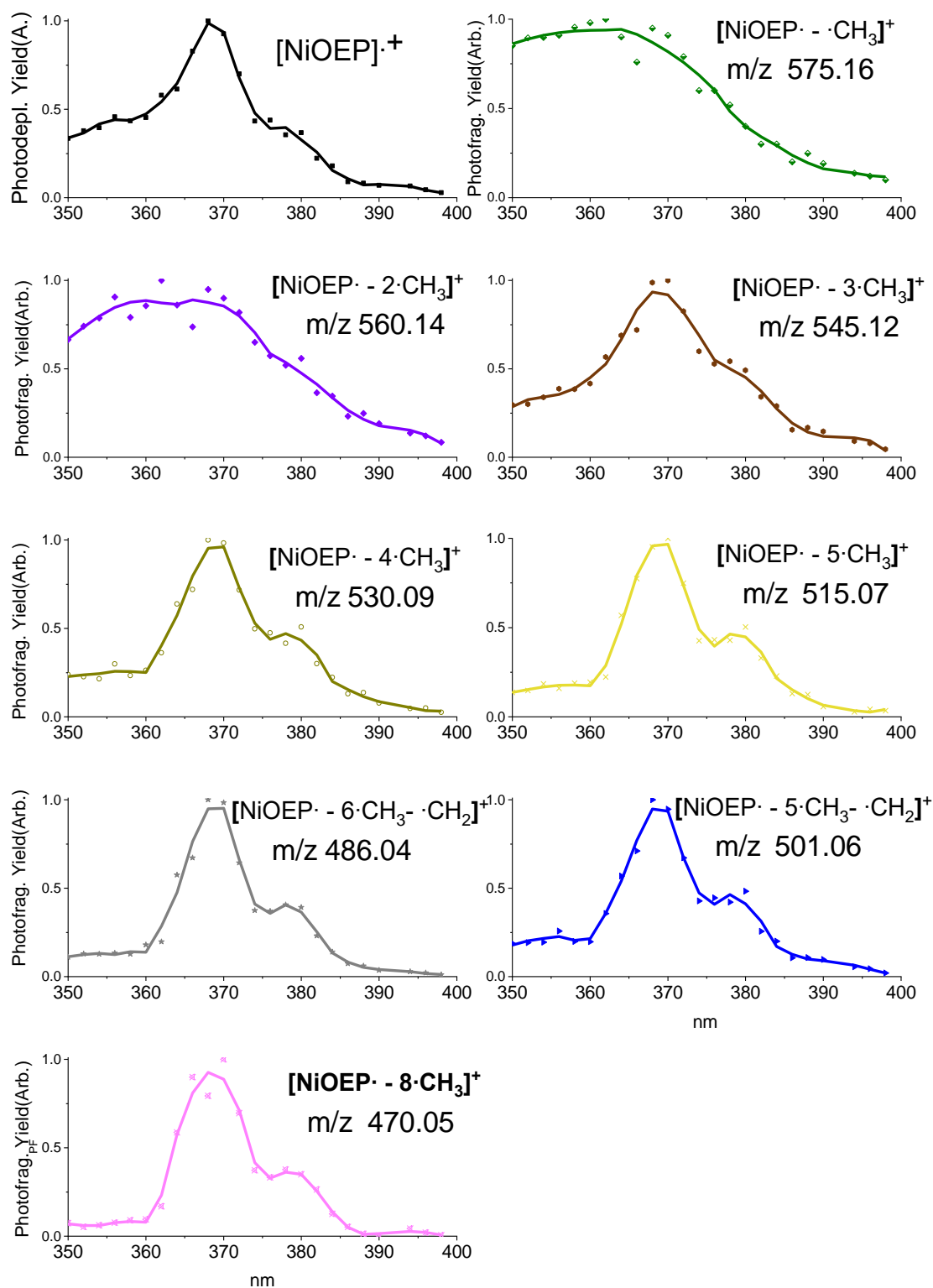


Figure 4.13 Gas-phase UV absorption (photodepletion) spectra of [NiOEP]•⁺ and Photofragment production spectra of the major fragments. The solid line is a four-point adjacent average of the data points. The laser pulse energy was set at 0.05 mJ.

4.10 Conclusions

In this chapter tetraphenyl zinc and octaethyl nickel porphyrins (ZnTPP and NiOEP) radicals were studied by electrospray ionization tandem mass spectrometry (ESI/MS) showing that intense $[\text{ZnTPP}]^{\bullet+}$ and $[\text{NiOEP}]^{\bullet+}$ peaks can be observed using the aprotic solvent acetonitrile (MeCN) while the negative radicals $[\text{ZnTPP}]^{\bullet-}$ and $[\text{NiOEP}]^{\bullet-}$ are observable with the LDI ionization technique.

The positive radicals $[\text{ZnTPP}]^{\bullet+}$ and $[\text{NiOEP}]^{\bullet+}$ dissociation pathways were probed by higher collisional dissociation (HCD) and compared with the collision induced dissociation (CID) showing a richer spectrum when HCD was applied.

$[\text{ZnTPP}]^{\bullet+}$ is proved to lose benzene, biphenyl, and hydrogen concomitantly in both CID and HCD while $[\text{NiOEP}]^{\bullet+}$ mainly fragments losing a methyl radical when CID is applied on the Orbitrap mass spectrometer. The dissociation pathways are strongly correlated to the parameters and instrument used and therefore are difficult to rationalize in terms of basic chemical properties.

The negative radicals $[\text{ZnTPP}]^{\bullet-}$ and $[\text{NiOEP}]^{\bullet-}$ are observable only with the MALDI technique applied without matrix (LDI) and using a laser wavelength of 355 nm, and in this case, a photo-induced dissociation in the source is observed. Both the positive and negative NiOEP radicals dissociate losing methyl ($\text{CH}_3\cdot$) or ethyl ($\text{CH}_3\text{CH}_2\cdot$) radicals through respectively α and β benzyl cleavage.

The photofragmentation products of both $[\text{ZnTPP}]^{\bullet+}$ and $[\text{NiOEP}]^{\bullet+}$ radicals cations are in common with the collision experiments. The PD spectra of both these radicals show a blue-shifted Soret band of 25 nm ($[\text{ZnTPP}]^{\bullet+}$) and 18 nm ($[\text{NiOEP}]^{\bullet+}$) compared to their respective neutral specie in a MeCN solution.

Chapter 5: Verteporfin

5.1 Introduction

Verteporfin is a free porphyrin base used in PDT as described in the introduction (Section 1.7). In this chapter, the thermal fragmentation pathways of this porphyrin are studied using CID and subsequently compared with the photo-fragmentation channels. The PD and PF spectra are shown and compared to the solution phase absorption spectra. These results provide unique new information on the thermal break-down products and photoproducts of this important light-triggered drug. In addition, solution photolysis experiments are used to allow comparison of the solution and gas-phase fragmentation pathways.

5.2 Experimental methods

Verteporfin ($\geq 94\%$ HPLC grade) was purchased from Sigma Aldrich and used without further purification. Solutions of verteporfin 10^{-5} M in MeCN were prepared and electrosprayed in the laser interfaced AmaZon Bruker mass spectrometer as described in the previous chapters. These solutions and the verteporfin powder were stored at -20°C in a dry environment. For the length of gas-phase experiments ($\leq 2\text{h}$), it was verified to be stable at room temperature if protected from light; this was verified by observing that its mass spectrum remained unchanged.

All the CID and PD and PF spectra were acquired using the laser interfaced AmaZon mass spectrometer. In these experiments, the first isotopic peak corresponding to the protonated verteporfin molecule was isolated (m/z 719.20) and the signal had good stability and intensity. Few droplets of NH_3 were added to the verteporfin solution and the deprotonated verteporfin signal was observed (m/z 717.23), however, after isolation

the intensity of this signal dropped off one order of magnitude and therefore no experiments were performed on this species.

The AmaZon instrument was operated at 4 μ L/min with the following parameters: ESI capillary -5000 V; End plate offset -700V; ion transfer tube temperature, 120 °C.

The photolysis experiments were conducted with a home-built photolysis cells, as described in Chapter 2.6. Unfortunately, no data on the intensity of the irradiated light is available. All the experiments were conducted in solutions of verteporfin at 10⁻³M in MeCN, and the samples were irradiated for 2h; after irradiation, the mass spectra of the solutions were taken to identify the fragmentation products. These photolysis cells employed LEDs peaking at 365 nm and 310 nm.

A second experiment was performed using the OPO laser as the photon source; the wavelength chosen was 689 nm corresponding to the peak used in PTD, and the sample was irradiated for 20 min with a laser pulse of 0.12 mJ.

5.3 CID on verteporfin

The protonated verteporfin (m/z 719.20) was isolated and its photo-fragmentation mechanisms studied using the CID technique. Fig.5.1 displays the ESI/MS spectrum that shows the CID fragmentation products and the CID plot. At around the same collision offset voltage of 0.7 V, all the fragments observed are present, and their relative abundances do not change, upon increasing the collision voltage further.

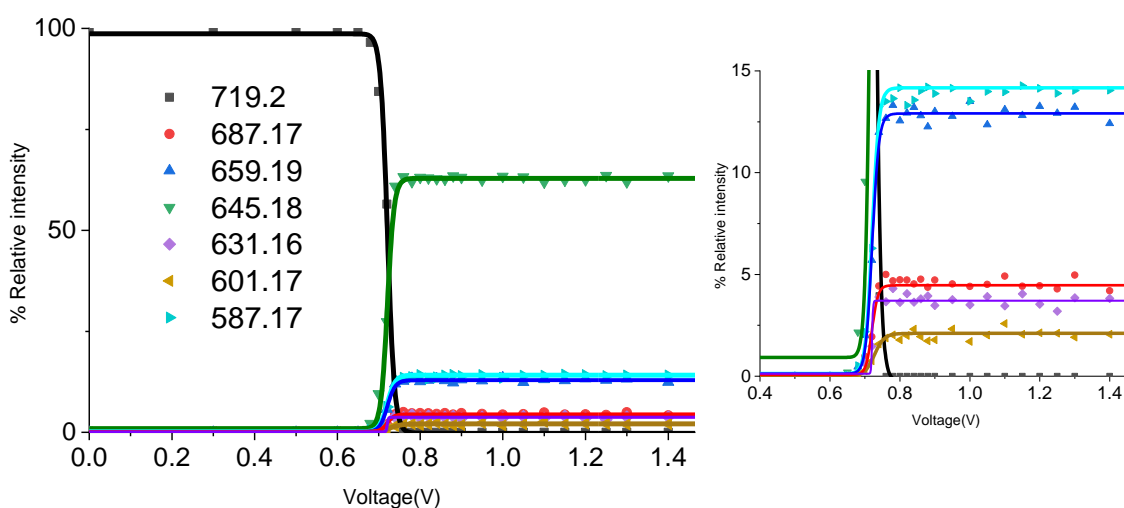
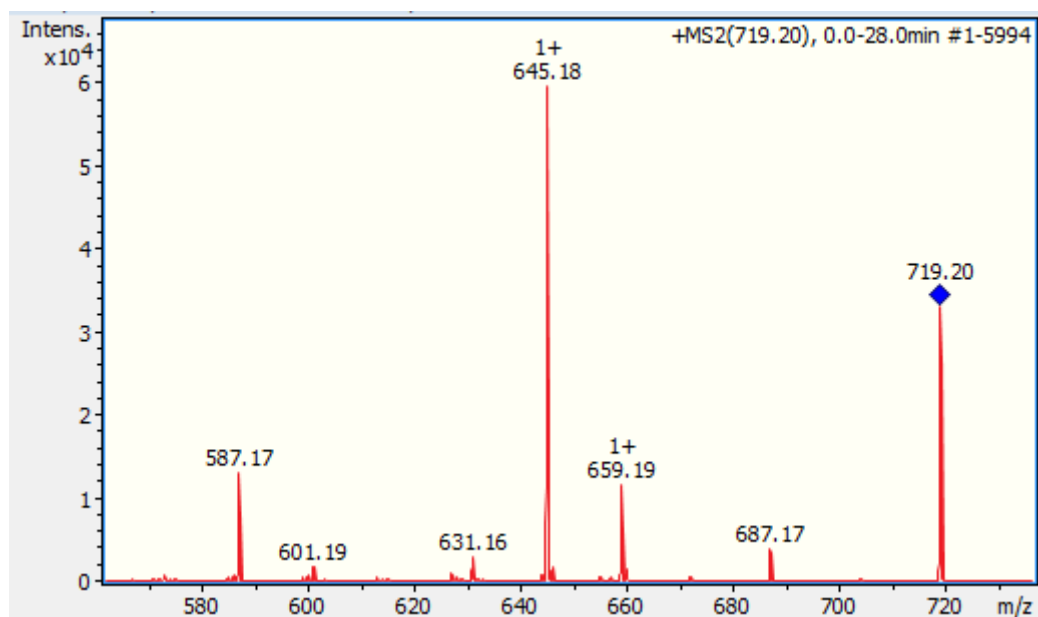
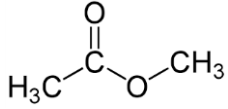
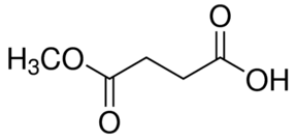
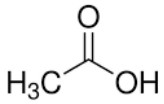
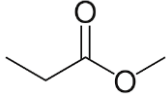
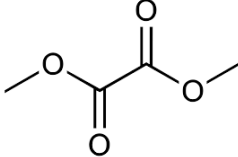


Figure 5.1 CID of protonated verteporfin: a) MS spectra averaged across the whole CID voltage range. b) Plot of relative intensity against CID voltage. A vertically expanded view of the CID results is shown on the bottom right.

These collision-induced fragments are summarised in Table 5.1 and Figure 5.2. The major product arises from a loss of methyl acetate(63%) followed by monomethyl succinate (14%), acetic acid (13%), methanol (4.5%), methyl propanoate (3.5%) and dimethyl oxalate (1.7%).

Table 5.1 Fragments derived from CID on protonated verteporfin (parent ion peak *m/z* 719.20).

Observed <i>m/z</i>	Fragment abundance	Neutral loss	
645.18	63%	methyl acetate	
587.17	14%	monomethyl succinate	
659.19	13%	Acetic acid	
687.17	4.5%	methanol	CH ₃ OH
631.16	3.5%	methyl propanoate	
601.17	1.7%	dimethyl oxalate	

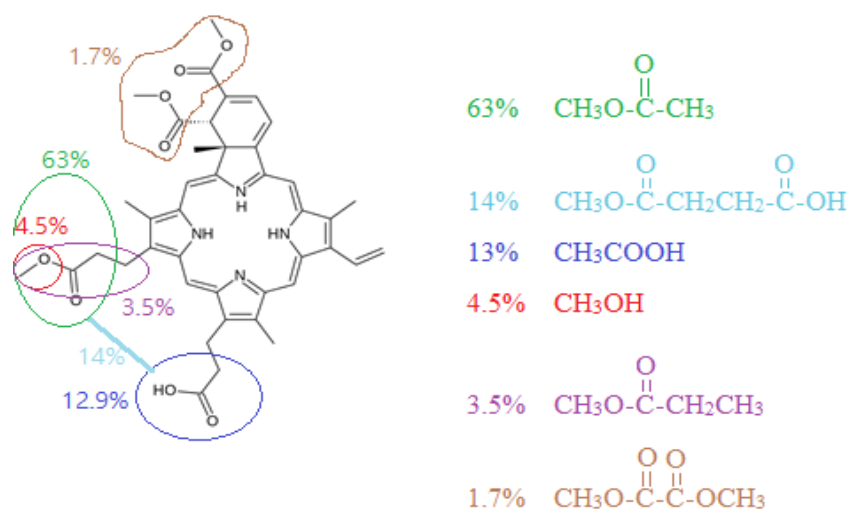
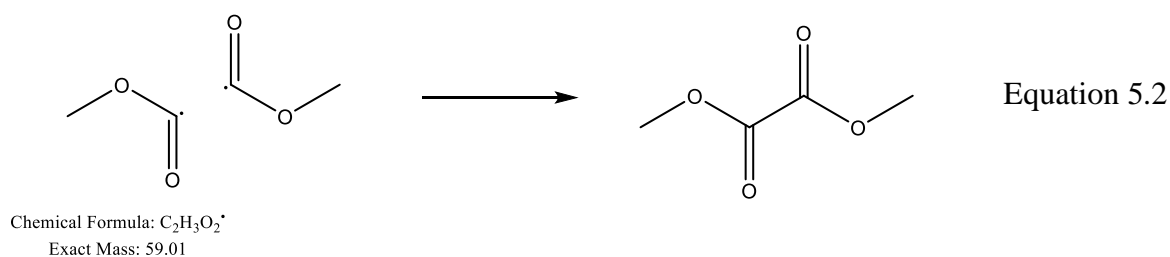
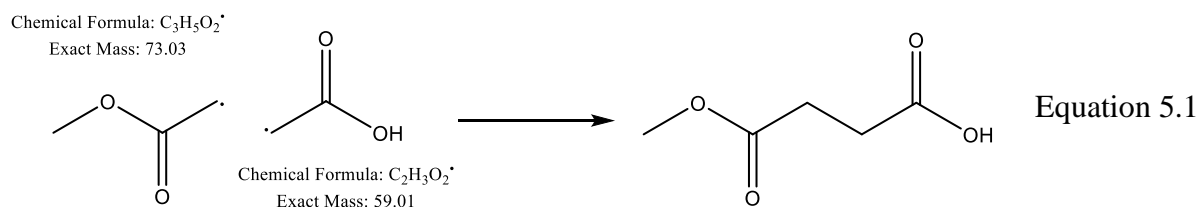


Figure 5.2 Scheme of the neutral fragments lost when CID is applied to protonated verteporfin. The proposed fragments are deduced from the observed peaks; the difference between the parent ion and the positive fragments observed is taken and assigned to a loss of a smaller neutral molecule.

Interestingly, the proposed monomethyl succinate and dimethyl oxalate derived from a combination of two radical fragments as shown in Fig.5.2 and their mechanism of production are shown in Equations 5.1 and 5.2:



5.4 Photodepletion and photofragmentation spectra

In Fig.5.3 the absorption spectra of a solution of verteporfin in MeCN is reported to allow comparisons with the gas-phase absorption spectra. Verteporfin is characterized by a distinctive strong Q band at 686 nm; this Q band is used in PDT. In addition, more peaks are observed compared to other porphyrins with simpler and symmetrical structures.

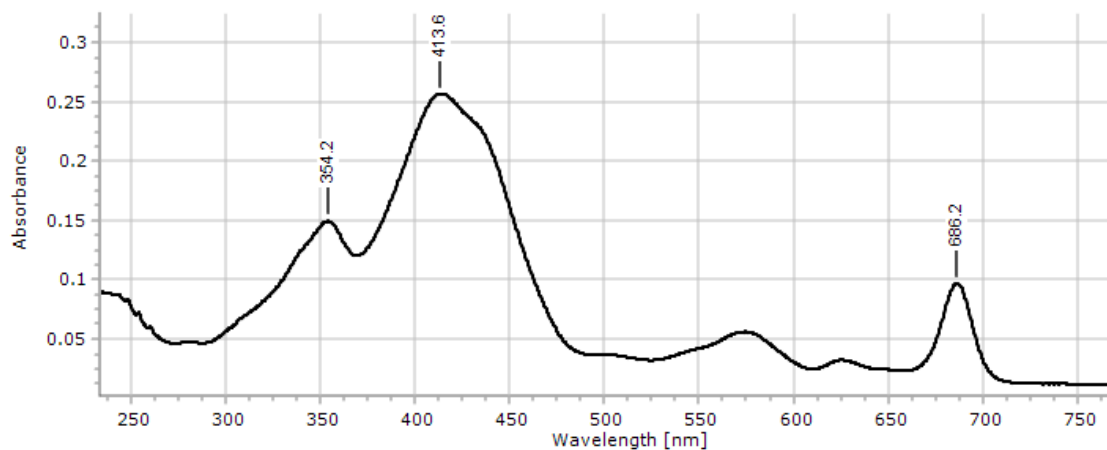


Figure 5.3 UV-Vis spectra verteporfin in MeCN

The MS spectrum obtained at 398nm is shown in Fig. 5.4; the major photo-fragment is methyl acetate similarly to the CID experiment, however many new additional fragmentation products from the precursor ion are observed, suggesting that the photo-induced fragmentation follows additional distinctive pathways.

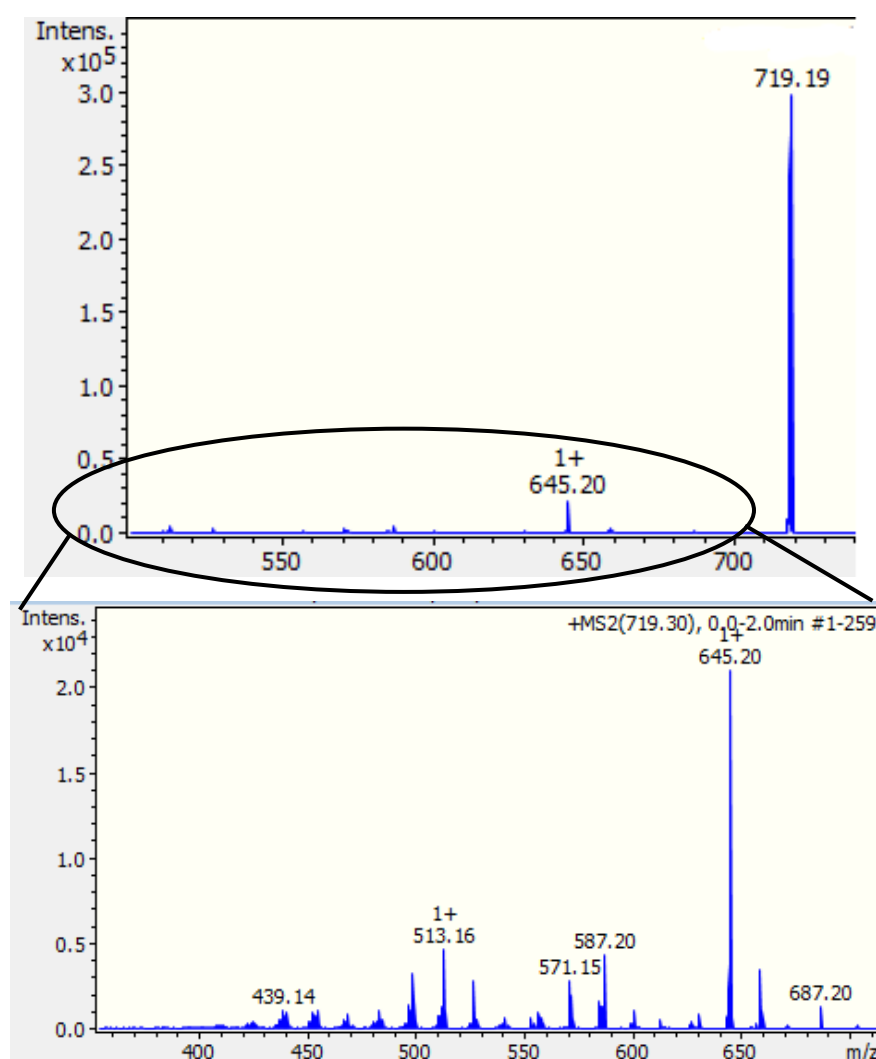


Figure 5.4 Photofragment laser laser on mass spectrum of protonated verteporfin, excited at photodepletion maxima at 398 nm. Laser pulse 0.05 mJ. The bottom spectrum is an expansion of the above spectra showing the photofragments.

Compared to the UV-Vis spectra in the solution phase (Fig.5.3), the Soret band in the gas phase is blue-shifted by 20 nm (Fig. 5.5) and its width is around 150 nm similarly to the solution phase spectrum. The Soret band in the PD spectrum appears to present a shoulder band at 430 nm that can be observed also in all the PF spectra. All the PF spectra have similar profiles and except for an additional band observed at 270 nm, their profile resembles the PD spectra.

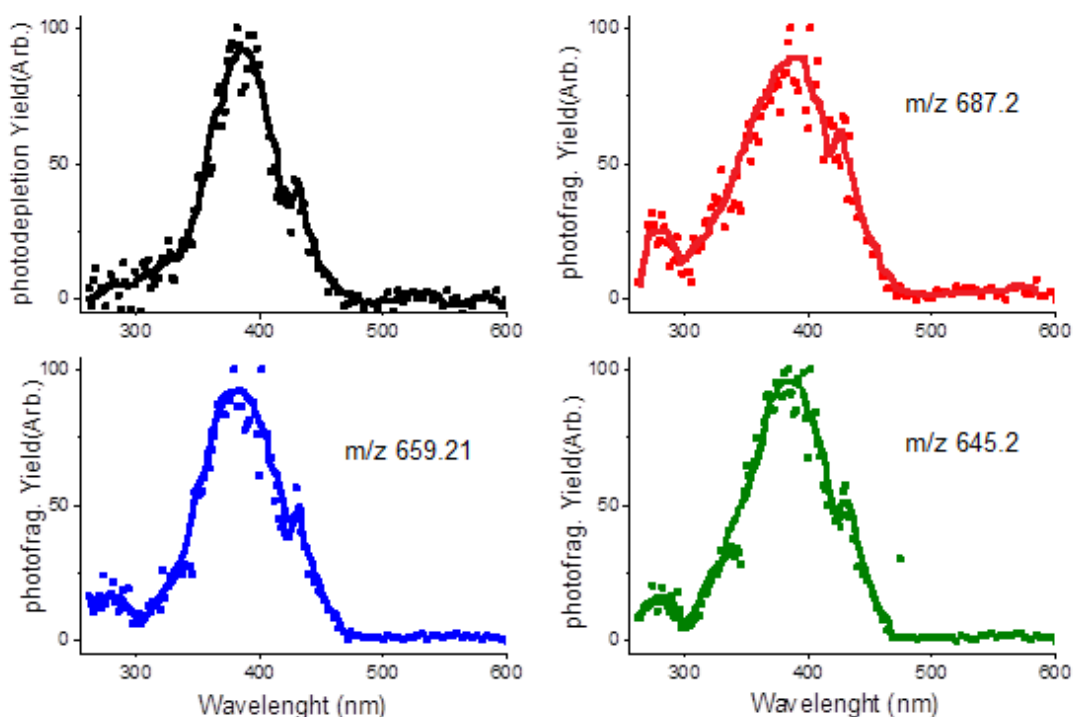


Figure 5.5 Photodepletion spectra of protonated verteporfin (black) and 3 photofragmentation spectra as examples (m/z 687.2, 659.2, 645.2). Laser pulse 0.05 mJ (400-260 nm), 0.3 mJ (402 nm to 600 nm) and m/z 200 cut-off.

The gas-phase peak that was hypothesized to correspond to the solution-phase peak at 686 nm, which is used in PDT, can be detected only in the photofragmentation spectra, and its intensity is very low, corresponding to 0.2/0.3% of the Soret band signal (Fig. 5.6). The photo-fragmentation channels are not always visible on the PD spectrum due to multiple overlapping channels contributing to it especially when the signal of interest is

particularly low. This peak is at 752 nm and is red-shifted by 66 nm compared to the solution phase. Similar large shifts were detected in gas-phase absorption spectra of protonated TPP, however, in this latter case the Q bands were blue-shifted compared to the solution phase.⁸⁸

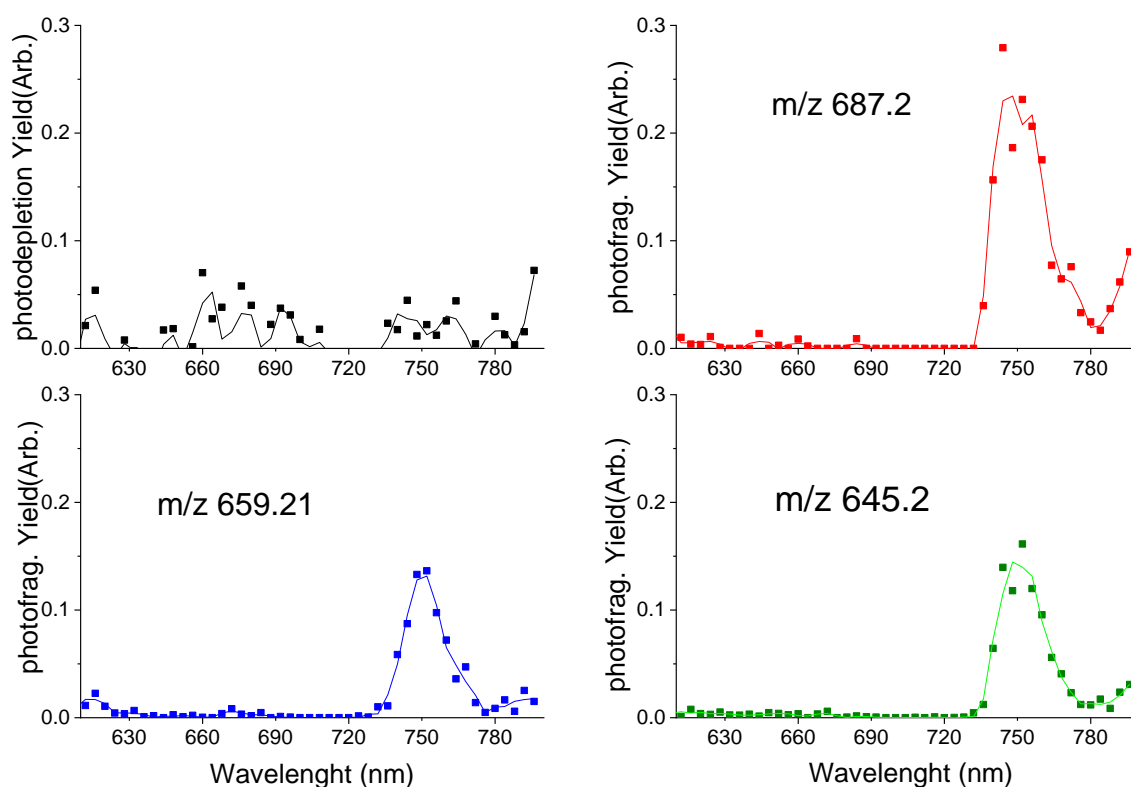


Figure 5.6 Photodepletion spectra of protonated verteporfin (black) and 3 photofragmentation spectra as examples. Laser pulse 0.2 mJ (600-800nm). Really low PF peak intensity (less than 0.2/0.3% of the Soret peak signal). 200 m/z cut-off.

5.5 Photolysis

The fragmentation products of verteporfin in the solution phase were studied using photolysis cells as described in Section 5.2. These results are summarised in Fig.5.7, which shows the ESI/MS spectra obtained from the solutions exposed to light at 310, 365 and 689 nm.

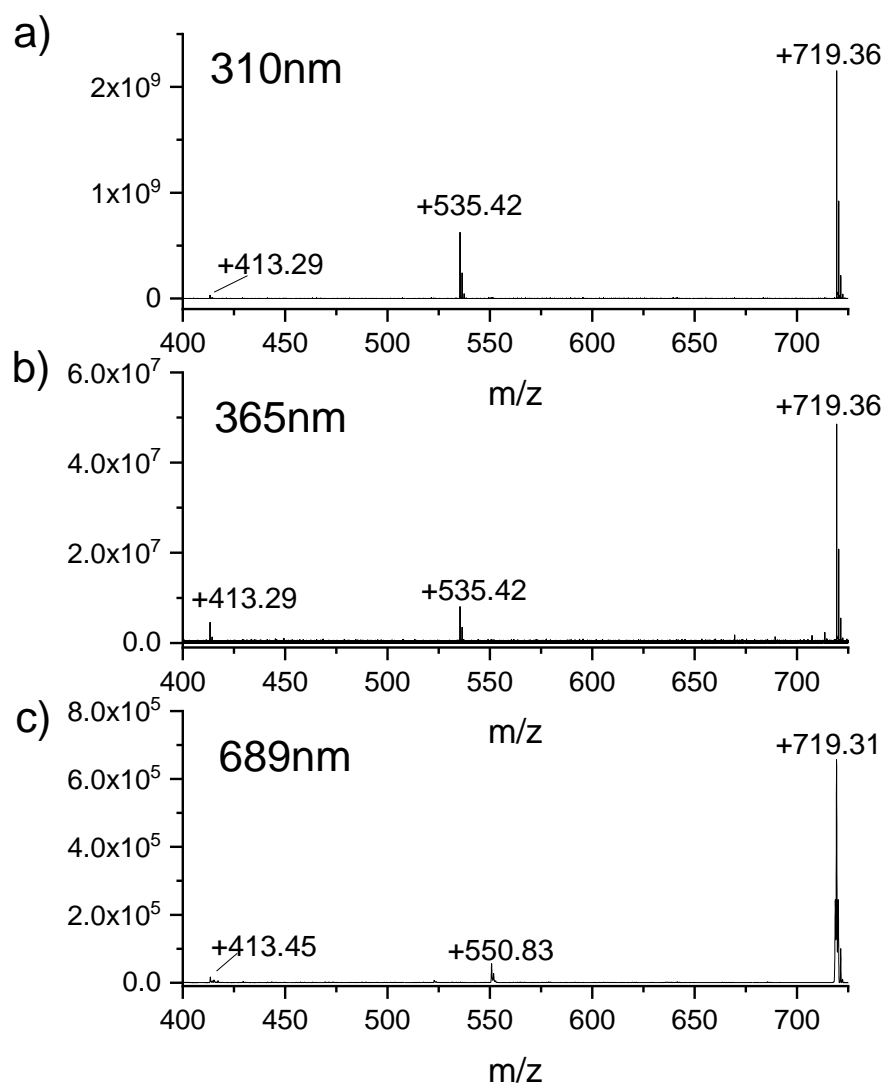


Figure 5.7 Mass spectra: a) after 2h exposure at 310nm. b) after 2h exposure 365nm. c) after 20min exposure 689nm(OPO).

At both 310 and 365 nm, the major fragmentation product observed (m/z 535.42) derives from the loss of the four major side chains and subsequent reaction with the residual water and/or oxygen, as illustrated schematically in Fig.5.8. The other fragment observed was the m/z 413.29 fragment, and was relatively more intense using the 365 nm photolysis cell compared to the 310 nm one.

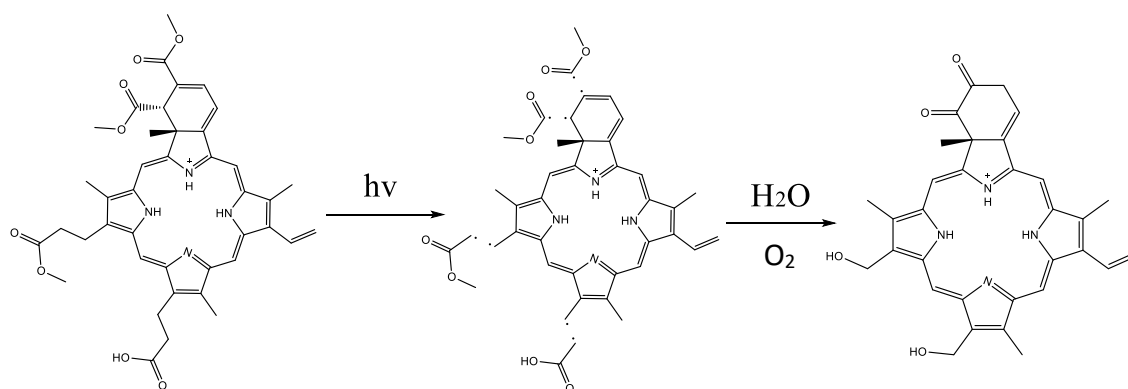


Figure 5.8 Proposed reaction scheme that leads to the main fragmentation product at $535.42m/z$.

Interestingly, all the samples discolored from pale yellow to transparent after 2h exposure to the UV light of the photolysis cells indicating that the photo-fragments produced do not absorb in the visible range.

Two fragments were observed with the OPO laser at 689 nm after 20 min exposure. The main fragment was at $550.83 m/z$, and this was not observed with the photolysis experiments in the UV region. A second fragment was observed at $413.45 m/z$ (in common with the UV photolysis). To date it has not been possible to assign the structure to these fragments, suggesting that they are formed in multi-step reactive processes.

5.6 Conclusions

The first gas-phase absorption spectra of verteporfin is shown here and it is characterized by a less resolved fine structure compared to the solution phase. The Soret band is blue-shifted by 20 nm suggesting a stabilisation of the excited state by the solvent.

The CID experiment shows that the major thermal fragments arise from the loss of neutral methyl acetate (63%) followed by monomethyl succinate (14%), acetic acid (13%), methanol (4.5%), methyl propanoate (3.5%) and dimethyl oxalate (1.7%). In comparison, the solution-phase photolysis experiments result in only two fragmentation products at the wavelength studied. The main product observed in both the solution-phase UV photolysis experiments (310 nm and 365 nm) derives from the loss of the same lateral groups as in the CID followed by a reaction with residual water present in solution and/or oxygen (Fig.5.8). The photolysis experiment at 689nm, corresponding to the peak used in PDT, shows two currently unassigned photo-fragments at 413.45 m/z (in common with the UV experiments) and 550.83 m/z (Fig.5.7-c).

Even if the proposed PDT activation mechanism, is considered to be based on the generation of highly reactive singlet oxygen ($^1\text{O}_2$) through interactions of photosensitizer, light, and oxygen ($^3\text{O}_2$, ground state),¹¹¹ a fraction of the activated photosensitizer may react with the surrounding water and solutes leading to other species that may contribute to the cytotoxic effect or alternatively the radical photofragmentation products themselves may react with the cellular biomolecules. These reaction products have been identified here for the first time following light exposure of solutions of verteporfin, and further studies may be motivated by these results to understand the extent of this contribution to cytotoxicity and to identify the species produced by simulating the typical light exposure used in the clinical setting and using solution of biological origin. At my best knowledge, no studies have been reported so far on the photofragmentation channels of verteporfin and few data are available regarding the identification of the photoproducts. The main study in this direction was carried by Gillies *et al.*¹¹², which reported the photophysical properties of a photoproduct generated in vitro from verteporfin (benzoporphyrin derivative monoacid ring A, BPD-MA) in fetal calf serum (FCS) solutions under 694 nm light irradiation, in order to provide a dosimeter for verteporfin-PDT effects. They

suggested that the changes in the absorption and fluorescence spectrum before and after irradiation are consistent with the production of a photoproduct, that was proposed to be hydroxyaldehyde; however they could not rule out the formation of other photo-products and no photo-production mechanism was determined. Furthermore, according to Gillies *et al.*, no photoproduct formation has been reported for BPD-MA in homogenous organic solutions suggesting that photoproduct formation occurred only when BPD-MA is bound to fetal calf solutions (FCS) with a high dependence on the presence of oxygen. However, in this thesis, the formation of photoproducts in solutions of verteporfin in MeCN was proved to occur; in addition, the experimental methodology presented in this thesis can be easily applied to determine the photoproducts and mechanisms in “biological” solutions. This methodology can be effectively used in support to the fluorescence spectroscopy studies so far performed.¹¹³

In this chapter, also the gas-phase photo-products were studied showing that they are substantially different from the solution-phase photolysis results, but, together with the CID fragmentation channels, they contribute to understanding the photofragmentation steps that occur in solution, for example showing the bonds that are more easily broken. In addition, they provide evidence of production of radicals.

Chapter 6: Summary and future work

6.1 Gas-phase complexes between MP and halide anions

In this thesis, the complexation energies between halide anions and different metal centers in MPs were studied, showing that the magnesium porphyrin has the highest affinity followed by ZnP, FeP, CuP. NiP was predicted to be unable to form stable complexes with the two halides studied theoretically (chloride and iodide).

The following computational studies were performed on gas-phase $\text{ZnP} \cdot \text{X}^-$ complexes ($\text{X} = \text{I}, \text{Br}, \text{Cl}, \text{F}$) revealing the structural and electron density changes that occur upon complexation. The calculations predicted a higher affinity towards hard ligands, and this was in line with previous solution-phase studies on zinc porphyrin complexes with halide anions.^{84,85} Experimentally, these trends were confirmed with the HCD technique applied to ESI generated gaseous $\text{ZnTPP} \cdot \text{X}^-$ complexes ($\text{X}=\text{I}, \text{Br}, \text{Cl}, \text{F}$) and in addition, the formation of $(\text{ZnTPP})_2 \cdot \text{X}^-$ complexes was observed for the first time.

Finally, the first gas-phase action spectra of $\text{ZnTPP} \cdot \text{X}^-$ complexes are presented in this work, including their photofragmentation products. These complexes are characterized by a particularly strongly blue-shifted (110-120 nm) Soret band compared to the solution phase; usually, large shifts are attributed to a specific chemical effects of the solvent on one or both electronic states of the chromophore interaction¹¹⁴ and to investigate further this unusual large shift, theoretical DFT studies that include solvation models could be applied. Additionally, the structure of these complexes could be further characterized using IR gas spectroscopy available in a custom-built instrument combined with an ESI source, such as the one described by Garand *et al.*¹¹⁵

6.2 ZnTPP and NiOEP radicals

In this thesis, the first thermal fragmentation study on radical cations of ZnTPP and NiOEP using CID and HCD is presented, showing similar fragmentation channels to other OPE and TPP porphyrins. Additionally, their gas-phase absorption spectra are here reported and their photoproducts compared to the thermal fragmentation ones.

Additionally, the negative radicals of both ZnTPP and NiOEP were produced using the MALDI technique without any matrix applied (LDI); to the best of my knowledge, these are the first reported porphyrin radical anions produced with this technique and MALDI may therefore be considered in future studies as a method to produce radical anions of porphyrin-like molecules. Other future studies can include gas-phase spectra of radical porphyrin anions and negative ion photoelectron spectroscopy.¹¹⁶

6.3 Verteporfin

In PDT, the photoproducts generated exposing the photosensitizing molecules to light can be important in understanding the cytotoxicity effects. So far, no known study determined directly the photoproducts and their production mechanisms in verteporfin molecules. In this thesis, CID thermal fragmentation, gas-phase photofragmentation, and photolysis experiments were used to determine the photodegradation channels of verteporfin molecules that were shown to involve radical species derived from the loss of carboxyl and ester groups. In addition, the first gas-phase absorption spectrum of protonated verteporfin molecules revealed its intrinsic photophysical properties.

These gas-phase techniques can be used in future studies to determine the photoproduction mechanisms of different photosensitizing molecules and photolysis experiments coupled with mass spectrometry can be used to determine the photoproducts in solution and therefore understanding their contribution to cytotoxicity.

In addition, these experiments can also be important in assessing the photostability of pharmaceuticals over the therapeutic time scale as part of the product development process in the pharmaceutical industry.¹¹⁷

Appendix A1

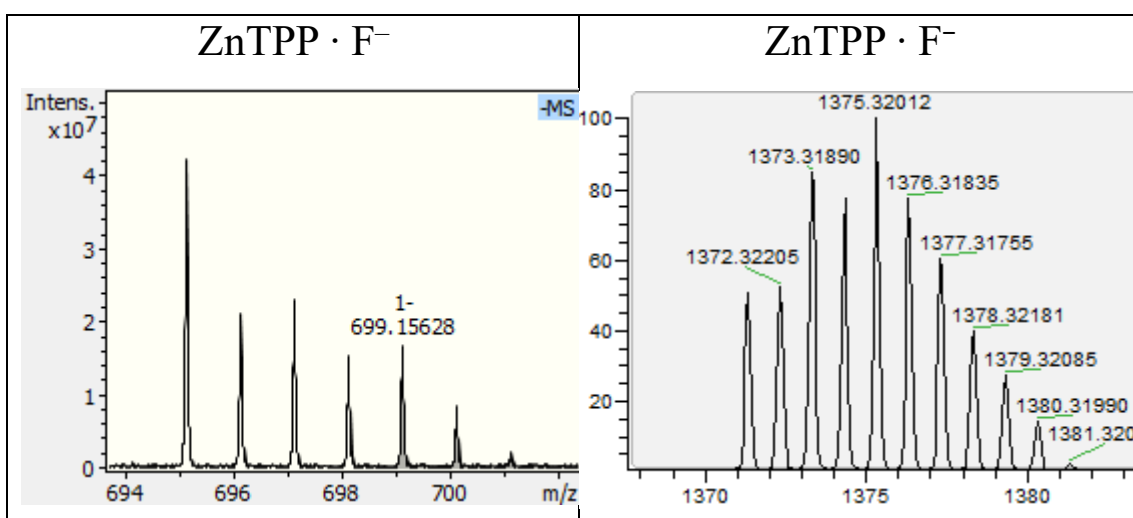
A1.1 Introduction

In this appendix, additional ESI/MS spectra and optimized DFT geometries are presented together with the PD spectra of iodide and bromide.

The following appendix A2 presents the computer programs that were developed as part of this thesis for the automated analysis of the experimental data in order to generate the CID plots, and PD and PF spectra.

A1.2 $\text{ZnTPP} \cdot \text{X}^-$ and $(\text{ZnTPP})_2 \cdot \text{X}^-$ ESI/MS spectra

The mass spectra of the ESI generated $\text{ZnTPP} \cdot \text{X}^-$ and $(\text{ZnTPP})_2 \cdot \text{X}^-$ complexes are here reported (Fig. A1.1). All the spectra were recorded with the Bruker solariX mass spectrometer except the $(\text{ZnTPP})_2 \cdot \text{F}^-$ that was recorded with the Orbitrap mass spectrometer.



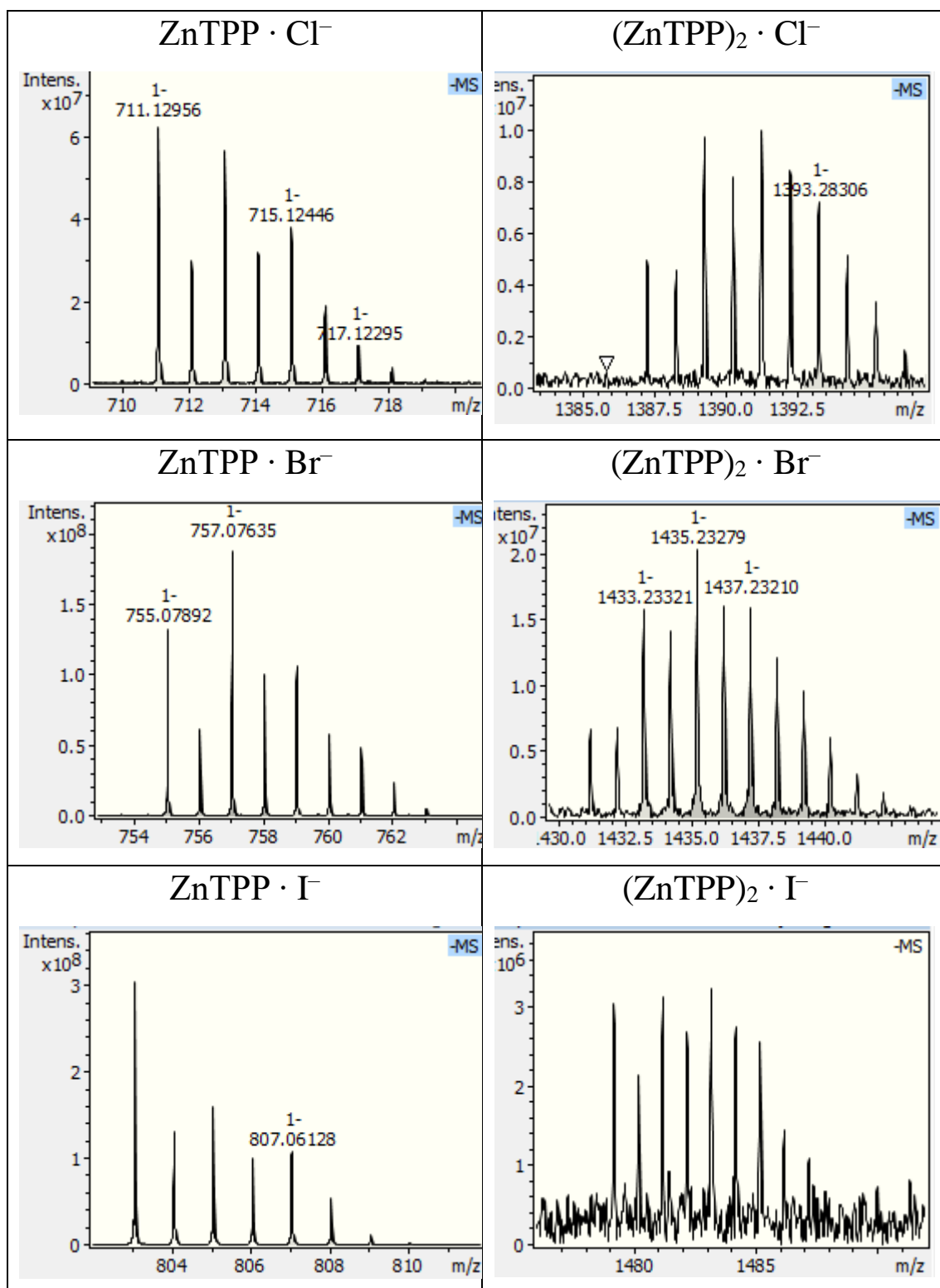
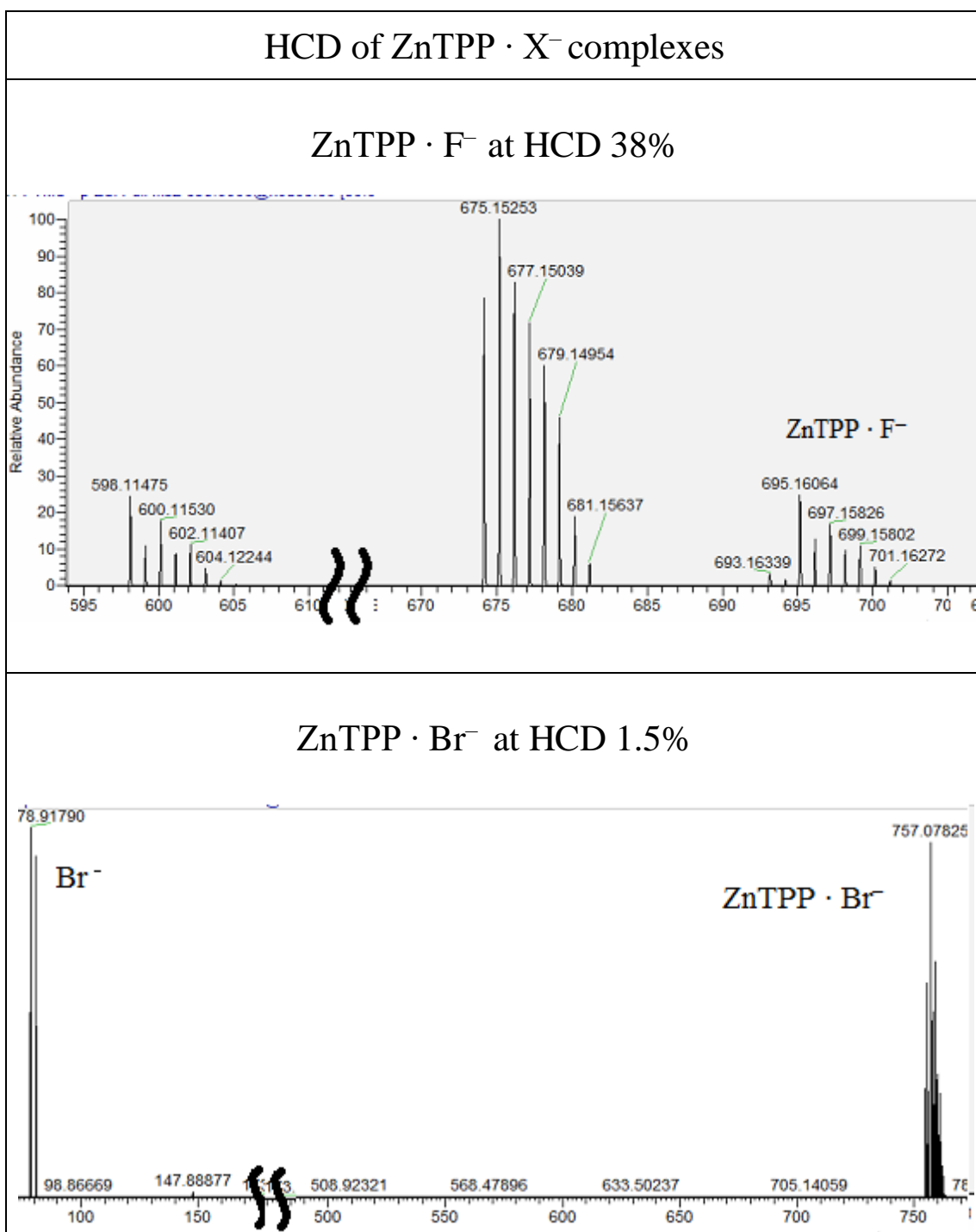


Fig A1.1 MS spectra of ZnTPP · X⁻ and (ZnTPP)₂ · X⁻ complexes. All the isotopic peaks are displayed.

A1.3 HCD $\text{ZnTPP} \cdot \text{X}^-$ and $(\text{ZnTPP})_2 \cdot \text{X}^-$ ESI/MS spectra

In Fig. A1.2 and A1.3 the MS spectra at different HCD voltages of the $\text{ZnTPP} \cdot \text{X}^-$ and $(\text{ZnTPP})_2 \cdot \text{X}^-$ complexes are displayed. The 2:1 complexes dissociate producing the signal corresponding to the $\text{ZnTPP} \cdot \text{X}^-$ complex.



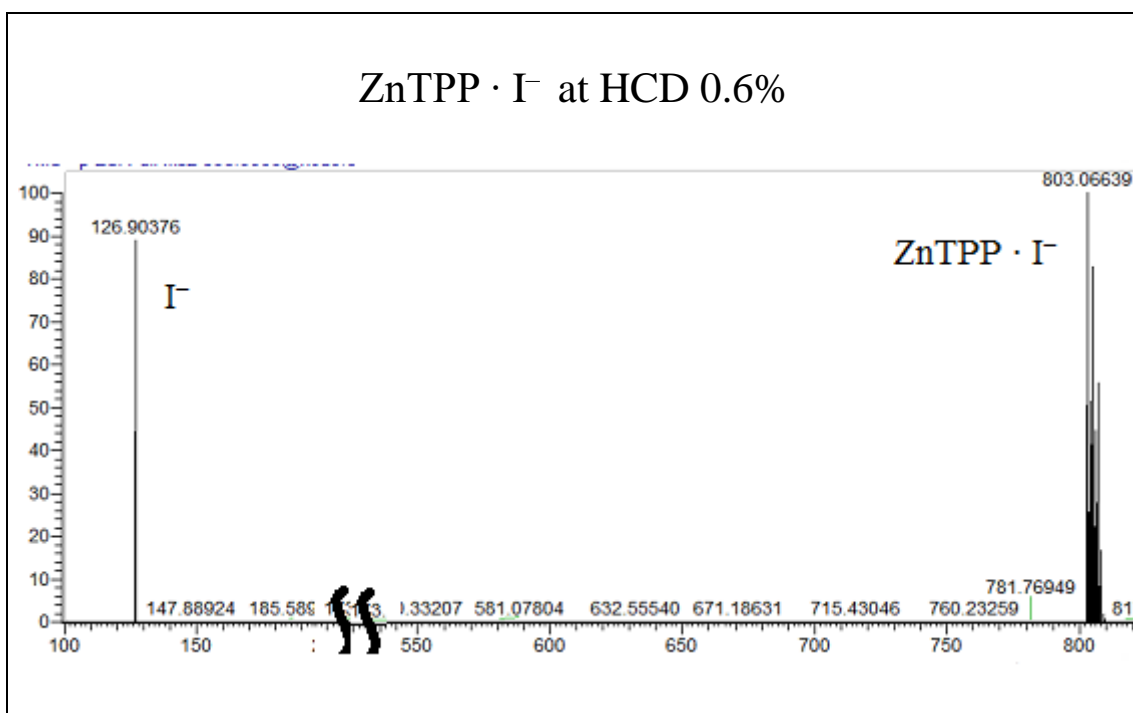
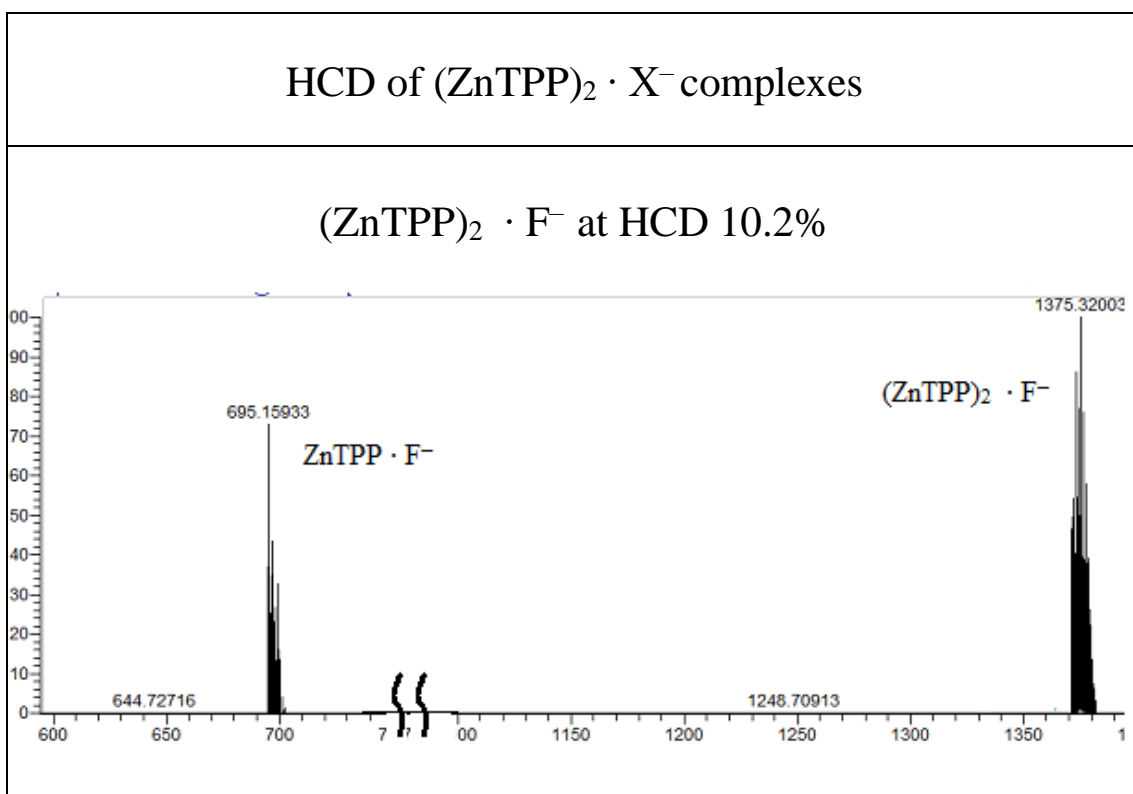


Fig A1.2 MS spectra of ZnTPP · X⁻ complexes when HCD is applied.



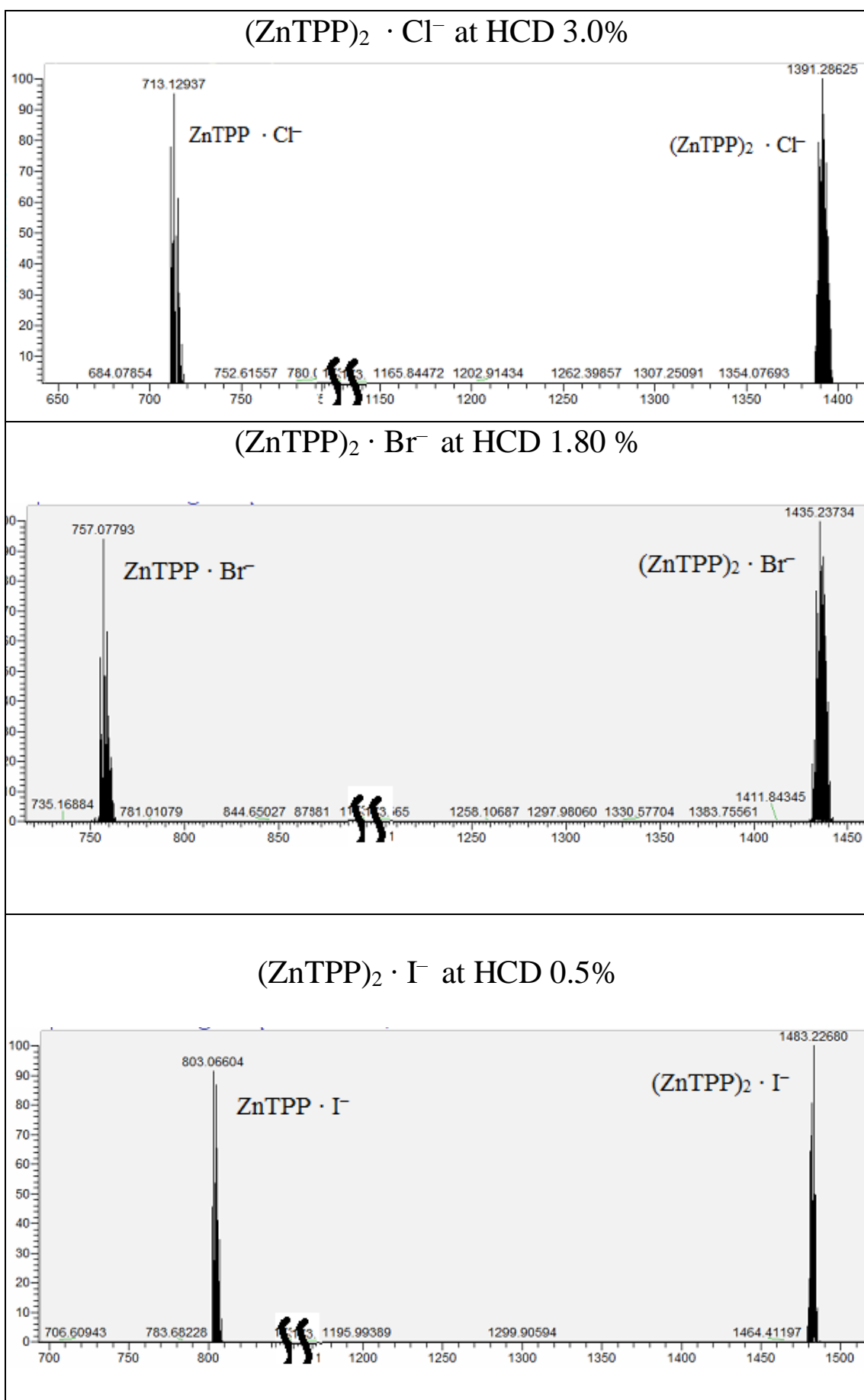


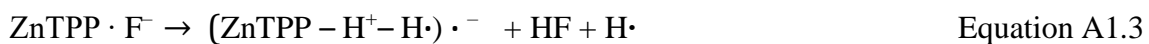
Fig A1.3 MS spectra of (ZnTPP)₂ · X⁻ complexes when HCD is applied.

A1.4 HCD of the ZnTPP · F⁻ complex

Since the lowest mass threshold for the HCD is 50 m/z it was not possible to observe the fluoride ion as a fragment when HCD is applied on ZnTPP · F⁻.

Compared to the other ZnTPP · X⁻ (X = Cl, Br, I) complexes, the fluorine 1:1 complex follows more distinctive mechanisms when HCD is applied.

The fragmentation channels that can be derived from the mass spectrum are:



These observed species are shown in Fig A1.4 below:

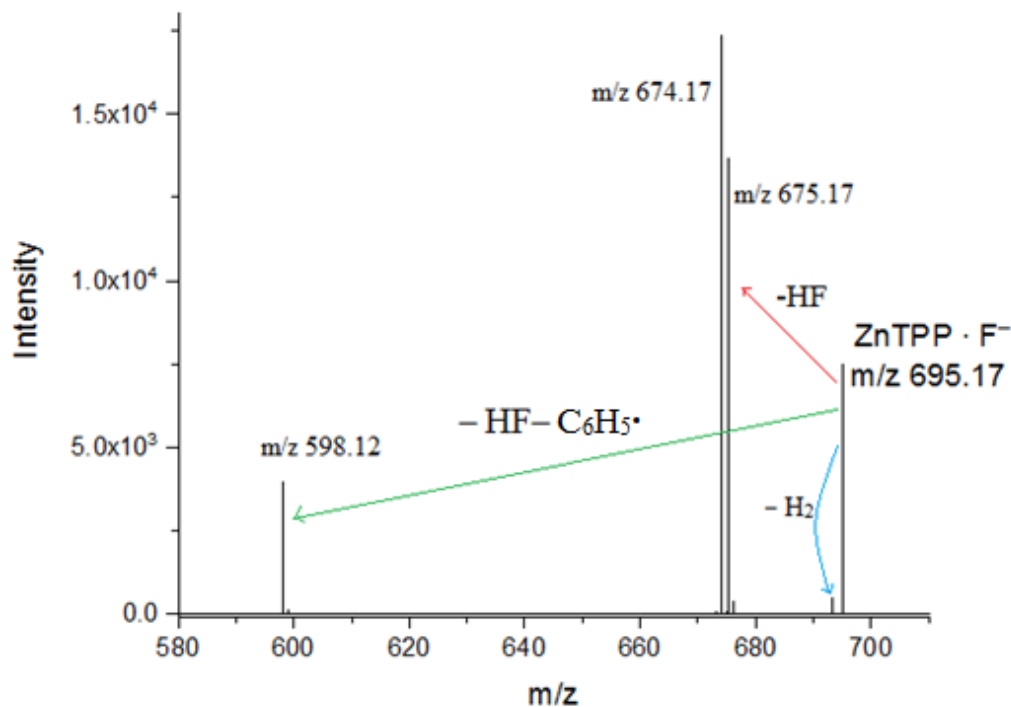


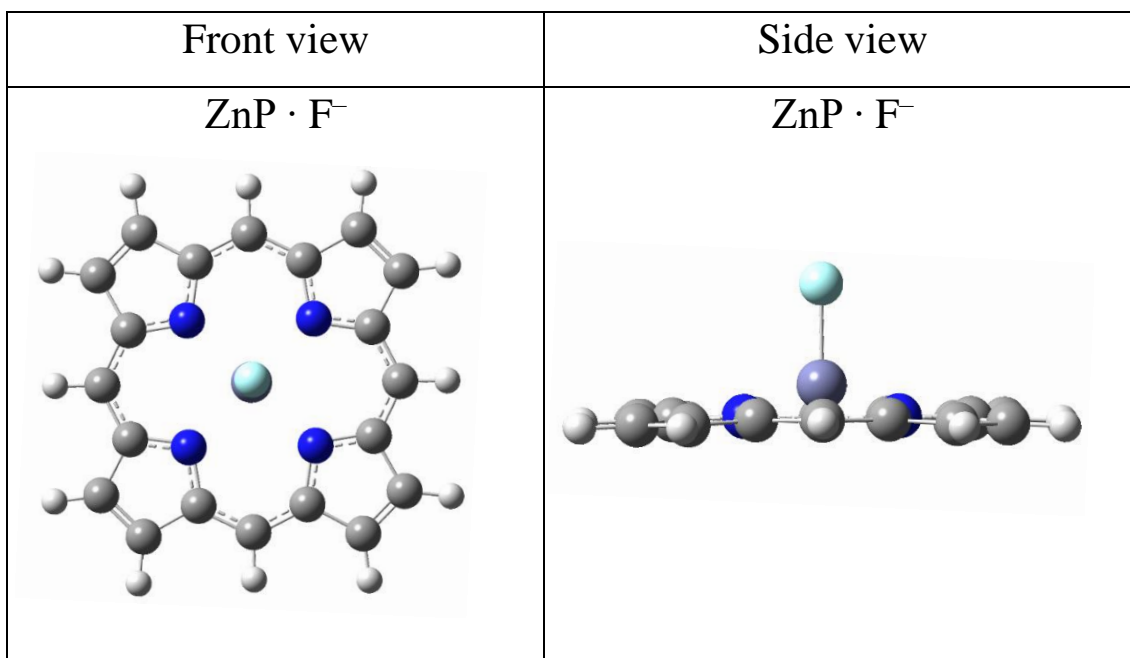
Figure A1.4 MS spectra of the ZnTPP · F⁻ complex at HCD 36%.

A1.5 DFT optimised geometries for $\text{ZnP} \cdot \text{X}^-$, $(\text{ZnP})_2 \cdot \text{X}^-$ and $(\text{ZnP})_2$

The DFT optimized structures are optimized using the methods described in Section 3.2. In Fig. A1.4 the front and side view of the DFT optimized $\text{ZnP} \cdot \text{X}^-$ complexes (1:1) is displayed; all of them are axially ligated and the Zn atom is displaced out of the porphyrin plane.

In Fig. A1.5 the front and side view of the DFT optimized $(\text{ZnP})_2 \cdot \text{X}^-$ complexes (2:1) is displayed; the two ZnP molecules are tilted due to the contribution of dispersive interaction between the two porphyrins.

In Fig. A1.6 the aggregate between two ZnP is displayed; the Zinc atom of each porphyrin is above the Nitrogen atom of the other porphyrin forming an 86° bond angle.



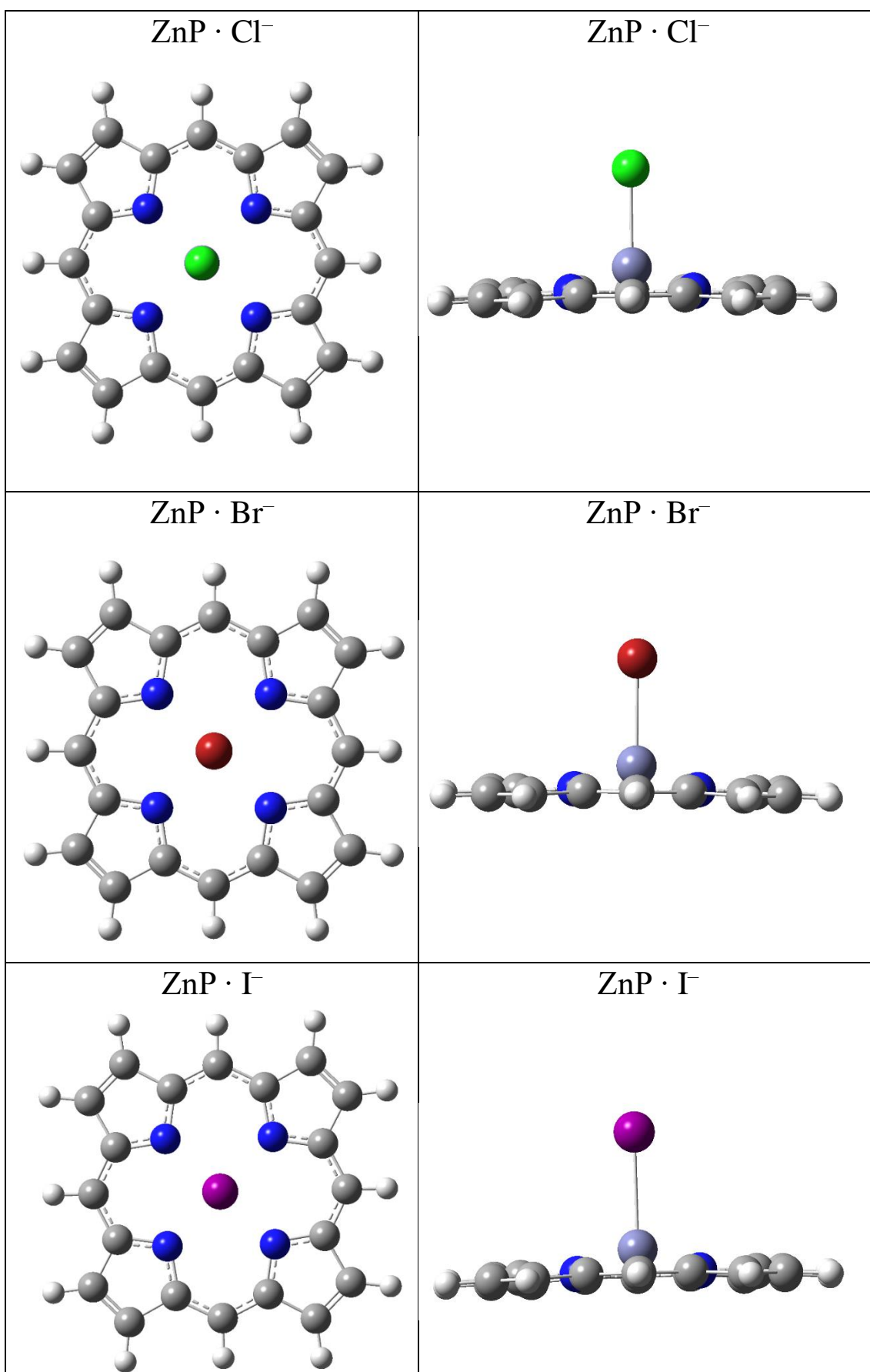
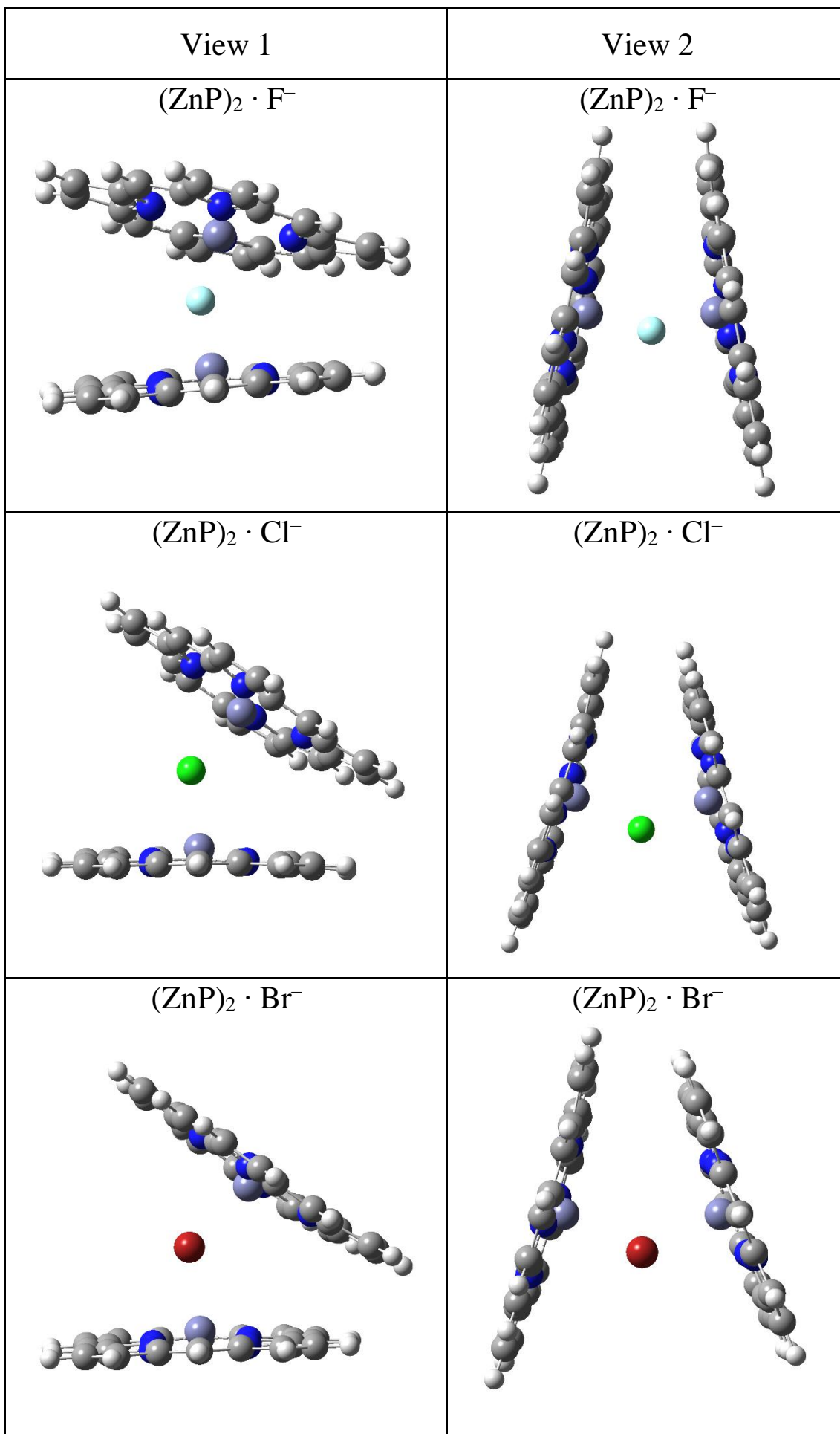


Figure A1.5 Front and side view of the DFT optimized structure of $\text{ZnP} \cdot \text{X}^-$ complexes.



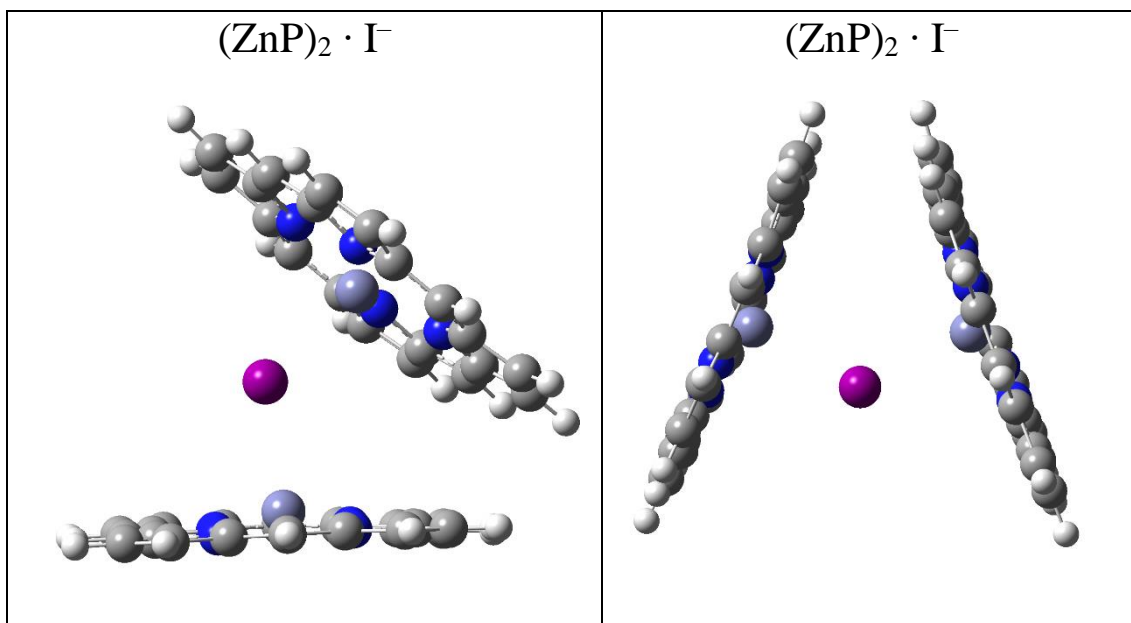


Figure A1.6 Front and side view of the DFT optimized structure of $(\text{ZnP})_2 \cdot \text{X}^-$ complexes.

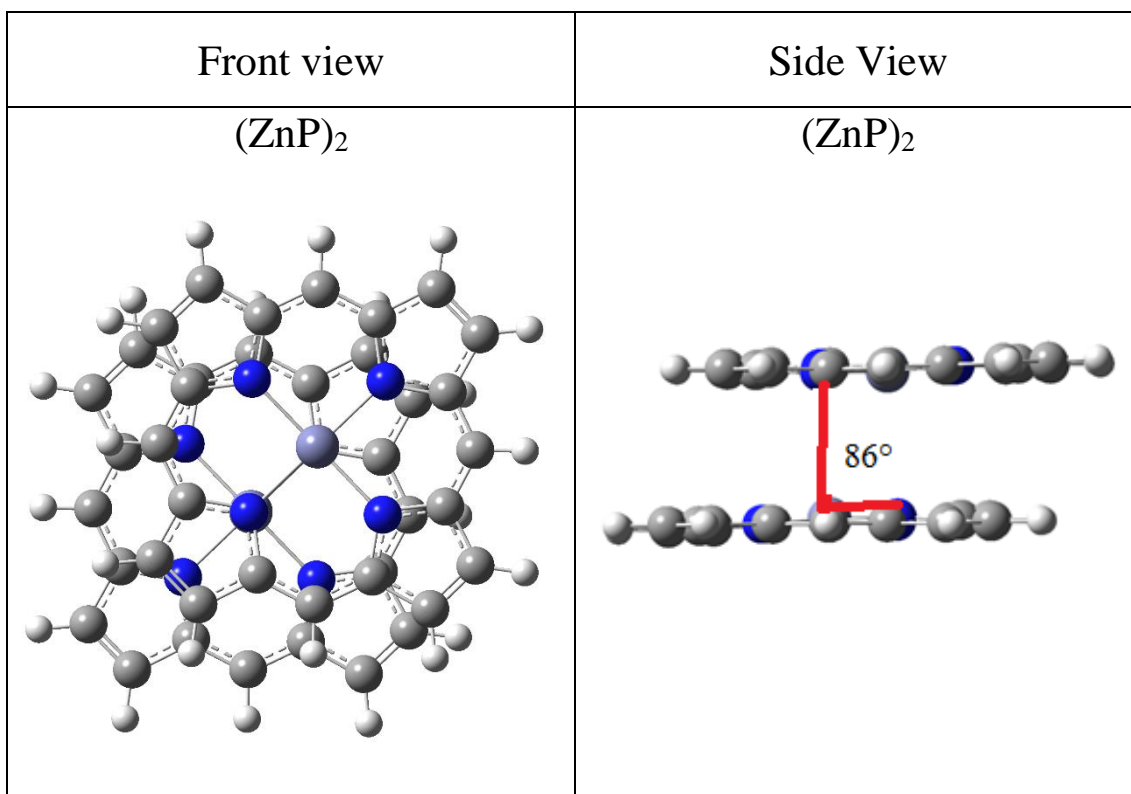


Figure A1.7 Front and side view of the DFT optimized structure of $(\text{ZnP})_2$ aggregates.

A1.6 Iodide and bromide photodepletion spectra

The PD spectra of iodide and bromide ions were measured in a laser interfaced mass spectrometer (AmaZon mass spectrometer). The curve that describes the PD spectra in case of simple monoatomic anion should show two onsets that begin promptly at the threshold energies corresponding to production of a free electron and a halide atom in the ground and excited states followed by plateau regions (Fig. A1.8); the shapes of these two onsets follow the ‘Wigner’ threshold law.¹¹⁸ When the energy of the photon is equal to the ionization energy of the anion X^- the photodetachment process can occur and one electron is ejected from the anion generating the first onset (Equation A1.1):



In the case of the bromide anion, its reported ionization energy is 3.36 eV¹¹⁹ and this is in accordance with the onset of the PD curve (Fig. A1. 9-a), however, the plateau is less defined and the signal to noise ratio is low; because no fragments can be produced by simple halide anions the only contribution to the photodepletion yield is photodetachment and together with the small cross-section, make those measurements difficult.

The iodide absorption profile (Fig. A1.9-b) appears plateauing more gradually and the second onset at 4.00 eV (Fig. A1.8) is not clearly identifiable. In the case of iodide, the onset of photodepletion appears to be at around 3.0 eV consistent with the reported iodine electron affinity of 3.06 eV.¹¹⁹

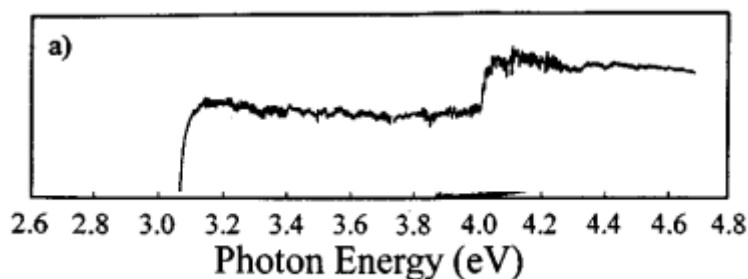


Figure A1.8 Photodetachment spectra of the bare I^- ion. Adapted from Ref.118

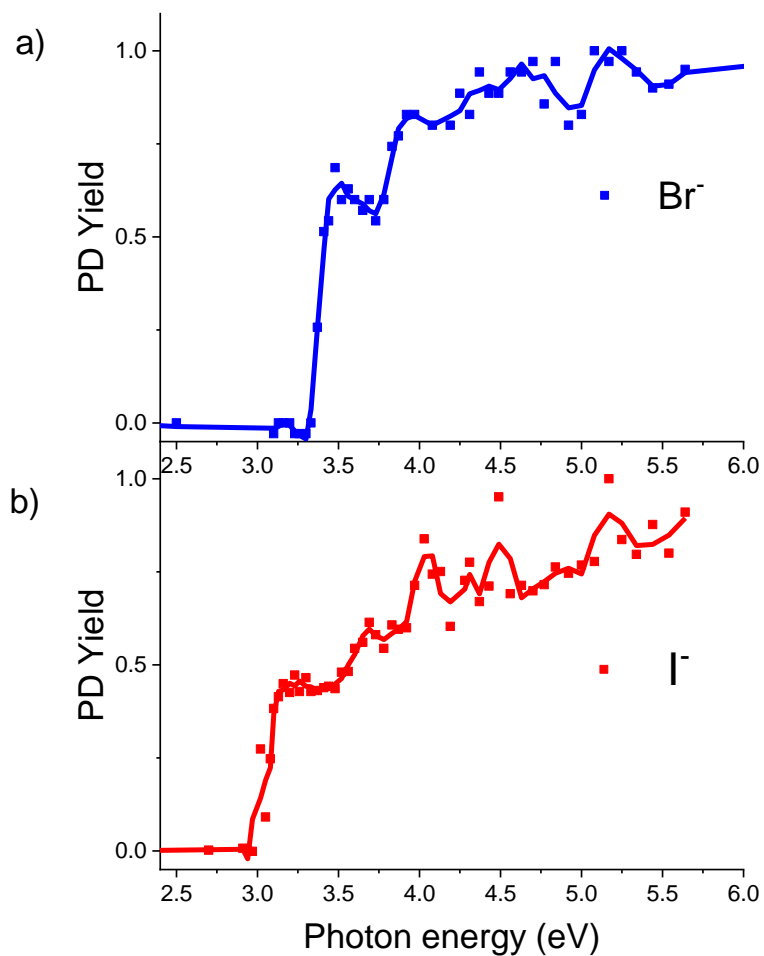


Figure A1.9 a) and b) Gas-phase UV absorption (photodepletion) spectra of bromide and iodide respectively. The solid line is a five-point adjacent average of the data points. The laser pulse energy was set at 0.30 ± 0.10 mJ for both the anions.

Appendix A2

A2.1 Introduction on the software developed to analyze the data

As part of this project, two Python computer programs were developed to automatically generate a table that can be used to plot directly the PD and PF spectra and a table used to generate the CID plots (relative intensity vs. CID voltage), respectively. Firstly, the commercial Bruker Compass DataAnalysis AutomationEngine software was used to extract the tables with all the data from the mass spectra that included m/z and intensities of the peaks in .ascii files (following a similar approach to a previous similar template). Then, the Python scripts were developed to analyze these extracted data and generate the PD and PF spectra or the CID plots.

This appendix will start with the PD and PF spectra generation (first Python program).

A2.2 Collection of the mass spectra

All the mass spectra are processed through Bruker Compass DataAnalysis (provided by the manufacturer of the mass spectrometer) and each data set was saved automatically with a numeric index inside the project folder:

“\\path\Project_Folder \date_molecule _0000.d”

“\\path\Project_Folder \date_molecule _0001.d”

“\\path\Project_Folder \date_molecule _0002.d”

etc.

Each of these data sets contains all the mass spectra collected with both the laser turned off and turned on at a specific wavelength and with a chosen data collection time of usually one minute; for example, “date_molecule _0000.d” contains the spectra collected at 402.0 nm, “date_molecule _0001.d” at 406 nm and “date_molecule _0002.d” at 410

nm.

During the experiment, in the same project folder, a text file (“info.txt”) is generated, that contains the current wavelength (nm), laser pulse energy (mJ), stability of the laser output (%), attenuation value, and the corresponding numeric index of the data set; for example if the laser pulse energy chosen is $0.30 \pm 15\%$ mJ, then the “info.txt” text file will look similar to this:

```
nm    mJ    %    at. index
402.0 0.286 10.19 19 0
406.0 0.307 9.72 35 1
410.0 0.285 10.94 46 2
etc.
```

The control of the laser pulse energy, attenuation, and generation of this latter text file is a merit of Dr. Jacob Berembein. This text file will be used by the Python scripts.

A2.3 DataAnalysis AutomationEngine: First step

Once the data acquisition from the laser interfaced mass spectrometer is finished, the indexed data sets (“eg. date_molecule _0000.d”) are used by the commercial software DataAnalysis AutomationEngine (Visual basic programming language); the script presented was written in DataAnalysis AutomationEngine and was adapted and modified from a previous template already available in this research group. Firstly, it starts with the data set “date_molecule _0000.d” and it averages all the mass spectra corresponding to the laser off and then to the laser on, generating two averaged spectra. Secondly, it identifies all the peaks in both the averaged spectra and generates two .ascii files (0000OFF.ascii and 0000ON.ascii) that contain the peaks m/z values together with their respective intensity. The software, then, repeat this same procedure with “date_molecule _0001.d”, “date_molecule _0002.d” etc. generating 0001OFF.ascii, 0001ON.ascii, 0002OFF.ascii, 0002ON.ascii etc.

All these .ascii files are automatically stored in a folder that the user chooses.

The script that does all the steps described above was written in the AutomationEngine interface and is copied below. The user has to change only the path where the data sets are stored and choose a path for the output folder that will contain the .ascii files (the user changes only the green parts of this script).

option explicit

'Dim to define variables

Dim Application

Dim Analysis

Dim int,count

Dim a,b,c,f,h,i,j

Dim pathOUT, pathON, pathOFF

' opens DataAnalysis

set Application = GetObject("", "BDal.DataAnalysis.Application")

'The user has to add the path where all the data sets are stored but removing the index as in the example below:

a = "\\path\Project_Folder \date_molecule _"

'The user has to add the path where they want to store the output .ascii files:

pathOUT = "\\path\output_asciiFiles_molecule\"

'create folder called "output_asciiFiles_molecule" using the path defined by the user(pathOUT)

Set f = CreateObject("Scripting.FileSystemObject")

f.CreateFolder(pathOUT)

b = ".d\Analysis.yep"

' The index used to label the data sets are made of four digits eg.0000, 0001, etc. and the

variable h is used to add the zeros on the left"

`h = "000"`

' if you have 10 data sets, this loop is performed 10 times, if you have 30 data sets then it will be performed 30 times, etc. up to 110 data sets. If you have more than 110 data sets increase this number below:

`For count = 0 To 110`

`i = h & count ' 0 becomes 0000, 2 becomes 0002, 32 become 00032, etc.`

"keeps only the last four numbers from i, i.e. 0002 is the same, 00028 becomes 0028, etc so that it matches up with the filename

`j = Right(i, 4)`

'combines a, j and b to provide the full root directory to the file of the data set whose index is defined by variable count. i.e. if we are at the 3rd loop than count is equal to 2 and therefore AutomationEngine orders to open the data set with the index 0002.

`c = a & j & b`

`set Analysis = Application.Analyses.Open(c)`

"loads the peak finding algorithm, noise cut off, etc. methods defined by the user in MethodEditor(provided by DataAnalysis). The user has to change this adding their path where their method file is stored. Once this method is optimized it is rarely changed, therefore, this section is not changed only if needed.

`Analysis.LoadMethod "\\path\DataExtractionScript.m"`

`'Analysis.RecalculateLineSpectra 'OPTIONAL, use only if you prefer to use line spectra MS instead of profile spectra`

'DataAnalysisfunctionality to separate the different MRM chromatograms

`Analysis.FindMSn`

`Analysis.Compounds.DisableAll 'Unchecks all of the produced compound spectra`

`Analysis.Chromatograms(2).AverageMassSpectrum true, false 'Averages the first MRM spectrum - which MUST be Laser ON`

`Analysis.Chromatograms(3).AverageMassSpectrum true, false 'Averages the first MRM spectrum - which MUST be Laser OFF`

`pathON = pathOUT & j & "ON"`

`pathOFF = pathOUT & j & "OFF"`

Analysis.Spectra(1).ExportMassList pathON, daASCII 'exports the mass list of the ON spectrum as an ascii file. i.e. 0000on.ascii, 0025on.ascii

Analysis.Spectra(2).ExportMassList pathOFF, daASCII 'exports the mass list of the OFF spectrum as an ascii file. i.e. 0000off.ascii, 0025off.ascii

Next

Analysis.Save ' Saves the analysis if you need to look at it later

Summary output:

At end of this AutomationEngine process a new folder will be created that contains these files:

0000OFF.ascii

0000ON.ascii

0001OFF.ascii

0001ON.ascii

0002OFF.ascii

0002ON.asciii

Etc.

Each of these .ascii files contains the mass peak list and their corresponding intensity i.e. "0002OFF.ascii" will contain all the m/z value and intensities of the peaks found on the averaged laser off spectrum (this spectrum is obtained averaging all the laser off spectra recorded on the data set with index 0002 ("date_molecule _0002.d")). Similarly, "0002ON.ascii" will contain all the m/z values and intensities of the peaks found on the averaged laser on spectrum.

Example of the content of one of these .ascii files (the second and third columns are the m/z and respective intensity of the detected peak)

#	m/z	Intensity
1	124.65	2
2	125.20	25

3 125.56 29
4 125.90 192
5 126.20 385
6 126.88 1136126
7 127.32 6976
8 127.57 1514
9 127.83 780
10 128.15 617
11 128.46 243
12 128.74 37
etc.

A2.4 Phyton scripts: Second step

Once the output .ascii files are generated and saved by AutomationEngine in the user-defined output folder, the user can start with the analysis of these collected experimental data using the scripts developed in this project.

A folder named “DataAnalysisSoftwares(DA 4.2 Phyton 3.8)” was created and inside this folder, the following Phyton scripts are stored:

ClickME.py

FindFragments.py

Info.py

Input.py

LaserAllFragments.py

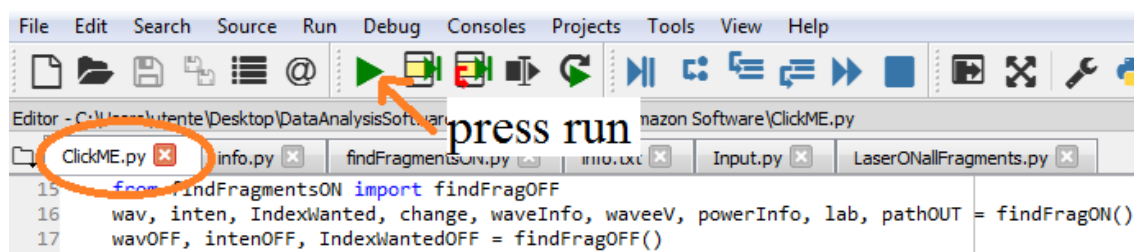
Importantly, the user has to copy and paste the “info.txt” file containing all the instrumental parameters (wavelengths, laser pulse energy, etc.) described in Section A2.2 from their project folder to the “DataAnalysisSoftwares(DA 4.2 Phyton 3.8)” folder. This is fundamental because those parameters are needed to calculate the PD and PF spectra. The following step is to double click the “ClickMe.py” file and follow the commands on the terminal. Another option is to download the Phyton Spyder interface and drag and drop all the scripts into it (this has to be done only once) and run the “ClickMe.py” script;

this latter approach is recommended because it displays all the errors and the scripts can be modified directly on this interface if needed.

Once ClickMe.py is running, the user has only to follow the instructions from this software and the final output table is generated inside the “DataAnalysisSoftwares(DA 4.2 Python 3.8)” folder. The user can copy and paste this to Excel or Origin and directly plot the PD or PF spectra.

Below a figured assisted guide of what the user has to do (Spyder interface):

1) Make sure ClickMe.py is selected and click run



2) The user is asked to write or copy and paste the path where their output .ascii files were saved in the first step using AutomationEngine. After pressing enter a new question is asked to the user: “do you want everything that differs less than 0.15 m/z the same species?”: all the laser on .ascii files of all the data sets are read by the software and the number of peaks with the same m/z value in the whole sets are counted; the peaks relative to the same ion species have often slightly different values (i.e. m/z 139.86, 139.89, 139.84, 139.91, 139.81, 139.83, etc.) and if the user leaves the default 0.15 m/z, that means that if two peaks differ of less than 0.15 m/z then they are considered the same ion by the software and counted (i.e. average m/z 139.86 with 6 counts).

At this step, the user sees all the signals detected with the laser on and the number of times they are present in all the data sets. This is displayed in columns as “an index, average m/z of the peak relative to the same ion species and counts”:

```
Console 2/A x
Enter the pathOUT you used in Data Analysis:
path\output_asciiFiles_molecule\
LASER ON

Do you want to consider everthing that differs less than 0.15m/z the same specie?

if you want to change this default write 0, if not write an other number: 2
0 139.86 6
1 139.56 7
3 139.31 5
```

3) The user takes notes of the corresponding index of the ions they are interested i.e. 3 if they want the ion at m/z 139.31 in the example above. The user then writes all these indexes when asked to do so; the index corresponding to the parent ion must be the first one and the following indexes corresponding to the fragments can be written in any order.

```
index m/z counts
Now that you know your fragments tell me which ones you want
PS the parent ion must be the first you choose

write the correspondant numbers(eg.0 4 6 13) with a space in between: 3 12 41
```

4) Then the user is asked to change or keep the default 0.15 m/z and follow the previous steps but this time for the laser off data; because those data are collected with the laser off, no photofragments are produced and only the parent ion index is asked.

5) Now the program finishes (“press any key to exit”) and the output table called finalTableIntensity.txt is generated automatically into the “DataAnalysisSoftwares(DA 4.2, python 3.8)\Amazon Software\OUTPUTfiles” folder (this folder is generated automatically as well).

6) The user can use this table to directly plot PD and PF spectra.

A2.5 Phyton original scripts used for the PD and PF spectra calculation

In this Section, the Phyton scripts used to do all the analysis of the experimental .ascii files, as described in Section A2.4, are reported. They consist of five module scripts that are imported in a chain sequence (command import); ClickMe.py imports the findFragON and findFragOFF functions that are part of the findFragments.py module; findFragments.py imports the textTableON function that is part of the LaserAllFragments.py module; LaserAllFragments.py imports the module info.py; And info.py imports the module Input.py.

The “Input.py” script automatically creates a folder called “OUTPUTfiles” in the current directory that contains all the five scripts. In addition, in this module the function Input is defined; this function is responsible for asking the user to type the path that they used in Data Analysis where the .ascii files are stored and creating a new text variable called pathASCII where this path is stored.

The “info.py” script imports the module “Input.py” and recalls the function Input to get the current folder path (pathCWD), the path of the “OUTPUTfiles” folder (pathOUT), and pathASCII. It then reads the “info.txt” file stored in the current folder and memorizes its data in arrays: the array “waveInfo” stores the wavelengths used for each data set while “powerInfo” contains the laser pulse energies.

The “LaserAllFragments.py” script imports the module “info.py” and recalls the function info to get the paths and the number of data sets (variable lengthInfo). It then defines the functions textTableON and textTableOFF; these functions are used to read the .ascii files and generate and save in the “OUTPUTfiles” folder, respectively, a text file called allFragmentsON.txt and allFragmentsOFF.txt that contain the data set index, corresponding wavelength (nm), photon energy (eV), laser pulse energy (mJ), m/z signal and intensity of the mass spectra peak of the laser ON and OFF .ascii files. Below an example of an allfragmentsOFF.txt file is shown (in this case 30 data sets corresponding to 30 wavelenght probed were used):

Index	nm	eV	mJ	#	m/z	intensity
0000	400.0	3.1	0.31	1	72.48	4
0000	400.0	3.1	0.31	2	72.75	1
0000	400.0	3.1	0.31	3	74.01	1
....						
0001	396.0	3.13	0.293	1	72.58	6
0001	396.0	3.13	0.293	2	73.05	4
0001	396.0	3.13	0.293	3	76.01	20
....						
....						
0030	280.0	4.43	0.3	1	74.24	8
0030	280.0	4.43	0.3	2	75.52	3
0030	280.0	4.43	0.3	3	76.02	35
0030	280.0	4.43	0.3	4	77.50	1500

The “findFragments.py” imports the functions textTableON and textTableOFF from the module “LaserAllFragments.py”. Calling those functions, this script receives all the arrays with the data from the laser ON and OFF respectively and specifically, using the array “m” that contains all the m/z signals, it counts the number of ions that have the same m/z and produces two outputs lists (laser On and laser Off) on the user interface that saves also in the “OUTPUTfile” folder. The first column of this list is a crescent numerical index, the second column the averaged m/z value of the signal relative to the same species/noise and the third column represents the counts. An example of this table is below:

	m/z	counts
0	89.89	42
1	89.73	20
2	89.58	10
3	89.42	2
...		
16	80.97	45
17	80.52	16
18	80.37	29

The user then can choose from this list the masses that they are interested in and take note of the corresponding indexes (first column). This “findFragments.py” scripts also is responsible for asking the user the indexes of interest and store them.

The final step is done by the “ClickME.py” script. This script imports the two functions findFragON and findFragOFF from the “findFragments.py” module and using the indexes chosen by the user and the data in the arrays produces and saves a text table called “finalTableIntensity.txt” in the “OUTPUTfiles” folder. This table contains columns representing in order: the wavelength of each set of data (nm), the corresponding photon energy (eV), the intensity of the mass spectra signal of parent ion with laser off, the intensity of the mass spectra signal of the parent ion with laser on and the intensity of the mass spectra signal of the fragments chosen by the user. An example of this table is below:

wavel	eV	lasPow	parOFF	676.04	674.05	673.01	672.06	Depl
390	3.18	0.047	281086	186602	8047	424	409	0.022350391
388	3.2	0.051	247717	200949	540	74	72	0.010573874
386	3.21	0.049	251834	211841	764	xxxx	xxxx	0.009143182
384	3.23	0.051	277157	228474	2467	257	xxxx	0.009863241
382	3.25	0.056	275422	228818	2834	71	82	0.008665741
380	3.26	0.054	263834	214827	3130	78	71	0.010013989

In the above output table, parOFF represents the intensity of the mass spectrum signal of the parent ion with laser off, 676.04 is the m/z value of the parent ion and this fifth column represents the intensity of the parent ion with laser on. These two intensities together with the wavelength (wavel) and laser pulse energy (lasPow) are used to calculate the photodepletion (Depl). The remaining columns represent the intensities of the fragments and are labeled with their m/z values (674.05, 673.01, 672.06). With excel the user uses those values to calculate the PF according to Equation 2.2 (Chapter 2). The PF yield is not automatically calculated like the PD one, because DataAnalysis AutomationEngine sometimes detects the same peak twice (irregular shape) and the entire row in the “finalTableIntensity.txt” is shifted, however the user easily can detect the rows involved and manually modify them. The Phyton software here developed, can be improved to recognize this automatically.

Below all the scripts described in this section are copied:

Input.py

```
# -*- coding: utf-8 -*-
"""
Created on Sun Mar 10 13:25:43 2019
This asks the users about where to find the output .ascii files from
AutomationEngine and creates a directory called OUTPUTfiles where all
the generated output from the Phyton scripts will be stored in form of
text files.
@author: Chris xhindoli furlan
"""

#GENERATE "OUTPUTfiles" folder inside current directory
#finds current working directory and creates folder with all the
output .txt files that will be generated from this Phyton software.
import os
pathCWD = os.getcwd()

pathOUT = pathCWD + "\\OUTPUTfiles\\"

try:
    # Create target Directory
    os.mkdir(pathOUT)
except OSError:
    print ("Creation of the directory %s failed" % pathOUT)
else:
    print ("Successfully created the directory %s " % pathOUT)

def Input():
    #the only path we need is the one with all the laser ON and OFF .ascii
    files. Asks the user this path.
    pathASCIItmp = input("Enter the pathOUT you used in
DataAnalysis:\n")
    pathASCII = pathASCIItmp + "/"

    return pathASCII, pathCWD, pathOUT
```

info.py

```
# -*- coding: utf-8 -*-
"""
This recalls Input.py module and imports the useful paths. It reads
all the data from the "info.txt" file that was generated during the
experimental data collection and copied and pasted in the current
software directory. All the experimental settings in the "info.txt"
are stored in arrays when this "info.py" script runs.
@author: Chris Xhindoli Furlan
"""
import Input

pathASCII, pathCWD, pathOUT = Input.Input() #this import paths

def info():

    pathTemp = pathCWD + "\\info.txt" #full path with file
    name(info.txt) is in current working directory
    fileTemp = open(pathTemp, "r") #only read file

    lines = fileTemp.readlines() #read all the lines of info.txt
    waveInfo = [] #stores wavelenght nm used(from info.txt)
    waveeV = [] #transform wavelenght in energy eV
    powerInfo = [] #stores laser power(from info.txt)

    for i in range(len(lines)):
        line = lines[i] #line store the "i" row
        inp = line.split() #detect spaces and divide terms in line
        waveInfo.append(float(inp[0]))
        energy = round(1239.84193/float(inp[0]),2)
        waveeV.append(energy)
        powerInfo.append(float(inp[1]))

    return waveInfo, waveeV, powerInfo, len(lines), pathASCII, pathOUT
```

laserAllFragments.py

```
# -*- coding: utf-8 -*-
"""
Created on Sat Mar  9 13:32:13 2019
Since DataAnalysis AutomationEngine can only export data as ASCII
format then Phyton has problems interpreting them. Whith this script
all the data are imported from the ASCII files and written to a
userfriendly text file. In addition the data are stored in 5 arrays.
For e.g the data from an hypothetical file named 0001ON.ASCII are
stored as following:
x[1]="0001", y[1]=400(wavelength nm), z[1]=0.32(eV), w[1]=720.12(m/z),
h[1]=11779(intensity)
and a txt file called laserONallFragments.txt is generated with all
the information. Same procedure repeated with laser off data.
@author: Chris Xhindoli Furlan
"""

# define a useful subroutine, global variables

#we need the wavelengh and the laser energy from the "info.txt" so
recall info.py
import info
waveInfo, waveeV, powerInfo, lenghtInfo, pathASCII, pathOUT =
info.info() #recals info function

#this is the name of the function to store all the laser ON data in
arrays
def textTableON():

    pathTemp = pathOUT + "allFragmentsON.txt"
    #opens the just created laserONallFragments.txt file to write on it.
    fileTemp = open(pathTemp, "w+")

    #GENERATE THE NAMES OF THE .ascii FILES GENERATED BY DATAANALYSIS
    AUTOMATIONENGINE SCRIPT
    #define the name of the files eg 0012ON.ASCII. here we are only
    interested in ON files
    for i in range(lenghtInfo):
        if i < 10:
            a = "000"
        elif i < 100:
            a = "00"
        else:
            a ="0"
        bON = a + str(i) + "ON" #this write eg.0003ON, 0016ON, 0128ON
        pathON = pathASCII + bON + ".ASCII"
        #this open the files with laser ON eg.parh....\\0012ON.ASCII

        #here reads files generated by dataanalysis
        fileON = open(pathON, 'r')
        lines = fileON.readlines()
        del lines[0] #delete first line of the table

    fileON.close()
```

```

newLines = []

#writes the userfriendly text file
for j in range(len(lines)):
    newLines.append(a + str(i) + " " + str(waveInfo[i]) + " " +
str(waveeV[i]) + " " + str(powerInfo[i]) + " " + lines[j])

    for j in range(len(lines)): #or you can use len(newLines)
since it's the same
        row = newLines[j]
        #now we can write those data in a temporary txt file to sort
out the difficulties experienced with the ASCII format
        fileTemp.write("%s" % row)

#open the same file but this time reading (r)
fileTemp = open(pathTemp, "r")
#read line into array
lines = fileTemp.readlines()

x = [] #number file
y = [] #energy eV
z = [] #wavelength
w = [] #laser power
h = [] #m/z
k = [] #intensity

for i in range(len(lines)):
    splitLines = lines[i].split() #eg. lines[1]= "23 67 6" -->
splitLines= "23", "67", "6"

    x.append( str(splitLines[0]) ) #this array has file number
    y.append( float(splitLines[1]) ) #this array has wavelength
    z.append( float(splitLines[2]) ) #energy
    w.append( float(splitLines[3]) ) #laserpower
    h.append( float(splitLines[5]) ) #m/z
    k.append( int(splitLines[6])) #intensity

    #now that we imported all the data in the arrays we can make the
text file even more user friendly adding a legend

fileTemp = open(pathTemp, "a")
fileTemp.seek(0,0)
fileTemp.write("file wavlgh eV laserP m/z int FWHW \n\n")

fileTemp.close()

return x, y, z, w, h, k, waveInfo, waveeV, powerInfo, pathOUT

```

```

"""
the same but with LASER OFF
"""

def textTableOFF(): #this is the name of the function to store all the
laser OFF data in arrays

    pathTemp = pathOUT + "allFragmentsOFF.txt"
    fileTemp = open(pathTemp, "w+") #open the
laserOFFallFragments.txt file to write on it

    #GENERATE THE NAMES OF THE .ascii FILES GENERATED BY DATAANALYSIS
AUTOMATION ENGINE SCRIPT
    #define the name of the files eg 0012OFF.ASCII. here we are only
interested in OFF files
    for i in range(lenghtInfo):
        if i < 10:
            a = "000"
        elif i < 100:
            a = "00"
        else:
            a = "0"
        bOFF = a + str(i) + "OFF" #this write eg.0003OFF, 0016OFF,
0128OFF
        pathOFF = pathASCII + bOFF + ".ASCII"
        #this open the files with laser OFF eg.parh....\\0012OFF.ASCII

        fileOFF = open(pathOFF, 'r') #here reads files generated by
dataanalysis
        lines = fileOFF.readlines()
        del lines[0] #delete first line of the table

        fileOFF.close()

        newLines = []

        #writes the userfriendly text file
        for j in range(len(lines)):
            newLines.append(a + str(i) + " " + str(waveInfo[i]) + " " +
str(waveV[i]) + " " + str(powerInfo[i]) + " " + lines[j])

        for j in range(len(lines)): #or len(newLines) since it's the
same
            row = newLines[j]
            #now we can write those data in a temporary txt file sorting
out the
            #the difficulties experienced with the ASCII format
            fileTemp.write("%s" % row)

        fileTemp = open(pathTemp, "r") #open the same file but this
time reading (r)
        #read line into array
        lines = fileTemp.readlines()

        x = [] #number file

```



```

y = [] #energy eV
z = [] #wavelength
w = [] #laser power
h = [] #m/z
k = [] #intensity

for i in range(len(lines)):
    splitLines = lines[i].split() #eg. lines[1]= "23 67 6" -->
splitLines= "23", "67", "6"

    x.append( str(splitLines[0]) ) #this array has file number
    y.append( float(splitLines[1]) ) #this array has wavelength
    z.append( float(splitLines[2]) ) #energy
    w.append( float(splitLines[3]) ) #laserpower
    h.append( float(splitLines[5]) ) #m/z
    k.append( int(splitLines[6])) #intensity

    #now that we imported all the data in the arrays we can make the
text file
    #even more user friendly

    fileTemp = open(pathTemp, "a")
    fileTemp.seek(0,0)
    fileTemp.write("file wavlgh eV laserP m/z int FWHW \n\n")
    fileTemp.close()

return x, y, z, w, h, k, waveInfo, waveeV, powerInfo, pathOUT

```

findFragments.py

```
# -*- coding: utf-8 -*-
"""
Created on Sun Mar 10 17:20:07 2019
This program uses the textTable function defined in
LaserAllFragments.py to write in the MyFragments.txt file all the
fragments and their abundance
@author: Chris Xhindoli Furlan
"""

def findFragON():

    from LaserAllFragments import textTableON #I will use the
    textTableON function later

    IdFile, wav, en, laserP, m, inten, waveInfo, waveeV, powerInfo,
    pathOUT = textTableON()

    fragPath = pathOUT + "FragmentsFoundON.txt" #where we create an
    output text file with all fragments
    fileFrag = open(fragPath, 'w+') #write and creates file(+)
    fileFrag.write("m/z counts\n")
    #now it finds all the fragments and counts them

    frame = 0.15 #by default everything that differs less than 0.5 m/z
    units is considered the same species.
    exclude = []

    print("LASER ON")
    print("\nDo you want to consider everthing that differs less than
    0.15m/z the same specie?")
    answer1 = int(input("if you want to change this default write 0,
    if not write an other number: "))
    if answer1 == 0:
        frame = float(input("write the new m/z difference to replace
    the default 0.15m/z: "))
        print("\nYour fragments with the laser on are:")

    m1 = sorted(m, reverse = True)

    massUser = []
    k_out=0

    for i in range(len(IdFile)):
        summ = m1[i]
        same = 1
        contin = 1
        #if is the same is excluded

        for k in range(len(exclude)):
            if i == exclude[k]:
                contin = 0 #false: we can not continue,this is a new
fragment
```

```

    if contin == 1:
        for j in range(i+1, len(IdFile)):
            if m1[j] - frame < m1[i] and m1[i] < m1[j] + frame:
                summ = summ + m1[j]
                same = same + 1
                exclude.append(j)
            mean = round(summ/same,2) #the mean of the fragment
found
            fileFrag.write(str(mean) + " " + str(same) + "\n")

            print(str(k_out)+" "+ str(mean) + " " + str(same))
            k_out = k_out + 1
            massUser.append(mean) #now we have correspondence index
with mass
            fileFrag.close()

            #now we have all the data in the txt file. #
            #I want to ask the user wich fragments wants and store these in a
new array

            print("\nindex m/z counts\n Now that you know your fragments tell
me which ones you want\nPS the parent ion must be the first you
choose")
            strFragUser = input("write the correspondant numbers(eg.0 4 6 13)
with a space in between: ")

            IndexWanted = []
            FragUser = [] #this is integer

            inp=strFragUser.split()

            for i in range(len(inp)):
                FragUser.append(int(inp[i]))

            #now we need a new array with the masses derived from massUser
            #if user choses eg.3 then they want massUser[3]

            change = [] #where we change fragment
            count = -1
            #when we choose numeber it corresponds to m[number] m/z value:
            for i in range(len(FragUser)):

                for j in range(len(IdFile)):
                    if m[j] - frame < massUser[FragUser[i]] and
massUser[FragUser[i]] < m[j] + frame: #fragment we want
                        #here it's ok, we may store index j to know wich
masses are to consider
                            IndexWanted.append(j)
                            #all we want is stored in IndexWanted
                            count = count + 1
                    change.append(count)

            #here we need to store the masses of the fragments for the label
in analysis
            label = []
            for i in range(len(FragUser)):
                label.append(massUser[FragUser[i]])

```

```

    return wav, inten, IndexWanted, change, waveInfo, waveeV,
powerInfo, label, pathOUT

```

```

"""
same with fragment OFF
"""

```

```

def findFragOFF():

```

```

    from LaserAllFragments import textTableOFF #I will use the
textTable function later

```

```

    IdFile, wav, en, laserP, m, inten, waveInfo, waveeV, powerInfo,
pathOUT = textTableOFF()

```

```

    fragPath = pathOUT + "FragmentsFoundOFF.txt" #where we create
file with all fragments
    fileFrag = open(fragPath, 'w+') #write and creates
file(+)
    fileFrag.write("m/z counts\n")
    #now it finds all the fragments and count them

```

```

    frame = 0.15 #by default everything that differs less than 0.5 m/z
units is considered the same specie
    exclude = []

```

```

    print("LASER OFF")
    print("\nDo you want to consider everthing that differs less than
0.15m/z the same specie?")
    answer1 = int(input("if you want to change this default write 0,
if not write an other number: "))
    if answer1 == 0:
        frame = float(input("write the new m/z difference to replace
the default 0.15m/z: "))
        print("\nYour fragments with the laser OFF are:")

```

```

    m1 = sorted(m, reverse = True)

```

```

    massUser = []
    k_out=0

```

```

    for i in range(len(IdFile)):
        summ = m1[i]
        same = 1
        contin = 1
        #if is the same is excluded

        for k in range(len(exclude)):
            if i == exclude[k]:
                contin = 0 #false: we can not continue,this is new
fragment

```

```

    if contin == 1:
        for j in range(i+1, len(IdFile)):

```

```

        if m1[j] - frame < m1[i] and m1[i] < m1[j] + frame:
            summ = summ + m1[j]
            same = same + 1
            exclude.append(j)
        mean = round(summ/same,2) #the mean of the fragment
found
        fileFrag.write(str(mean) + " " + str(same) + "\n")

        print(str(k_out)+" "+ str(mean) + " " + str(same))
        k_out = k_out + 1
        massUser.append(mean) #now we have correspondence index
with mass
    fileFrag.close()

    #now we have all the data in the txt file. #
    #I want to ask the user wich fragments wants and store these in a
new array

    print("\nNow that you know your fragments with laser OFF tell me
which one is your parent ion")
    strFragUser = input("write the correspondant number of the parent
ion(eg.3): ")

    IndexWanted = []

    parentIon = int(strFragUser) #here if parent ion is in 3rd
fragment shown then parentIon = 3

    #if user choses eg.3 then they want massUser[3]

    #when we choose numeber it corresponds to m[number] m/z value:

    for j in range(len(IdFile)):
        if m[j] - frame < massUser[parentIon] and massUser[parentIon]
< m[j] + frame: #fragment we want
            #here it's ok, we may store index j to know wich masses
are to consider
            IndexWanted.append(j)
            #all we want is stored in IndexWanted

    return wav, inten, IndexWanted

```

ClickME.py

```
# -*- coding: utf-8 -*-
"""
This is the final script. You have to double click this one or press
run when this one is selected on Spyder. All the other modules
previously described are used and loaded by this one. This script
recalls findFragments which uses LaserONallFragments
Author: Chris Xhindoli Furlan
"""

import math

#this is only laser On
def Analysis():

    from findFragments import findFragON
    from findFragments import findFragOFF
    wav, inten, IndexWanted, change, waveInfo, waveeV, powerInfo, lab,
pathOUT = findFragON()
    wavOFF, intenOFF, IndexWantedOFF = findFragOFF()

    #write .txt wavelengh, energy, intensityONparent,
intensityOFFparent, intensityfrag1, frag2
    outPath = pathOUT + "finalTableIntensity.txt"
    fileFinal = open(outPath, 'w+')
    line = []

    for i in range(len(waveInfo)):
        line.append(str(waveInfo[i])+" "+str(waveeV[i])+"
"+str(powerInfo[i]))

    numFrag = len(change)

    for i in range(len(line)):
        parentOFF=0
        parentON = 0
        fragON=0
        for k in range(len(IndexWantedOFF)):
            if wavOFF[IndexWantedOFF[k]] == waveInfo[i]:
                line[i] = line[i] + " " +
str(intenOFF[IndexWantedOFF[k]])
                iOFF = k
                parentOFF = 1

        if parentOFF == 0:
            line[i] = line[i] + " " + "xxxxx"#in this case none of the
parent ion with laser OFF is present at that wavelengh

        #laser On fragments(number of fragments is numFrag that is the
length of change)

        for k in range(change[0]+1):
            if wav[IndexWanted[k]] == waveInfo[i]:
                line[i] = line[i] + " " + str(inten[IndexWanted[k]])
```

```

        iON = k
        parentON = 1

    if parentON == 0:
        line[i] = line[i] + " " + "xxxx"

    sumFrag = 0 #for relative photodetachment
    for j in range(1, numFrag):
        fragON=0

        for k in range(change[j-1]+1, change[j]+1):
            if wav[IndexWanted[k]] == waveInfo[i]:
                line[i] = line[i] + " " +
str(inten[IndexWanted[k]])
                sumFrag = sumFrag + inten[IndexWanted[k]]
                fragON = 1

        if fragON == 0:
            line[i] = line[i] + " " + "xxxx"

        #analysis part
        if parentON == 1 and parentOFF == 1: #parent ion visible both
ON and OFF mode
            photoDepletion =
math.log((intenOFF[IndexWantedOFF[iOFF]]/inten[IndexWanted[iON]])/(wa
veInfo[i]*powerInfo[i]))
            diffParent=intenOFF[IndexWantedOFF[iOFF]]-
inten[IndexWanted[iON]]
            relPhotDetachmentPerc = 100*(1-sumFrag/diffParent)

            line[i] = line[i] + " " + str(round(photoDepletion,4)) + " "
+str(round(relPhotDetachmentPerc,1))
        else:
            line[i] = line[i] + " " + " xxxx" + " xxxx"

    fileFinal.write(line[i]+"\n")

    label = "wavel eV lasPow parOFF "
    for i in range(len(lab)):
        label = label + str(lab[i])+" "

    label = label + "Depl"+" %relPhotD"
    fileFinal.write(label)

    fileFinal.close()

    print("You program is finished!!!Check the
FinalTableIntensity.txt")
    k=input("press any key to exit ")

```

Analysis()

A2.6 CID plots scripts

To generate the CID plots the previously described AutomationEngine VB script and the Phyton modules were modified; in the CID experiments, usually, every fixed number of minutes the collision voltage increases of a step decided by the user and this defines ranges in the TIC of equal time length. In this case, the AutomationEngine script described in Section A2.3 was modified so that a text file was extracted for each range i.e. min1.txt, min2.txt...min18.txt. These text files are then used by the Phyton scripts to generate an output table where each row represents a range in the TIC and the columns represent the mass spectrum peak intensity of the ions with the m/z displayed on the legend.

	309.16	400.96	311.48
1min	85	6539230	36
2min	93	6016573	52
3min	41	5665652	83
4min	382	5674469	62
5min	51	5531550	xxxx

In the example above, the data from the first TIC range collected at a certain CID collision voltage (the user takes notes of collision voltages during the experiment) is displayed in the first row (1min) of the table; the second TIC range on the second row (2min) etc. In this example, the parent ion is at m/z 400.96 and the other ions (collision-induced fragments) selected by the user are at m/z 309.16 and m/z 311.48 (all these m/z values are shown on the legend) and their respective mass spectra intensities are displayed for each TIC range.

The user can use this table and directly calculate the relative intensities and plot the CID graph.

After running the new modified VB AutomationEngine the user double clicks on the “ClickME.py” script or uses Spyder as described in the previous Sections and follows the instructions that will be displayed.

Here only four Phyton modules are used: ClickME.py, findFragments.py, allFragments.py, Input.py.

AutomationEngine Script

```
'CHANGE THIS! time = 28 <--- change the second number to the time of
your CID(the end time of your last segment)
'NB if you are lazy just put a high number and then delete the extra
output segments later
'CHANGE THIS! segmentLenght = 1 <--- change this number to the lenght
of each segment. In this case it means each segment length is lmin
time = 2
segmentLenght = 0.5
For count = 0 To time Step segmentLenght
    x = count
    y = count + segmentLenght

    'Analysis.RecalculateLineSpectra 'use line spectra MS instead of
profile spectra, this is optional'
    Analysis.Compounds.DisableAll 'Unchecks all of the produced
compound spectra (which are not useful in our analysis)
    Analysis.Chromatograms(1).AddRangeSelection x, y, 0, 0
    Analysis.Chromatograms(1).AverageMassSpectrum true, false
    Analysis.Chromatograms(1).ClearRangeSelections

    Analysis.Save ' Saves the analysis if you need to look at it
later

Next

x= 0

num_seg = time/segmentLenght
For i = 0 To num_seg Step 1
    x = x + 1
    path = pathOUT & "min" & x
    Analysis.Spectra(x).ExportMassList path, daASCII 'exports the mass
list
Next
```

Input.py

```
# -*- coding: utf-8 -*-
"""
This asks the users about where to find the output .ascii files from
AutomationEngine and creates a directory called OUTPUTfiles where all
the generated output from the Phyton scripts will be stored in form of
text files.
"""

#ASK USER WHERE TO STORE ALL THE RESULTING TEXT FILES
#finds current working directory to write folder with all the output
.txt files
import os
pathCWD = os.getcwd()

pathOUT = pathCWD + "\\OUTPUTfiles\\"

try:
    # Create target Directory
    os.mkdir(pathOUT)
except OSError:
    print ("Creation of the directory %s failed" % pathOUT)
else:
    print ("Successfully created the directory %s " % pathOUT)

def Input():
    #the only path we need is the one with all the laser ON and OFF
files
    pathASCIItmp = input("Enter the pathOUT you used in Data
Analysis:\n")
    pathASCII = pathASCIItmp + "/"

    numIntervals = input("Enter number of intervals you have:\n")

    numIntervalsInt = int(numIntervals)

    return pathASCII, pathCWD, pathOUT, numIntervalsInt
```

allFragments.py

```
# -*- coding: utf-8 -*-
"""
Creates an output file called allFragments.txt where the range and the
m/z and corresponding intensities are stored
"""
# define a useful subroutine, global variables

import Input

pathASCII, pathCWD, pathOUT, numIntervals = Input.Input() #this import
path where info.txt is stored

def textTable(): #this is the name of the function to store all the
laser ON data in arrays

    pathTemp = pathOUT + "allFragments.txt"
    fileTemp = open(pathTemp, "w+") #open the
laserONallFragments.txt file to write on it, if not present crates
file

    #GENERATE THE NAMES OF THE FILES GENERATED BY DATAANALYSIS
AUTOMATION ENGINE SCRIPT
    #define the name of the files eg 0012ON.ASCII. here we are only
interested in ON files
    for i in range(1, numIntervals+1):

        bON = "min" + str(i) #this write eg.min1, min2, min3 etc.
        pathON = pathASCII + bON + ".ASCII"
        #this open the files with laser ON eg.parh....\\0012ON.ASCII

        fileON = open(pathON, 'r') #here reads files generated by
dataanalysis
        lines = fileON.readlines()
        del lines[0] #delete first line of the table

        fileON.close()

        newLines = []

        #writes the userfriendly text file
        for j in range(len(lines)):
            newLines.append("min" + str(i) + " " + lines[j])

        for j in range(len(newLines)): #or len(newLines) since it's
the same
            row = newLines[j]
            #now we can write those data in a temporary txt file sorting
out the
            #the difficulties experienced with the ASCII format
            fileTemp.write("%s" % row)
```

```

    fileTemp = open(pathTemp, "r")    #open the same file but this
time reading (r)
    #read line into array
    lines = fileTemp.readlines()

    x = [] #number file

    h = [] #m/z
    k = [] #intensity

    for i in range(len(lines)):
        splitLines = lines[i].split()    #eg. lines[1]= "23 67 6" -->
splitLines= "23", "67", "6"

        x.append( str(splitLines[0]) ) #this array has file number

        h.append( float(splitLines[2]) ) #m/z
        k.append( int(splitLines[3])) #intensity

    #now that we imported all the data in the arrays we can make the
text file
    #even more user friendly

    fileTemp = open(pathTemp, "a")
    fileTemp.seek(0,0)
    fileTemp.write("min    ?    m/z    int \n\n")

    fileTemp.close()

    return x, h, k, pathOUT, numIntervals

```

findFragments.py

```
# -*- coding: utf-8 -*-
"""
Asks which are the fragments produced after showing the use all the
mass spectra signals and their counts.
"""

def findFrag():

    from allFragments import textTable #I will use the textTable
    function later

    IdFile, mz, intens, pathOUT, numIntervals = textTable()

    fragPath = pathOUT + "FragmentsFound.txt" #where we create file
    with all fragments
    fileFrag = open(fragPath, 'w+') #write and creates
    file(+)
    fileFrag.write("m/z counts\n")
    #now it finds all the fragments and count them

    frame = 0.1 #by default everything that differs less than 0.5 m/z
    units is considered the same specie
    exclude = []

    print("FIND FRAGMENTS OPTIONS")
    print("\nDo you want to consider everything that differs less than
    0.1m/z the same specie?")
    answer1 = int(input("if you want to change this default write 0,
    if not write an other number: "))
    if answer1 == 0:
        frame = float(input("write the new m/z difference to replace
    the default 0.1m/z: "))
        print("\nYour fragments are:")

    m1 = sorted(mz, reverse = True)

    massUser = []
    k_out=0

    for i in range(len(IdFile)):
        summ = m1[i]
        same = 1
        contin = 1
        #if is the same is excluded

        for k in range(len(exclude)):
            if i == exclude[k]:
                contin = 0 #false: we can not continue,this is new
                fragment

        if contin == 1:
            for j in range(i+1, len(IdFile)):
                if m1[j] - frame < m1[i] and m1[i] < m1[j] + frame:
                    summ = summ + m1[j]
```

```

        same = same + 1
        exclude.append(j)
        mean = round(summ/same,2) #the mean of the fragment
found
        fileFrag.write(str(mean) + " " + str(same) + "\n")

        print(str(k_out)+" "+ str(mean) + " " + str(same))
        k_out = k_out + 1
        massUser.append(mean) #now we have correspondence index
with mass
        fileFrag.close()

        #now we have all the data in the txt file. #
        #I want to ask the user wich fragments wants and store these in a
new array

        print("\nNow that you know your fragments tell me which ones you
want")
        strFragUser = input("write the correspondant numbers(eg.0 4 6 13)
with a space in between: ")

        IndexWanted = []
        FragUser = [] #this is integer

        inp=strFragUser.split()

        for i in range(len(inp)):
            FragUser.append(int(inp[i]))

        #now we need a new array with the masses derived from massUser
        #if user choses eg.3 then they want massUser[3]

        change = [] #where we change fragment
        count = -1
        #when we choose numeber it corresponds to m[number] m/z value:
        for i in range(len(FragUser)):

            for j in range(len(IdFile)):
                if mz[j] - frame < massUser[FragUser[i]] and
massUser[FragUser[i]] < mz[j] + frame: #fragment we want
                    #here it's ok, we may store index j to know wich
masses are to consider
                    IndexWanted.append(j)
                    #all we want is stored in IndexWanted
                    count = count + 1
            change.append(count)

        #here we need to store the masses of the fragments for the label
in analysis
        label = []
        for i in range(len(FragUser)):
            label.append(massUser[FragUser[i]])

        return IdFile, intens, IndexWanted, change, label, pathOUT,
numIntervals

```

ClickME.py

```
# -*- coding: utf-8 -*-
"""
This is the final script. You have to double click this one. All the
other scripts
are used by this one. This script recalls findFragments wich uses
LaserONallFragments
wich uses input...
"""

#this is only laser On
def Analysis():

    from findFragments import findFrag
    IdFile, inten, IndexWanted, change, lab, pathOUT, numIntervals =
findFrag()

    #wrrite .txt wavelengh, energy, intensityONparent,
intensityOFFparent, intesnsityfrag1, frag2
    outPath = pathOUT + "finalTableIntensity.txt"
    fileFinal = open(outPath, 'w+')
    line = []

    for i in range(numIntervals):
        line.append(str(i+1)+"min ")

    numFrag = len(change)

    #laser On fragments(number of fragments is numFrag that is the
lenght of change)
    for i in range(len(line)):
        parentON = 0
        fragON=0

    #laser On fragments(number of fragments is numFrag that is the
lenght of change)

        for k in range(change[0]+1):

            if IdFile[IndexWanted[k]] == ("min"+str(i+1)):
                line[i] = line[i] + " " + str(inten[IndexWanted[k]])

                parentON = 1

    if parentON == 0:
        line[i] = line[i] + " " + "xxxx"

    sumFrag = 0 #for relative photodetachment
    for j in range(1, numFrag):
        fragON=0
```

```

        for k in range(change[j-1]+1, change[j]+1):
            if IdFile[IndexWanted[k]] == ("min"+str(i+1)):
                line[i] = line[i] + " " +
str(inten[IndexWanted[k]])
                sumFrag = sumFrag + inten[IndexWanted[k]]
                fragON = 1

    if fragON == 0:
        line[i] = line[i] + " " + "xxxxx"

    fileFinal.write(line[i)+"\n")

label = "min  "
for i in range(len(lab)):
    label = label + str(lab[i])+" "

fileFinal.write(label)

fileFinal.close()

print("You program is finished!!!Check the
FinalTableIntensity.txt")
k=input("press any key to exit ")

Analysis()

```


Abbreviations and glossary

CID – Collision Induced Dissociation

CRM – Charge Residue Model

DFT – Density Functional Theory

ESI – Electrospray Ionization

HCD – Higher Energy Collisional Dissociation

IEM – Ion Evaporation Model

TTP – Tetraphenylporphyrin

LIMS – Laser Interfaced Mass Spectrometer

LDI – Laser Desorption Ionization

MALDI – Matrix Assisted Laser Desorption

MP – Metalloporphyrin

NiOEP – Nickel octaethylporphyrin

$[\text{NiOEP}]^{\cdot+}$ and $[\text{NiOEP}]^{\cdot-}$ – Nickel octaethylporphyrin radical cation and anion

OEP – Octaethylporphyrin

PD – Photodepletion

PF – Photofragmentation

X – Halide atom (X = F, Cl, I, Br)

TIC – Total Ion Current

VDE – Vertical Detachment Energy

ZnTPP – Zinc tetraphenylporphyrin

$[\text{ZnTPP}]^{\cdot+}$ and $[\text{ZnTPP}]^{\cdot-}$ – Zinc tetraphenylporphyrin radical cation and anion

$\text{ZnTPP} \cdot \text{X}^-$ – Cluster between zinc tetraphenyl porphyrin and a halide anion

Action spectrum: Indirect absorption spectrum.

Action spectroscopy: Indirect spectroscopic technique to obtain an absorption spectrum when it is not possible to measure directly the difference between the light in and out.

Aggregate/cluster: General term used to describe two or more molecules/ions that are kept together by electrostatic interactions; in mass spectrometry, the formation of ion clusters in the ion source is a common phenomenon. In this thesis, the term aggregate/cluster is extended also to describe complexes observed to be produced in the ionization source.

Photodepletion: Depletion of a molecular species mediated by light due to photodissociation or electron loss. It can also be defined with negatively charged atomic species since they can deplete by losing electrons.

Photodepletion spectrum: Plot of the photodepletion yield vs. wavelength or photon energy; this is considered an indirect absorption spectrum (action spectra).

Photodetachment: The absorption of a photon and subsequent elimination of an electron from an anion to form a neutral species.

Photodissociation: dissociation of a chemical compound by the action of light.

Photofragmentation: Synonymus of photodissociation.

Photofragmentation spectrum: Plot of the photofragmentation yield vs. wavelength or photon energy; this shows the production profile of the photofragment considered.

Photodissociation mass spectrum: Mass spectrum taken after the ions have absorbed photons and have dissociated; the mass spectra peaks of photofragments produces are therefore displayed.

Photoelectron spectroscopy: refers to energy measurement of electrons emitted from solids, gases or liquids by the photoelectric effect, in order to determine the binding energies of electrons in a substance.

Photoelectron spectrum: Plot of ionization energy Vs. electron counts derived from a photoelectron spectroscopy experiment.

Bibliography

- (1) Mirkovic, T., Ostroumov, E. E., Anna, J. M., van Grondelle, R., Govindjee, and Scholes, G. D. (2017) Light Absorption and Energy Transfer in the Antenna Complexes of Photosynthetic Organisms. *Chem. Rev.* *117*, 249–293.
- (2) Walter, M. G., Rudine, A. B., and Wamser, C. C. (2010) Porphyrins and phthalocyanines in solar photovoltaic cells. *J. Porphy. Phthalocyanines*.
- (3) Yella, A., Lee, H. W., Tsao, H. N., Yi, C., Chandiran, A. K., Nazeeruddin, M. K., Diao, E. W. G., Yeh, C. Y., Zakeeruddin, S. M., and Grätzel, M. (2011) Porphyrin-sensitized solar cells with cobalt (II/III)-based redox electrolyte exceed 12 percent efficiency. *Science* (80-).
- (4) Mahmood, A., Hu, J.-Y., Xiao, B., Tang, A., Wang, X., and Zhou, E. (2018) Recent progress in porphyrin-based materials for organic solar cells. *J. Mater. Chem. A Mater. Energy Sustain.* *6*, 16769–16797.
- (5) Windle, C. D., George, M. W., Perutz, R. N., Summers, P. A., Sun, X. Z., and Whitwood, A. C. (2015) Comparison of rhenium--porphyrin dyads for {CO₂} photoreduction: photocatalytic studies and charge separation dynamics studied by time-resolved {IR} spectroscopy. *Chem. Sci.*
- (6) Windle, C. D., Câmpian, M. V., Duhme-Klair, A. K., Gibson, E. A., Perutz, R. N., and Schneider, J. (2012) CO₂ photoreduction with long-wavelength light: Dyads and monomers of zinc porphyrin and rhenium bipyridine. *Chem. Commun.*
- (7) Hambourger, M., Moore, G. F., Kramer, D. M., Gust, D., Moore, A. L., and Moore, T. A. (2009) Biology and technology for photochemical fuel production. *Chem. Soc. Rev.*
- (8) Giuntini, F., Boyle, R., Sibrian-Vazquez, M., and Graça H. Vicente, M. (2013) Porphyrin Conjugates for Cancer Therapy, pp 303–416.
- (9) Wormald, R., Evans, J., Smeeth, L., and Henshaw, K. (2005) Photodynamic therapy for neovascular age-related macular degeneration. *Cochrane database Syst. Rev.* CD002030.
- (10) Price, M., Terlecky, S. R., and Kessel, D. (2009) A role for hydrogen peroxide in the pro-apoptotic effects of photodynamic therapy. *Photochem. Photobiol.*
- (11) Singh, S., Aggarwal, A., Bhupathiraju, N. V. S. D. K., Arianna, G., Tiwari, K., and Drain, C. M. (2015) Glycosylated Porphyrins, Phthalocyanines, and Other Porphyrinoids for Diagnostics and Therapeutics. *Chem. Rev.*
- (12) Gold, M. H. (2008) Therapeutic and Aesthetic Uses of Photodynamic Therapy Part two of a five-part series: Lasers and Light Treatments for Acne Vulgaris Promising Therapies. *J. Clin. Aesthet. Dermatol.*
- (13) Fyrestam, J., Bjurshammar, N., Paulsson, E., Johannsen, A., and Östman, C. (2015) Determination of porphyrins in oral bacteria by liquid chromatography electrospray ionization tandem mass spectrometry. *Anal. Bioanal. Chem.*
- (14) Gouterman, M., Wagnière, G. H., and Snyder, L. C. (1963) Spectra of porphyrins: Part {II}. Four orbital model. *J. Mol. Spectrosc.* *11*, 108–127.
- (15) Namuangruk, S., Sirithip, K., Rattanatwan, R., Keawin, T., Kungwan, N., Sudyodsuk, T.,

Promarak, V., Surakhot, Y., and Jungsuttiwong, S. (2014) Theoretical investigation of the charge-transfer properties in different meso-linked zinc porphyrins for highly efficient dye-sensitized solar cells. *Dalt. Trans.*

(16) Marsh, D. F., and Mink, L. M. (1996) Microscale synthesis and electronic absorption spectroscopy of tetraphenylporphyrin H₂(TPP) and metalloporphyrins ZnII(TPP) and NiII(TPP). *J. Chem. Educ.*

(17) Nielsen, S. B. (2012) Gas-phase spectroscopy of biomolecular ions: Porphyrins and metalloporphyrins. *J. Phys. Conf. Ser.* 388, 12026.

(18) Milne, B. F., Toker, Y., Rubio, A., and Nielsen, S. B. (2015) Unraveling the intrinsic color of chlorophyll. *Angew. Chem. Int. Ed Engl.* 54, 2170–2173.

(19) Milne, B. F., Kjaer, C., Houmøller, J., Stockett, M. H., Toker, Y., Rubio, A., and Nielsen, S. B. (2016) On the Exciton Coupling between Two Chlorophyll Pigments in the Absence of a Protein Environment: Intrinsic Effects Revealed by Theory and Experiment. *Angew. Chem. Int. Ed Engl.* 55, 6248–6251.

(20) Szatkowski, L., and Hall, M. B. (2016) Dehalogenation of chloroalkanes by nickel(i) porphyrin derivatives, a computational study. *Dalt. Trans.*

(21) Ermler, U. (2005) On the mechanism of methyl-coenzyme M reductase. *Dalt. Trans.*

(22) Wakao, N., Yokoi, N., Ioyama, N., Hiraishi, A., Shimada, K., Kobayashi, M., Kise, H., Iwaki, M., Itoh, S., Takaichi, S., and Sakurai, Y. (1996) Discovery of natural photosynthesis using Zn-containing bacteriochlorophyll in an aerobic bacterium *Acidiphilium rubrum*. *Plant Cell Physiol.*

(23) Lin, S., Jaschke, P. R., Wang, H., Paddock, M., Tufts, A., Allen, J. P., Rosell, F. I., Mauk, A. G., Woodbury, N. W., and Beatty, J. T. (2009) Electron transfer in the *Rhodobacter sphaeroides* reaction center assembled with zinc bacteriochlorophyll. *Proc. Natl. Acad. Sci. U. S. A.*

(24) Ali, M., Kumar, V., Baker, S. N., Baker, G. A., and Pandey, S. (2010) J-aggregation of ionic liquid solutions of meso-tetrakis(4-sulfonatophenyl) porphyrin. *Phys. Chem. Chem. Phys.* 12, 1886–1894.

(25) Schwarz, U., Vonderach, M., Armbruster, M. K., Fink, K., Kappes, M. M., and Weis, P. (2014) Cu(II)- and Mn(III)-porphyrin-derived oligomeric multianions: Structures and photoelectron spectra. *J. Phys. Chem. A.*

(26) Scheller, M. K., Compton, R. N., and Cederbaum, L. S. (1995) {Gas-Phase} Multiply Charged Anions. *Science (80-.)*. 270, 1160–1166.

(27) Wang, X.-B., and Wang, L.-S. (1999) Observation of negative electron-binding energy in a molecule. *Nature* 400, 245–248.

(28) Karpuschkin, T., Kappes, M. M., and Hampe, O. (2013) Binding of {O₂} and {CO} to metal porphyrin anions in the gas phase. *Angew. Chem. Int. Ed.* 52, 10374–10377.

(29) Archipov, T., Kirkland, J. K., Vogiatzis, K. D., Steiner, A., Niedner-Schatteburg, G., Weis, P., Fink, K., Hampe, O., and Kappes, M. M. (2018) {Gas-Phase} Ion Chemistry of Metalloporphyrin Anions with Molecular Oxygen: Probing the Influence of the Oxidation and Spin State of the Central Transition Metal by Experiment and Theory. *J. Phys. Chem. A.*

(30) Jäger, P., Brendle, K., Schwarz, U., Himmelsbach, M., Armbruster, M. K., Fink, K., Weis, P., and Kappes, M. M. (2016) {Q} and Soret Band Photoexcitation of Isolated Palladium Porphyrin

Tetraanions Leads to Delayed Emission of Nonthermal Electrons over Microsecond Time Scales. *J. Phys. Chem. Lett.* **7**, 1167–1172.

(31) Jäger, P., Brendle, K., Schneider, E., Kohaut, S., Armbruster, M. K., Fink, K., Weis, P., and Kappes, M. M. (2018) Photodissociation of Free Metalloporphyrin Dimer Multianions. *J. Phys. Chem. A* **122**, 2974–2982.

(32) Stockett, M. H., Musbat, L., Kjær, C., Houmøller, J., Toker, Y., Rubio, A., Milne, B. F., and Brøndsted Nielsen, S. (2015) The Soret absorption band of isolated chlorophyll a and b tagged with quaternary ammonium ions. *Phys. Chem. Chem. Phys.* **17**, 25793–25798.

(33) Hitzenberger, J. F., Dammann, C., Lang, N., Lungerich, D., Garcia-Iglesias, M., Bottari, G., Torres, T., Jux, N., and Drewello, T. (2016) Making the invisible visible: improved electrospray ion formation of metalloporphyrins/-phthalocyanines by attachment of the formate anion (HCOO⁻). *Analyst* **141**, 1347–1355.

(34) Sleno, L., and Volmer, D. A. (2004) Ion activation methods for tandem mass spectrometry. *J. Mass Spectrom.*

(35) Kertesz, T. M., Hall, L. H., Hill, D. W., and Grant, D. F. (2009) CE50: Quantifying Collision Induced Dissociation Energy for Small Molecule Characterization and Identification. *J. Am. Soc. Mass Spectrom.*

(36) Gozet, T., Huynh, L., and Bohme, D. K. (2009) Collision-induced dissociation of tetraphenyl iron and manganese porphyrin ions by electrospray ionization mass spectrometry. *Int. J. Mass Spectrom.*

(37) Brendle, K., Kordel, M., Schneider, E., Wagner, D., Bräse, S., Weis, P., and Kappes, M. M. (2018) Collision Induced Dissociation of {Benzylpyridinium-Substituted} Porphyrins: Towards a Thermometer Scale for Multiply Charged Ions? *J. Am. Soc. Mass Spectrom.* **29**, 382–392.

(38) Molecular beam, <https://www.britannica.com/science/molecular-beam>, accessed 28/11/2019

(39) Jankunas, J., and Osterwalder, A. (2015) Cold and Controlled Molecular Beams: Production and Applications. *Annu. Rev. Phys. Chem.*

(40) Even, U., Magen, Y., Jortner, J., and Levanon, H. (1981) Excited-state energetics and dynamics of magnesium tetraphenylporphyrin cooled in supersonic expansions. *J. Am. Chem. Soc.* **103**, 4583–4585.

(41) Even, U., Magen, J., Jortner, J., Friedman, J., and Levanon, H. (1982) Isolated ultracold porphyrins in supersonic expansions. I. Free-base tetraphenylporphyrin and Zn-tetraphenylporphyrin. *J. Chem. Phys.* **77**, 4374–4383.

(42) Beames, J. M., Hudson, A. J., Vaden, T. D., and Simons, J. P. (2010) Double-resonance spectroscopy of the jet-cooled free base and Cu (II) complex of protoporphyrin IX. *Phys. Chem. Chem. Phys.* **12**, 14076–14081.

(43) Cercola, R., Matthews, E., and Dessent, C. E. H. (2017) Photoexcitation of Adenosine 5'-Triphosphate Anions in Vacuo: Probing the Influence of Charge State on the UV Photophysics of Adenine. *J. Phys. Chem. B.*

(44) verteporfin for injection, package insert, . Bausch Lomb Inc. [https://www.bausch.com/Portals/77/-](https://www.bausch.com/Portals/77/)

/m/BL/United%20States/Files/Package%20Inserts/Pharma/visudyne-package-insert.pdf,
accessed 28/11/2019

- (45) Scott, L. J., and Goa, K. L. (2000) Verteporfin. *Drugs Aging* 16, 139–146.
- (46) Sahni, V., and Sahni, V. (2004) The Hohenberg-Kohn Theorems and Kohn-Sham Density Functional Theory, in *Quantal Density Functional Theory*, pp 99–123. Springer Berlin Heidelberg.
- (47) Mann, M., and Fenn, J. B. (1992) Electrospray Mass Spectrometry, in *Mass Spectrometry*, pp 1–35. Springer US, Boston, MA.
- (48) Page, J. S., Kelly, R. T., Tang, K., and Smith, R. D. (2007) Ionization and Transmission Efficiency in an Electrospray Ionization-Mass Spectrometry Interface. *J. Am. Soc. Mass Spectrom.*
- (49) Loo, J. A. (1997) Studying noncovalent protein complexes by electrospray ionization mass spectrometry. *Mass Spectrom. Rev.*
- (50) Kellogg, M. D. (2016) Measurement of Biological Materials, in *Clinical and Translational Science: Principles of Human Research: Second Edition*, pp 137–155. Elsevier Inc.
- (51) Konermann, L., Ahadi, E., Rodriguez, A. D., and Vahidi, S. (2013) Unraveling the mechanism of electrospray ionization. *Anal. Chem.*
- (52) Ho, C. S., Lam, C. W. K., Chan, M. H. M., Cheung, R. C. K., Law, L. K., Lit, L. C. W., Ng, K. F., Suen, M. W. M., and Tai, H. L. (2003) Electrospray ionisation mass spectrometry: principles and clinical applications. *Clin. Biochem. Rev.*
- (53) Banerjee, S., and Mazumdar, S. (2012) Electrospray Ionization Mass Spectrometry: A Technique to Access the Information beyond the Molecular Weight of the Analyte. *Int. J. Anal. Chem.*
- (54) Wilm, M. (2011) Principles of electrospray ionization. *Mol. Cell. Proteomics.*
- (55) Dastourani, H., Jahannama, M. R., and Eslami-Majd, A. (2018) A physical insight into electrospray process in cone-jet mode: Role of operating parameters. *Int. J. Heat Fluid Flow.*
- (56) Wilm, M. S., and Mann, M. (1994) Electrospray and Taylor-Cone theory, Dole's beam of macromolecules at last? *Int. J. Mass Spectrom. Ion Process.*
- (57) Guharay, S. K., Dwivedi, P., and Hill, H. H. (2008) Ion mobility spectrometry: Ion source development and applications in physical and biological sciences. *IEEE Trans. Plasma Sci.*
- (58) Kebarle, P. (2000) A brief overview of the present status of the mechanisms involved in electrospray mass spectrometry. *J. Mass Spectrom.*
- (59) Dole, M., Mack, L. L., Hines, R. L., Mobley, R. C., and Ferguson, L. D. (1968) Molecular beams of macroions. *J Chem. Phys.*
- (60) Iribarne, J. V., and Thomson, B. A. (1976) On the evaporation of small ions from charged droplets. *J. Chem. Phys.*
- (61) Hillenkamp, F., Karas, M., Beavis, R. C., and Chait, B. T. (1991) Matrix-Assisted Laser Desorption/Ionization Mass Spectrometry of Biopolymers. *Anal. Chem.*
- (62) Robinson, K. N., Steven, R. T., and Bunch, J. (2018) Matrix Optical Absorption in UV-MALDI MS. *J. Am. Soc. Mass Spectrom.*

- (63) Karas, M., and Krüger, R. (2003) Ion formation in MALDI: The cluster ionization mechanism. *Chem. Rev.*
- (64) Science, L., Search, C., and Inquiry, P. (2017) Principles of MALDI-TOF Mass Spectrometry : SHIMADZU (Shimadzu Corporation).
- (65) Liu, J., Song, K., Hase, W. L., and Anderson, S. L. (2003) Direct dynamics study of energy transfer and collision-induced dissociation: Effects of impact energy, geometry, and reactant vibrational mode in H₂CO⁺- Ne collisions. *J. Chem. Phys.*
- (66) Ichou, F., Schwarzenberg, A., Lesage, D., Alves, S., Junot, C., MacHuron-Mandard, X., and Tabet, J. C. (2014) Comparison of the activation time effects and the internal energy distributions for the CID, PQD and HCD excitation modes. *J. Mass Spectrom.* 49, 498–508.
- (67) Matthews, E., and Dessent, C. E. H. (2017) Experiment and theory confirm that UV laser photodissociation spectroscopy can distinguish protomers formed: Via electrospray. *Phys. Chem. Chem. Phys.*
- (68) Matthews, E., and Dessent, C. E. H. (2016) Locating the proton in nicotinamide protomers via low-Resolution UV action spectroscopy of electrosprayed solutions. *J. Phys. Chem. A.*
- (69) Talbot, F. O., Sciuto, S. V., and Jockusch, R. A. (2013) Fluorescence imaging for visualization of the ion cloud in a quadrupole ion trap mass spectrometer. *J. Am. Soc. Mass Spectrom.*
- (70) Compagnon, I., Allouche, A. R., Bertorelle, F., Antoine, R., and Dugourd, P. (2010) Photodetachment of tryptophan anion: An optical probe of remote electron. *Phys. Chem. Chem. Phys.*
- (71) Matthews, E., Cercola, R., Mensa-Bonsu, G., Neumark, D. M., and Dessent, C. E. H. (2018) Photoexcitation of iodide ion-pyrimidine clusters above the electron detachment threshold: Intracluster electron transfer versus nucleobase-centred excitations. *J. Chem. Phys.* 148.
- (72) Frisch, M. J., Trucks, G. W., Schlegel, H. B., Scuseria, G. E., Robb, M. A., Cheeseman, J. R., Scalmani, G., Barone, V., Mennucci, B., Petersson, G. A., Nakatsuji, H., Caricato, M., Li, X., Hratchian, H. P., Izmaylov, A. F., Bloino, J., Zheng, G., Sonnenberg, J. L., Hada, M., Ehara, M., Toyota, K., Fukuda, R., Hasegawa, J., Ishida, M., Nakajima, T., Honda, Y., Kitao, O., Nakai, H., Vreven, T., Montgomery Jr., J. A., Peralta, J. E., Ogliaro, F., Bearpark, M., Heyd, J. J., Brothers, E., Kudin, K. N., Staroverov, V. N., Kobayashi, R., Normand, J., Raghavachari, K., Rendell, A., Burant, J. C., Iyengar, S. S., Tomasi, J., Cossi, M., Rega, N., Millam, J. M., Klene, M., Knox, J. E., Cross, J. B., Bakken, V., Adamo, C., Jaramillo, J., Gomperts, R., Stratmann, R. E., Yazyev, O., Austin, A. J., Cammi, R., Pomelli, C., Ochterski, J. W., Martin, R. L., Morokuma, K., Zakrzewski, V. G., Voth, G. A., Salvador, P., Dannenberg, J. J., Dapprich, S., Daniels, A. D., Farkas, Foresman, J. B., Ortiz, J. V., Cioslowski, J., and Fox, D. J. (2010) Gaussian09 Revision D.01, Gaussian Inc. Wallingford CT. *Gaussian 09 Revis. C.01.*
- (73) Calais, J.-L. (1993) Density-functional theory of atoms and molecules. R.G. Parr and W. Yang, Oxford University Press, New York, Oxford, 1989. IX + 333 pp. Price £45.00. *Int. J. Quantum Chem.* 47, 101–101.
- (74) Rassolov, V. A., Pople, J. A., Ratner, M. A., and Windus, T. L. (1998) 6-31G* basis set for atoms K through Zn. *J. Chem. Phys.*
- (75) Yurieva, A. G., Poleshchuk, O. K., and Filimonov, V. D. (2008) Comparative analysis of a full-electron basis set and pseudopotential for the iodine atom in DFT quantum-chemical

calculations of iodine-containing compounds. *J. Struct. Chem.*

(76) Swart, M., Güell, M., Luis, J. M., and Solà, M. (2010) Spin-state-corrected Gaussian-type orbital basis sets. *J. Phys. Chem. A* 114, 7191–7197.

(77) Nguyen, K. A., and Pachter, R. (2001) Ground state electronic structures and spectra of zinc complexes of porphyrin, tetraazaporphyrin, tetrabenzoporphyrin, and phthalocyanine: A density functional theory study. *J. Chem. Phys.*

(78) Wu, Z. Y., Wang, T., Meng, Y. S., Rao, Y., Wang, B. W., Zheng, J., Gao, S., and Zhang, J. L. (2017) Enhancing the reactivity of nickel(II) in hydrogen evolution reactions (HERs) by β -hydrogenation of porphyrinoid ligands. *Chem. Sci.*

(79) Stoyanov, S. R., Yin, C. X., Gray, M. R., Stryker, J. M., Gusarov, S., and Kovalenko, A. (2010) Computational and experimental study of the structure preferences binding preferences, and spectroscopy of nickel(II) and petroleum vanadyl porphyrins in petroleum. *J. Phys. Chem. B.*

(80) Ekrami, S., and Shamlouei, H. R. (2018) Ab initio study of C 20 nanocluster effects on electrochemical properties of tetraphenylporphyrin. *J. Porphyr. Phthalocyanines.*

(81) Grimme, S., Antony, J., Ehrlich, S., and Krieg, H. (2010) A consistent and accurate ab initio parametrization of density functional dispersion correction (DFT-D) for the 94 elements H-Pu. *J. Chem. Phys.*

(82) Weinhold, F., Landis, C. R., and Glendening, E. D. (2016) What is NBO analysis and how is it useful? *Int. Rev. Phys. Chem.*

(83) Yao, H., and Jockusch, R. A. (2013) Fluorescence and electronic action spectroscopy of mass-selected gas-phase fluorescein, 2',7'-dichlorofluorescein, and 2',7'- difluorofluorescein ions. *J. Phys. Chem. A.*

(84) Nappa, M., and Valentine, J. S. (1978) The influence of axial ligands on metalloporphyrin visible absorption spectra. Complexes of tetraphenylporphinatozinc. *J. Am. Chem. Soc.* 100, 5075–5080.

(85) Morris, A. J., Marton, A., and Meyer, G. J. (2008) Halide coordination to zinc porphyrin sensitizers anchored to nanocrystalline {TiO₂}. *Inorg. Chem.* 47, 7681–7685.

(86) Periodic Table of Elements - PubChem, <https://pubchem.ncbi.nlm.nih.gov/periodic-table/>, accessed 28/11/2019

(87) McClellan, J. E., Murphy, J. P., Mulholland, J. J., Yost, R. A., and E P, S. J. (1987) Effects of Fragile Ions on Mass Resolution and on Isolation for Tandem Mass Spectrometry in the Quadrupole Ion Trap Mass Spectrometer. *Int. J. Mass Spectrom. Ion Process.* 1, 402.

(88) Hawkridge, M. (2018) Electronic Laser Photodissociation Spectroscopy of Gas-Phase Metalloporphyrins and Metalloporphyrin-Aromatic Molecule Complexes.

(89) Wyer, J. A., and Nielsen, S. B. (2010) Absorption in the Q-band region by isolated ferric heme⁺ and heme⁺ (histidine) in vacuo. *J. Chem. Phys.*

(90) March, R. E. (1997) An introduction to quadrupole ion trap mass spectrometry. *J. Mass Spectrom.*

(91) Dawson, P. H. (1988) Quadrupole mass filters with varying mathieu parameter. *Int. J. Mass Spectrom. Ion Process.* 83, 295–309.

- (92) Wong, N. G. K., Berenbeim, J. A., Hawkrige, M., Matthews, E., and Dessent, C. E. H. (2019) Mapping the intrinsic absorption properties and photodegradation pathways of the protonated and deprotonated forms of the sunscreen oxybenzone †. *Phys. Chem. Chem. Phys.* **21**, 14311.
- (93) Mckechnie, S., Booth, G. H., Cohen, A. J., and Cole, J. M. On the Accuracy of Density Functional Theory and Wave Function Methods for Calculating Vertical Ionization Energies.
- (94) Nielsen, S. B. (2012) Gas-phase spectroscopy of biomolecular ions: Porphyrins and metalloporphyrins, in *Journal of Physics: Conference Series*.
- (95) Zhang, S., and Gerhard, G. S. (2009) Heme mediates cytotoxicity from artemisinin and serves as a general anti-proliferation target. *PLoS One*.
- (96) Stockett, M. H., Houmøller, J., and Brøndsted Nielsen, S. (2016) Nile blue shows its true colors in gas-phase absorption and luminescence ion spectroscopy. *J. Chem. Phys.*
- (97) Shimizu, D., and Osuka, A. (2018) Porphyrinoids as a platform of stable radicals. *Chem. Sci.*
- (98) Tran, T. T. H., Chang, Y. R., Hoang, T. K. A., Kuo, M. Y., and Su, Y. O. (2016) Electrochemical Behavior of meso-Substituted Porphyrins: The Role of Cation Radicals to the Half-Wave Oxidation Potential Splitting. *J. Phys. Chem. A* **120**, 5504–5511.
- (99) Fuhrhop, J. H., and Mauzerall, D. (1969) The One-Electron Oxidation of Metalloporphyrins. *J. Am. Chem. Soc.* **91**, 4174–4181.
- (100) Mauzerall, D., and Feher, G. (1964) A study of the photoinduced porphyrin free radical by electron spin resonance. *BBA - Spec. Sect. Biophys. Subj.*
- (101) Rosario, M., Domingues, M., Nemirovskiy, O. V., Graço, M., Marques, O. S., Graça Neves, M., Cavaleiro, J. A. S., Ferrer-Correia, A. J., and Gross, M. L. (1998) High- and low-energy collisionally activated decompositions of octaethylporphyrin and its metal complexes. *J. Am. Soc. Mass Spectrom.*
- (102) Vandell, V. E., and Limbach, P. A. (1998) Electrospray ionization mass spectrometry of metalloporphyrins. *J. Mass Spectrom.* **33**, 212–220.
- (103) Van Berkel, G. J., McLuckey, S. A., and Glish, G. L. (1991) Electrospray ionization of porphyrins using a quadrupole ion trap for mass analysis. *Anal. Chem.* **63**, 1098–1109.
- (104) (2001) Assignment of the optical spectrum of metal porphyrin and phthalocyanine radical anions. *J. Porphyr. Phthalocyanines* **5**, 67–76.
- (105) Gozet, T., Huynh, L., and Bohme, D. K. (2009) Collision-induced dissociation of tetraphenyl iron and manganese porphyrin ions by electrospray ionization mass spectrometry. *Int. J. Mass Spectrom.* **279**, 113–118.
- (106) Rosario, M., Domingues, M., Graça, M., Marques, O. S., Alonso, C. M. A., Neves, P. M. S., Cavaleiro, J. A. S., Ferrer-Correia, A. J., Nemirovskiy, O. V., and Gross, M. L. (2002) Unexpected Fragmentation of-Substituted meso-Tetraphenylporphyrins Induced by High-Energy Collisional Activation.
- (107) Silva, E. M. P., Domingues, P., Tomé, J. P. C., Amparo, M., austino, Graça, M., Neves, P. M. S., Tomé, A. C., Dauzonne, D., Silva, A. M. S., Cavaleiro, J. A. S., Ferrer-Correia, A. J., Rosário, M., and Domingues, M. (2008) Electrospray tandem mass spectrometry of b-nitroalkenyl meso-tetraphenylporphyrins.

- (108) Kaczorowska, M. A., and Cooper, H. J. (2011) Electron induced dissociation (EID) tandem mass spectrometry of octaethylporphyrin and its iron(III) complex. *Chem. Commun.* **47**, 418–420.
- (109) Olsen, J. V, Macek, B., Lange, O., Makarov, A., Horning, S., and Mann, M. (2007) RECEIVED 19 MARCH; ACCEPTED 30 JULY; PUBLISHED ONLINE 26. *Nat. Methods* **4**.
- (110) Piet, D. P., Danovich, D., Zuilhof, H., and Sudhölter, E. J. R. (1999) Ionization potentials of porphyrins and phthalocyanines. a comparative benchmark study of fast improvements of Koopman's Theorem. *J. Chem. Soc. Perkin Trans.* **2**.
- (111) Jarvi, M. T., Patterson, M. S., and Wilson, B. C. (2012) Insights into photodynamic therapy dosimetry: Simultaneous singlet oxygen luminescence and photosensitizer photobleaching measurements. *Biophys. J.*
- (112) Gillies, R., Kollias, N., Hasan, T., and Diddens, H. (1996) Spectral characterization of the benzoporphyrin derivative monoacid ring-A photoproduct formed in fetal calf solutions during irradiation with 694 nm continuous-wave radiation. *J. Photochem. Photobiol. B Biol.*
- (113) Zeng, H., Korbelik, M., McLean, D. I., MacAulay, C., and Lui, H. (2007) Monitoring Photoproduct Formation and Photobleaching by Fluorescence Spectroscopy Has the Potential to Improve PDT Dosimetry with a Verteporfin-like Photosensitizer. *Photochem. Photobiol.* **75**, 398–405.
- (114) Nicol, M. F. (1974) Solvent Effects on Electronic Spectra. *Appl. Spectrosc. Rev.* **8**, 183–227.
- (115) Marsh, B. M., Duffy, E. M., Soukup, M. T., Zhou, J., and Garand, E. (2014) Intramolecular Hydrogen Bonding Motifs in Deprotonated Glycine Peptides by Cryogenic Ion Infrared Spectroscopy. *J. Phys. Chem. A* **118**, 3906–3912.
- (116) Buytendyk, A. M., Graham, J. D., Gould, J., and Bowen, K. H. (2015) Parent Anions of Iron, Manganese, and Nickel Tetraphenyl Porphyrins: Photoelectron Spectroscopy and Computations. *J. Phys. Chem. A* **119**, 8643–8646.
- (117) Ahmad, I., Ahmed, S., Anwar, Z., Sheraz, M. A., and Sikorski, M. (2016) Photostability and Photostabilization of Drugs and Drug Products. *Int. J. Photoenergy*. Hindawi Publishing Corporation.
- (118) Serxner, D., Dessent, C. E. H., and Johnson, M. A. (1996) Precursor of the I⁻ charge-transfer-to-solvent (CTTS) band in I⁻·(H₂O)_n clusters. *J. Chem. Phys.*
- (119) Zollweg, R. J. (1969) Binding Energies in Atomic Negative Ions: III. *J. Phys. Chem. Ref. Data* **50**, 15.